



Università Politecnica delle Marche
Scuola di Dottorato di Ricerca in Scienze dell'Ingegneria
Corso di Dottorato in Ingegneria Industriale

Physical modelling of the high temperature deformation of complex microstructure materials for aeronautical applications

Ph.D. Dissertation of:
Mohamed Saad Ghat

Supervisor:
Prof.Ing. Stefano Spigarelli

Ph.D. Course coordinator:
Prof. Giovanni Di Nicola

XVIII edition - new series



Università Politecnica delle Marche
Scuola di Dottorato di Ricerca in Scienze dell'Ingegneria
Corso di Dottorato in Ingegneria Industriale

Physical modelling of the high temperature deformation of complex microstructure materials for aeronautical applications

Ph.D. Dissertation of:
Mohamed Saad Ghat

Supervisor:
Prof.Ing. Stefano Spigarelli

Ph.D. Course coordinator:
Prof. Giovanni Di Nicola

XVIII edition - new series

Università Politecnica delle Marche
Dipartimento di (Ingegneria Industriale e Scienze Matematiche)
Via Brecce Bianche — 60131 - Ancona, Italy

To my parents,

Eng.Saad Shehata Ghat & Mrs.Fatma El-Zahra M.Khalil

*For what you've been
&
what you've done*

To:

My sister "Fatma El-Zahra Ghat" and my brother "Dr.Amr Ghat"

My uncle "Mr.Moustafa M.Khalil" and "Dr.Metwaley shehata Ghat"

My beloved late grandparents "Shehata Ghat" and "Mohamed Khalil"

Acknowledgements

Firstly, I would like to express my sincere gratitude to my advisor Prof. Ing. Stefano Spigarelli. for the continuous support of my Ph.D study and related research, for his patience, motivation, and knowledge, for providing me an opportunity to join the team as intern, and who gave access to the laboratory and research facilities, and for his guidance helped me in all the time of research and writing of this thesis.

Beside my advisor, my sincere thanks also go to Prof. Marcello Cabibbo, for his support and guidance during my research. Also, I am particularly grateful to Prof. Maria Cecilia Poletti at Graz university of Technology, Austria, for her time and academic support during the stay period in Graz. I am grateful to Prof. M. El Mehtedi for his efforts, helpful and inspiring on the torsion tests activities.

I also want to thank all the technical staff who have helped me and offered their technical assistance to carry out my experimental work, especially Daniele Ciccarelli.

I thank all my friends and colleagues, past and present, whether discussing work at the University, especially Chiara Paoletti, Dagmawi Neway and Ahmed S.Afify, for their friendship and sharing a scientific and general ideas. Finally, I reserve heartfelt thanks to my parents, I cannot express gratitude in words to my father, mother, brother and sisters who have fully supported me and encouraged me to reach the finish line. Thanks to My late grandparents.

Ancona, November, 2019

Mohamed Saad Ghat

“The important thing is to not stop questioning. Curiosity has its own reason for existing.”

“Life is like riding a bicycle. To keep your balance, you must keep moving.”

Albert Einstein (1879 –1955)

“Resist What You Love And Bear What You Hate.”

Mustafa Mahmoud (1921–2009)

Abstract

Today aerospace industry is growing fast on developing the mechanical component for the hot section part of the jet engine. The prediction of the dynamic behavior of metals is usually investigated by phenomenological models. In this study, we described the hot deformation behavior by using different approaches for constitutive model: Hansel and spittle equation, Garofalo equation and basic modelling. In the present PhD work, three different metals were used (Inconel 718, Ti-6Al-4V and AA2024 – T3) which are extensively used in the aerospace industry. A basic model was applied to pure Ni and then to a single-phase superalloy. In the case of Ti-6Al-4V alloy, the hot deformation behavior was studied by hot compression test in β phase domain. The effects of hot deformation parameters (deformation temperature and strain rate) on flow stress were analyzed. A phenomenological model based on the Hansel and Spittel equation was used to obtain a quite accurate description of the flow curves for processing temperatures between 1010 and 1150 °C and strain rates of 100 and 0.001 s⁻¹. The model used gave an accurate excellent experiments result. The high temperature deformation of the superalloy, a solution treated IN718, was investigated by torsion testing in a high-temperature regime (1000–1100 °C). The peak-flow stress dependence on strain-rate and temperature was described by a physically-based constitutive equations, which took into account both dislocation hardening and solid solution strengthening, and represents a substantial advancement over phenomenological models, although, in the present form, it cannot give the full shape of the flow curves.

The creep response for AA2024-T3 alloy produced by a friction stir processing (FSP) has been investigated, the same creep modeling based on the theoretical approach. The hardness variation with creep duration was used to quantify the particle strengthening term.

Table of Contents

Acknowledgements	ii
Abstract	iv
List of Figures	ii
List of Tables.....	v
Chapter 1 – Introduction	1
1.1. Thermomechanical Modelling	1
1.2. Project Aims	3
1.3. Thesis Outline.....	3
Chapter 2 – Literature Review.....	6
2.1. High Temperature Materials	6
2.2. The need for high-temperature materials	7
2.3. Operating environment.....	9
2.4. Constitutive descriptions for metals and alloys in hot working	13
2.4.1. Arrhenius equation	15
2.5. The material for high temperature application: what is the superalloy?.....	19
2.5.1. Classification of superalloys	19
2.6. Application of Superalloys	24
2.7. Physical metallurgy of nickel and its alloys.....	25
2.8. Inconel 718: Features and characterization	29
2.9. Workability and hot deformation behavior of IN718.....	31
2.10. Titanium Alloys.....	35
2.10.1. Classification of titanium alloys.....	37
2.11. Ti-6Al-4V features and characterization	41
2.12. Workability and hot deformation behavior of Ti-6Al-4V	43
2.13. Aluminum and Aluminum Alloys.....	45
2.13.1. Alloy Categories.....	45

2.13.2. Wrought Alloy Classes.....	47
2.14. Hot deformation and creep of Aluminum alloys.....	52
2.15. Conclusions	52
Chapter 3 - Constitutive Modeling On β Transus of Ti-6Al-4V Alloy at High Temperature and Strain Rates	55
3.1. Introduction	55
3.2. Compression test	56
3.3. Experimental Procedure	58
3.4. Experimental results for Ti – 6Al – 4V	59
3.4.1. Peak flow stress dependence on strain rate and temperature.	59
3.4.2. Flow stress variation with strain, strain rate and temperature	63
3.5. Summary and Conclusions	70
Chapter 4 - A model for the Hot Workability of Solution Treated IN718 Superalloy.....	72
4.1. Torsion test	72
4.2. Test device.....	73
4.3. Evaluation methods	75
4.4. Experimental results for IN 718	77
4.5. Effects of solid solution strengthening	83
4.6. Material models	85
4.6.1. Constitutive analysis.....	85
4.7. Microstructure analysis	87
4.8. Basic creep modelling of Nickel and single-phase Ni based superalloy	91
4.9. Description of pure Nickel	96
4.10. Description of IN718 solutioned alloy	102
4.11. Summary and Conclusions	109
Chapter 5 - Physical Modeling of The Creep Response for Al-Cu-Mg Alloy Produced by Friction Stir Processing.....	111
5.1. Introduction	111

5.2. Creep and Creep testing	113
5.2.1. Phenomenological laws and coefficients	117
5.3. Experimental procedure for AA2024-T3	121
5.4. Results for AA2024-T3	124
5.4.1. Microstructure evaluation during creep	124
5.5. Creep data	136
5.6. Creep modelling of AA2024-T3	139
5.7. Summary and Conclusions	149
Chapter 6 - Conclusions	151
References	154

List of Figures

Chapter 2

Figure 2.1: Typical operating temperatures in high-temperature environments[2].....	8
Figure 2.2: Stress/temperature regimes of high-temperature materials[2].	11
Figure 2.3: Specific strength comparison of high-temperature alloys [2]...	11
Figure 2.4: Typical 0.1% / 100h creep strength for various titanium alloys [2].	12
Figure 2.5: (a) Typical true stress–strain curves for 42CrMo steel under the different deformation temperatures with strain-rate of 0.01s^{-1} ; (b) typical flow stress curve [8].....	14
Figure 2.6: Comparisons between predicted and measured flow stress curves of 42CrMo steel under strain-rates of (a) 0.01s^{-1} and (b) 50s^{-1} [12].	18
Figure 2.7: Tensile strength of superalloys at different temperature ranges[16].....	23
Figure 2.8: Cross section of the Rolls-Royce jet engine (extensive use of nickel-based superalloys in the combustor and turbine sections)[1].....	25
Figure 2.9: Face Centered Cubic (FCC) crystal structure[16].	26
Figure 2.10: Representation of different alloying elements present in Ni base alloys[16]	26
Figure 2.11: The unit cell of γ'' precipitate[16]	28
Figure 2.12: Stress-rupture characteristics of wrought Ni-, Fe-Ni- and Co-based superalloys depending on the strengthening mechanism[3].	31
Figure 2.13: The true stress–true strain curves of IN718 at various strain rates: (a) $\dot{\epsilon}=0.001\text{ s}^{-1}$, (b) $\dot{\epsilon}=0.01\text{ s}^{-1}$, (c) $\dot{\epsilon}=0.1\text{ s}^{-1}$, (d) $\dot{\epsilon}=1\text{ s}^{-1}$ [28].	33
Figure 2.14: The dependence of the peak stress on strain rate at different temperatures: (a) $\ln \sigma_p$ versus $\ln \dot{\epsilon}$, (b) σ_p versus $\ln \dot{\epsilon}$ (c) $\ln(\sinh(\alpha\sigma_p))$ versus $\ln \dot{\epsilon}$. [28].....	34
Figure 2.15: $\ln(\sinh(\alpha\sigma_p))$ versus $1/T$ [28].	35
Figure 2.16: Titanium usage in the aero-engine[4].	36
Figure 2.17: Crystal structure of hcp α and bcc β phase[4].	37
Figure 2.18: Influence of alloying elements on phase diagrams of titanium alloys[4].....	38
Figure 2.19: Schematic quasi-vertical section for ternary titanium alloys containing both α and β stabilising solute elements [4].	39

Figure 2.20: A schematic illustration of microstructures occurring in Ti-6Al-4V after quenching from different temperatures [4].	42
Figure 2.21: Flow curves obtained at 1000 °C (a), 1050 °C (b), 1100 °C (c) at different strain rates [44].	44
Figure 2.22: Relationships among commonly used alloys in the 2xxx series (Al-Cu)[5].	48
Figure 2.23: Relationships among commonly used alloys in the 5xxx series (Al-Mg). Tensile strength (TS) and yield strength (YS) are in ksi unit[5].	49
Figure 2.24: Relationships among commonly used alloys in the 6xxx series (Al-Mg-Si).Tensile strength (TS) and yield strength (YS) are in ksi units[5].	50
Figure 2.25: Relationships among commonly used alloys in the 7xxx series (Al-Zn-Cu-Mg-Cr).Tensile strength (TS) and yield strength (YS) are in ksi units[5].	51

Chapter 3

Figure 3.1: (a) slight barreling as a result of light friction which hinders sliding and (b) severe barreling as a result of high friction which prevents slipping[48].	58
Figure 3.2: Double cone specimens before and after the compression test for (Ti64).	59
Figure 3.3: Representative stress-strain high temperature flow curves of the Ti – 6Al – 4V alloy under different compression deformation conditions: (a) 1050°C; (b)1150°C.	60
Figure 3.4: Strain rate dependence on the peak flow stress with $\alpha = 0.0154 \text{ MPa}^{-1}$.	61
Figure 3.5: Plot used to calculate the activation energy, $\ln [\sinh (\alpha\sigma)]$ vs $1/T$.	62
Figure 3.6: The relationships between the peak stress and the Zener-Hollomon parameter for the calculated peaks; compression test.	63
Figure 3.7: Comparison between the modelled flow curves and experimental data at 0.1 s^{-1} .	65
Figure 3.8: Comparison between the modelled flow curves and experimental data at 1 s^{-1} .	66
Figure 3.9: Comparison between the modelled flow curves and experimental data at 10 s^{-1} .	67

Figure 3.10: Comparison between the modelled flow curves and experimental data at 50 s^{-1}	68
--	----

Chapter 4

Figure 4.1: typical torsion-test specimen[71].....	72
Figure 4.2: Servo controlled, hydraulic torsion test machine.	74
Figure 4.3. Torsion of solid bar specimen[80].	75
Figure 4.4: Specimen for torsion testing and experimental layout for torsion testing.	79
Figure 4.5: Representative flow equivalent-stress vs equivalent strain flow curves obtained by testing the IN718 in torsion.	80
Figure 4.6: Peak flow stress in torsion as a function of the testing strain rate.	81
Figure 4.7: Strain-hardening rate ($\theta = \partial\sigma / \partial\varepsilon$) as a function of flow stress for representative conditions. The Figure also plots the peak stress (σ_p) and the saturation stress(σ_s^*).	82
Figure 4.8: Comparison between the peak flow stress values obtained by testing in torsion single-phase IN718 (this study) and pure-Ni in torsion and compression at 1000 and 1100°C[61][86].....	84
Figure 4.9: Strain rate as a function of $\sinh(\alpha\sigma_p)$, with $\alpha=0.003$	86
Figure 4.10: Calculation of the activation energy for hot working of single-phase IN718.....	86
Figure 4.11: Zener-Hollomon parameter as a function of $\sinh(\alpha\sigma_p)$	87
Figure 4.12: Microstructure of the received alloy (IN 718), heat treatment 1150 °C for 4 h (Light optical microscopy), before a hot torsion deformation.	88
Figure 4.13: Optical images of the IN718 alloy microstructure deformed at: (a) 1100 °C ,1 s ⁻¹ ; (b) 1100 °C, 0,01 s ⁻¹ ; (c)1000 °C; 1 s ⁻¹ ; (d) 1000 °C,0, 01 s ⁻¹	91
Figure 4.14: Peak-flow stress in pure Ni[61]. The curves were calculated by the model equation described in Section 3.6, with $G=(93 \times 10^4 - 36T)[\text{MPa}][96]$, $R_{\max}=570 \text{ MPa}$ ($=1.5R_{\text{UTS}}$), $D=D_{\text{Ni}}=2 \times 10^{-4} \exp(290/RT) [\text{m}^2 \text{s}^{-1}][97]$, $U_{\text{ss}}=\sigma_{\text{ss}}=0$, $p=2$, $q=1$ and $C_L=86$	96

Figure 4.15: Plot of the K_σ term as a function of σ_d/R_{UTS} for $p=2$ and $q=1$, or $p=1$ and $q=0.5$. The boxed area represents the interval of activation energy values obtained in[61].	98
Figure 4.17: a) Peak-flow stress in pure Ni by compression testing[86]; b) steady state creep rate a function of applied stress[98]. The model curves were calculated as in Figure 4.15.	101
Figure 4.18: Plot of the drag stress as a function of applied stress for Al-2%Mg[87]. The curves obtained at different homologous temperatures overlap on a straight line in the low stress regime.	103
Figure 4.19: Peak flow stress as a function of the strain rate for solution treated IN718 ($G=(93 \times 10^4 - 36T)$ [MPa][96], $R_{max}=1215$ MPa ($=1.5R_{UTS}$), $D=D_{Ni}=2 \times 10^{-4} \exp(290/RT)$ [m^2s^{-1}][97], $U_{ss}=30$ kJ mol $^{-1}$, $\sigma_{ss}=0.37\sigma$, $p=1$, $q=0.5$ and $C_L=86$	105
Figure 4.20: Peak flow stress as a function of the strain rate for 1050°C-1 h solution treated IN718[99], with ($G=(93 \times 10^4 - 36T)$ [MPa] [96], $R_{max}=1215$ MPa ($=1.5R_{UTS}$), $D=D_{Ni}=2 \times 10^{-4} \exp(-290/RT)$ [m^2s^{-1}][97], $U_{ss}=30$ kJ mol $^{-1}$, $\sigma_{ss}=0.37\sigma$, $p=1$, $q=0.5$ and $C_L=86$	106
Figure 4.21: Variation of the ultimate tensile strength with solution treatment temperature, for a standard duration of 1h (data from[90]).	108

Chapter 5

Figure.5.1: Schematic of a creep test[108].	115
Figure.5.2: Constant true stress (a) and constant strain rate (b) creep behavior in pure and Class M (or Class I) metals[48].	115
Figure 5.3: Stress and temperature dependence of the steady state creep rate[110].	118
Figure 5.4: Schematic drawing of a) friction stir processing process and b) tool[113].	123
Figure 5.5: Schematic drawing of the Creep specimen[101].	123
Figure 5.6: Microstructure of the FSP 2024-T3 alloy: a) optical micrograph; b) structure observed by TEM.	126
Figure 5.7: Vickers hardness variation along the thickness of the FSP 2024-T3 alloy, measured in the center of the FSP zone. The broken line represents the average HV value.	127
Figure 5.8: Hardness variation as a function of time of exposure (creep test duration) for the sample tested at 250 and 315°C.	128

Figure 5.9: Hardness variation as a function of the temperature-compensated time, with $Q = 260 \text{ kJ mol}^{-1}$. The data substantially overlap on the same sigmoidal curve. The Figure also shows the hardness value for the T3 state, for the alloy after FSP, and for the fully annealed condition[118].	130
Figure 5.10: Representative TEM micrographs of the sample tested under 140 MPa at 250°C. (a) The presence of large intergranular precipitates is well documented; (b), an example of the fine intragranular particles is shown.	131
Figure 5.11: Representative TEM micrographs of the sample tested under 100 MPa at 250°C.	132
Figure 5.12: Representative TEM micrographs of the sample tested under 30 and 50 MPa at 250°C.	134
Figure 5.13: Distribution of the secondary phase particle length, of the samples tested under 30, 100, and 140 MPa at 250°C.	135
Figure 5.14: Representative TEM micrograph of the sample tested under 25 MPa at 315°C.	136
Figure 5.15: Minimum creep rate dependence on applied stress for 2024-T3 FSP alloy, tested both in constant (CLE) and variable (VLE) load conditions. The Figure also shows the strain rate for the base alloy tested by CLE (broken curves).	137
Figure 5.16: Zener-Hollomon parameter as a function of applied stress for 2024-T3 FSP tested under constant load conditions.	138
Figure 5.17: Particle (Orowan) strengthening term as a function of temperature compensated testing time.	145
Figure 5.18: Reciprocal of particle spacing as a function of the Orowan stress at room temperature.	146
Figure 5.19: Basic creep modelling of the minimum strain rate dependence on applied stress for CLE (solid curves) and VLE (broken curves).	148

List of Tables

Chapter 2

Table 2.1: Temperature capability of high-temperature material systems [2].	10
Table 2.2: Mechanical properties depending on temperature for selected Fe-, Ni- and Co based superalloys[3][16].	30
Table 2.3: Standard Terminology and Principle Alloy Element of Aluminum Alloy [5]	46
Table 2.4: Aluminum Alloy Series Designation of Casting Alloys [5]	47

Chapter 3

Table 3.1: Chemical composition of the Ti6Al4V used in this study (in wt.%)	59
--	----

Chapter 5

Table 5.1: chemical composition of AA2024-T3 (wt.%) [101]	122
Table 5.2: Summary of the experimental results. The strain rate values reported in italic font were those of the VLE.	129

Chapter 1.

Introduction

1.1. Thermomechanical Modelling

Flow behavior of the metals during hot forming process is often complex. The hardening and softening mechanisms are both significantly influenced by many factors such as strain, strain rate, and forming temperature. A given combination of thermo-mechanical parameters yields a particular metallurgical phenomenon (microstructure evolution); on the other hand, microstructure changes of the metal during the hot forming process in turn affect the mechanical characteristics of the metal such as the flow stress, and hence influence the forming processes.

Understanding the flow behaviors of metals and alloys at hot deformation condition has a great importance for designers of metal forming processes (hot rolling, forging and extrusion) because of its effective role on metal flow pattern as well as the kinetics of metallurgical transformation (for example, static, dynamic, and metadynamic recrystallization behaviors). In the industrial practice with the help of the FEM simulation, the distribution of stress and strain during the deformation can be analyzed in any part of the work piece.

To obtain accurate simulations and good results, the materials flow stress has to be determined in reliable basic experiments. Some tests like torsion tests, compression tests, etc. have been developed with the aim to characterize the materials flow stress.

The constitutive models are the mathematical representation of the flow behavior of materials, which used to describe the plastic flow properties of the metals and alloys, which are divided into three categories, including the phenomenological and physically-based models, and descriptions by artificial neural networks. The constitutive models are used as input to FE code for calculating the material's response under determined loading conditions. The success of the numerical simulation to accurately reproduce the flow behavior, depends on how accurately the constitutive equation represent the deformation behavior of the metals.

Nonetheless, numerical simulations can be truly reliable only when a proper constitutive model is built. Therefore, based on the experimentally measured data, a number of research groups have made efforts to develop constitutive equations to describe the hot deformation behaviors of metals and alloys. in meanwhile a number of constitutive models have been proposed or modified in recent years to describe the strain rate, stain and temperature-dependent flow behavior of metals and alloys. These models all show that increasing the strain-rate and decreasing the temperature can both enhance the resistance of plastic deformation and cause a rise of the flow stress. For the original constitutive models, there are always some limitations when the authors firstly proposed for their studied materials.

1.2. Project Aims

The aim of this thesis is to investigate the prediction of the dynamic behavior of metals by using a constitutive model (basic creep modelling, Hansel and spittle equation and Garofalo equation), in order to describe the hot deformation behavior. For this purpose, three different metals were considered: The Inconel 718 (age -hardenable nickel-based super alloy), the Titanium Ti-6Al-4V and the commercial AA2024-T3/ Al-Cu-Mg 2024 aluminum alloy. In order to investigate the mechanical response of these metals in dynamic conditions, different experimental techniques were developed and used, microstructural analysis is performed. The experimental data were analyzed through different procedures with the aim to provide consistent methodologies suited to extract sets of model parameters.

1.3. Thesis Outline

Chapter 2 is a review of the literature discussing the metallurgical background of IN 718 Superalloy, titanium (Ti-6Al-4V.) and AA2024-T3 aluminum alloys which included: applications, alloy classification, features and characterization of each alloy, workability and hot deformation behavior.

Chapter 3 discusses the constitutive modeling on the β transus of Ti-6Al-4V alloys at high temperatures and strain rates. The hot compression test was used to investigate the high temperature deformation.

Hensel and Spittel equation was used, peak-flow stress dependence on temperature and strain rate are discussed using a classic phenomenological approach (Garofalo and Arrhenius equations). This Chapter thus outline ones of the classical phenomenological approaches commonly used to describe the high temperature response of advanced materials.

Chapter 4 discusses the hot workability of solution treated for IN718 superalloy. A basic model was applied to pure Ni and then to a single-phase superalloy. Hot torsion tests were used to investigate the high temperature deformation of the superalloy and a solution treated IN718. An alternative physically-based approach, developed for creep of fcc metals, was used for a pure Ni and then to a single-phase superalloy. Microstructure characterization of the torsioned samples, dislocation hardening and solid solution strengthening are all discussed.

Chapter 5 discusses the physical modeling of the creep response for the AA2024-T3 aluminum alloy produced by friction stir processing (FSP). The same constitutive model based on a theoretical approach have been discussed to describe the creep response of this multi-phase material. Microstructural evolution during creep, hardness variation with creep duration, creep rate dependence on applied stress at steady state and the dislocation mobility M are all discussed.

Chapter 6 documents the key conclusions from this work.

Chapter 2.

Literature Review

This chapter begins with an introduction to the high temperature materials (IN718, titanium and its alloys and Aluminum alloys), that were the subjects of this work. Features and characterizations, workability and hot deformation behavior for each alloy has been discussed. The second section discusses the constitutive descriptions for metals and alloys in hot working.

2.1. High Temperature Materials

The subject of high temperature materials is a very broad topic indeed. When a material is used at elevated temperatures, its strength, as reflected in tensile strength, stress rupture life, or fatigue life, is of prime importance. It is also likely that corrosion processes affect strength; therefore, high temperature corrosion resistance is critical. The most demanding applications for high temperature materials are found in aircraft jet engines, industrial gas turbine and nuclear reactor. However, many furnaces, ducting and electronic and lighting devices operate at such high temperature. High temperature materials are mainly used in aircraft engines components, where Ti and Ni based super alloys are important materials to be used for manufacturing the blades and disks[1][2]. Their excellent mechanical properties, even under extreme conditions, come from their two-phase optimized microstructures.

Refractory metals have high strengths at 1200 °C, but oxidation resistance is poor[1][2]. Nickel and cobalt base superalloys have good strengths up to 1000°C with reasonable oxidation resistance[3]. Titanium alloys and some steels can be used to temperatures of about 600 to 700°C[4], Aluminum alloys cannot be subjected to high loads at temperatures much above about 200°C, but fiber-reinforced aluminum has flexural strengths as high as 300 to 400 MPa at 300°C [5].

2.2. The need for high-temperature materials

High-temperature technology is of major importance in many industries including primary metal and nonmetal production, material processing, chemical engineering, transportation and power generation. For many of these industries the price of fuel is a major component of overall operating costs. Materials that allow operation at high temperature are essential for industrial competitiveness because the efficiency of fuel conversion and use is related to operating temperature. Current operating temperatures in various applications are shown in Fig. 2.1, together with the melting temperatures of selected materials [2]. However, no material is capable of operating approximately above 4000°C and thermal ablation must be used at these temperatures. Many industries could benefit from still higher operating temperatures. The temperature of super heater tubes for steam-raising boilers in power plants is currently 560 °C; if this could be increased to 650 °C, efficiency would increase from 35% to 36.5%. This would result in a saving approximately 3.5×10^6 ton of coal per year, i.e. 4% of the total coal used in the United Kingdom for power generation. The use of ceramics-

in diesel engine development in the United States has allowed higher operating temperatures, thus improving efficiency (an increase from 38% to 65% appears possible) and reducing exhaust pollution. Higher temperature operation has a powerful effect on the performance of the gas turbine engine. For example, an increase of 150 °C in turbine entry temperature combined with elimination of internal air cooling of turbine components can give an improvement of around 6% in gas generator thermal efficiency. This order of benefit led to the progressive development of nickel superalloys for gas turbine applications and more recently led to the search for materials with higher temperature capability than the superalloys [1][2].

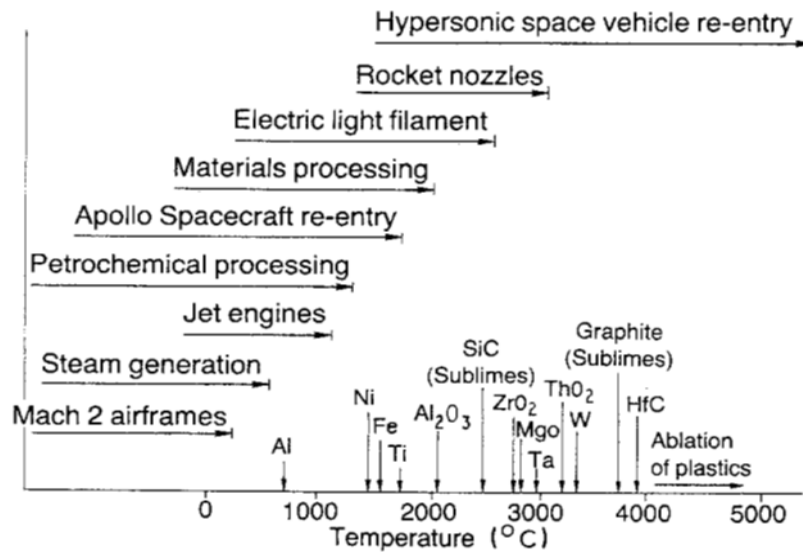


Figure 2.1: Typical operating temperatures in high-temperature environments[2].

2.3. Operating environment

High-temperature materials operate in environments with a wide spectrum of mechanical and chemical conditions. The temperature may be relatively constant (e.g. in continuously operated heat-treatment furnaces) or subject to severe cycling (e.g. in jet engines where the thin edges of turbine blades can experience temperature changes of more than 1000 °C in seconds). The operating stress can vary from very low stress levels in furnace heating elements, for example, to high combined centrifugal and thermal stresses in a gas turbine disc [1][2]. Some measure of inherent oxidation resistance is an essential characteristic of high-temperature materials; however, many applications involve significantly more complex corrosive environments than simple oxidation. In certain types of coal gasification, the atmosphere may be reducing to some extent; thus, alloys that rely on chromium oxide scales for protection do not perform as well as aluminum oxide forming alloys. Oxidation is further modified by atmospheric and fuel contaminants as in, for example, the use of lower grade fuel such as residual fuel oil, instead of higher fractions such as kerosene, in industrial turbines, and boilers. The lower grade fuels contain larger amounts of impurities such as vanadium, Sulphur and sodium which accelerate corrosion. Erosion is an important factor in applications such as fluidized-bed coal combustion. The required life can range from minutes for rocket motor, through 50000 to 100000h for industrial steam and gas turbines, to more than 20 y for large steam turbine installations. Operational stress has a major influence on temperature capability, with the limit being 0.7 to 0.9 of the melting temperatures, T_m , in unstressed applications and 0.3 to 0.7 T_m in stressed-

applications Table 2.1. On the basis of the T_u / T_m factor, aluminum alloys can be considered as high-temperature alloys. Although they can operate up to 300 °C, compared with 580°C for low-alloy steels, this represents a T_u / T_m factor of 0.45 compared with 0.37 for low alloy steels. The broad stress-temperature operational regimes of various materials in stressed applications are illustrated in Fig. 2.2[2]. The strength is based on the 0.2% proof stress for metals and an appropriate proportion of the flexure strength for ceramics and composites. Specific strength Fig. 2.3[2] is an important property in materials for rotating machinery [1][2].

Table 2.1: *Temperature capability of high-temperature material systems [2].*

Material	Approx. max. use temp., T_u (°C)	T_u/T_m	Application
Aluminium (RR350)	300	0.45	Stressed
Low-alloy steel	580	0.37	Stressed
Austenitic steel (A286)	600	0.4	Stressed
Nickel superalloy (MarM002)	1000	0.77	Stressed
Nickel (Brightray H)	1250	0.9	Unstressed
Alummina	1850	0.9	Unstressed
Tungsten	2500	0.74	Unstressed

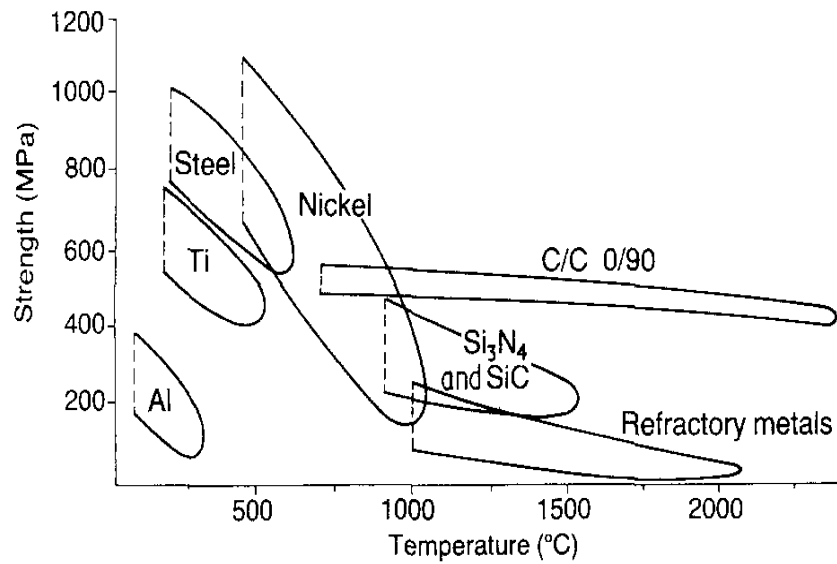


Figure 2.2: Stress/temperature regimes of high-temperature materials[2].

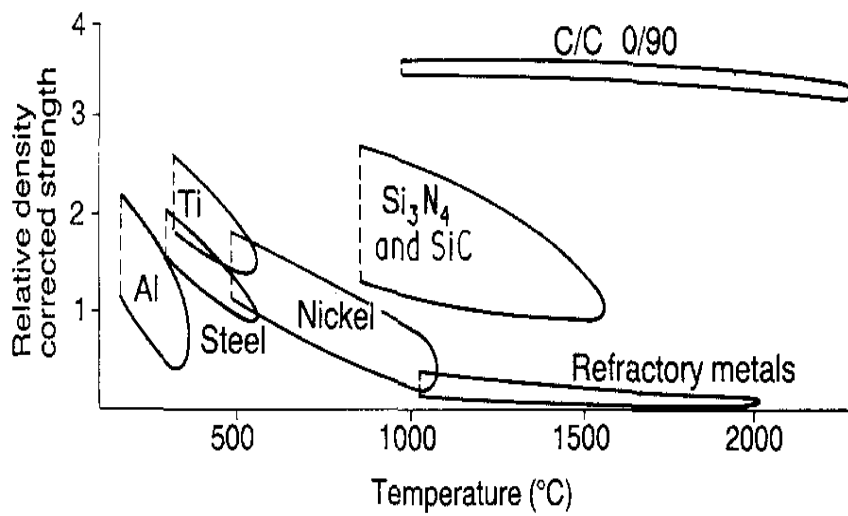


Figure 2.3: Specific strength comparison of high-temperature alloys [2].

The superior specific strength of titanium relative to steel and nickel superalloys provided the motivation for its development for aerospace applications. Major progress has been achieved in increasing the temperature capability of titanium alloys. A recent alloy, IMI829, can be used up to 600 ~ some 250 ~ higher than the early Ti 6-4 alloy Fig. 2.4[2] Despite the fact that the T_u / T_m factor for IMI829 of 0.36 is similar to that for low-alloy steel[1][2].

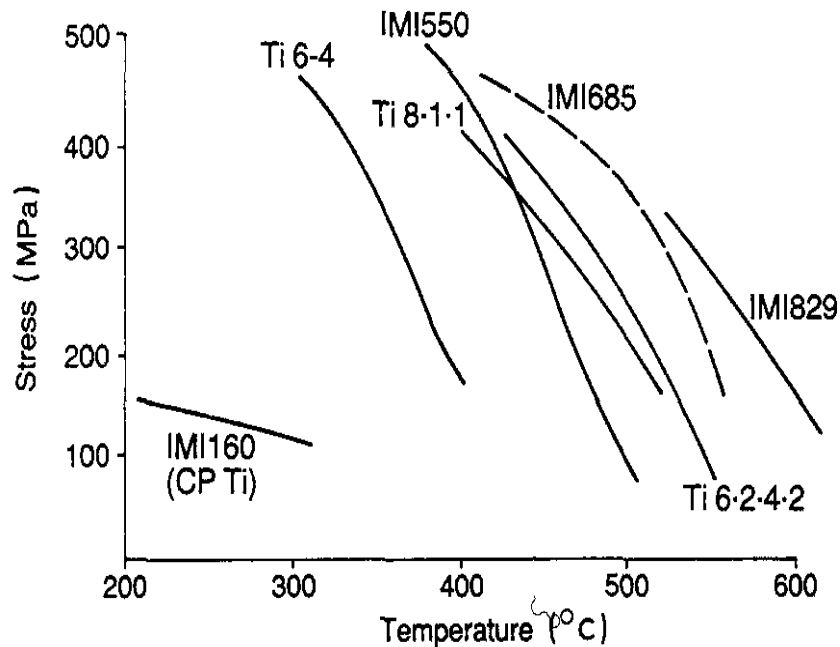


Figure 2.4: Typical 0.1% / 100h creep strength for various titanium alloys [2].

2.4. Constitutive descriptions for metals and alloys in hot working

Flow behavior of materials under the hot deformation process is a very complex affair. Many factors such as strain, strain rate and deformation temperature significantly influence the hardening and softening mechanisms. During hot deformation, the microstructure changes, and this in turn affects the mechanical response of the material. Understanding the flow behaviors of metals and alloys at hot deformation condition has thus, a great importance for designers of metal forming processes (hot rolling, forging and extrusion) because of its effective role on metal flow pattern as well as the kinetics of metallurgical transformation[6][7]. The flow properties of the metals and alloys are described by the constitutive relations that can be used in a computer code to model the forging response of mechanical part members under prevailing loading conditions. So, the numerical simulations can be truly effective only when a proper constitutive model is built. Therefore, much work was done by many researchers to develop reliable constitutive equations, to describe the hot deformation behaviors of metals and alloys. Fig.2.5 a. shows the typical true stress strain curves obtained from the hot compression of 42CrMo steel[8]. The figure shows that the effects of the temperature and strain-rate on the flow stress are significant for all the tested conditions. At small strains, the true stress strain curves exhibit a peak stress (σ_{peak}), while the stress level decreases with increasing deformation temperature and decreasing strain rate ($\dot{\epsilon}$). The flow curves obtained from experiments consist of four different stage,

as shown in Fig. 2.5b[8]. stage I (Work hardening stage), stage II (Transition stage), stage III (Softening stage) and stage IV (Steady stage) [8] .

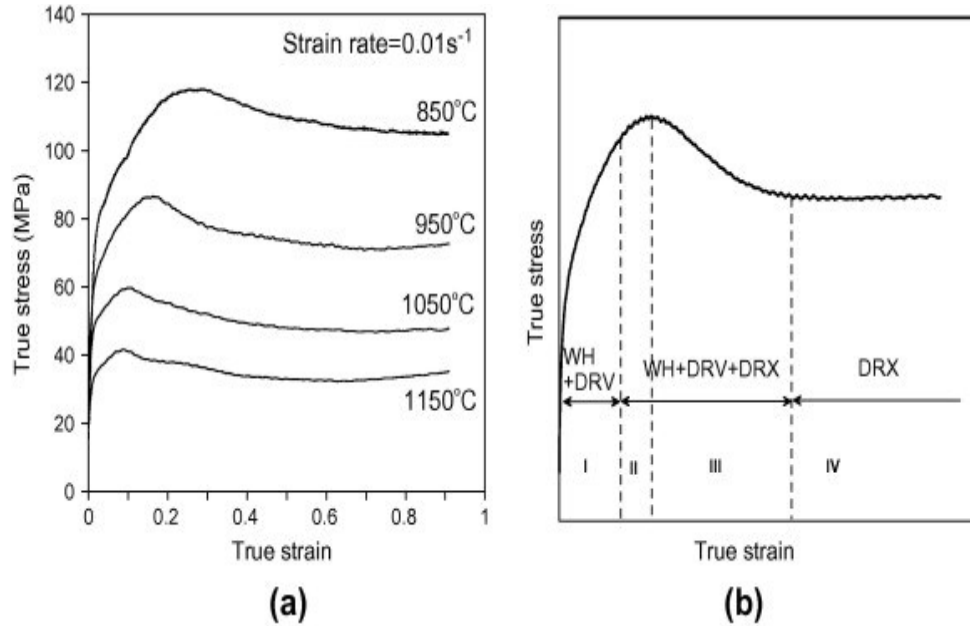


Figure 2.5: (a) Typical true stress–strain curves for 42CrMo steel under the different deformation temperatures with strain-rate of 0.01s^{-1} ; (b) typical flow stress curve [8].

Some constitutive models have been modified, to describe the strain rate, strain, temperature and flow behavior of metals and alloys. The constitutive models are divided into three categories [9][10][11]:

1. Phenomenological constitutive models. They consist of some mathematical functions, that provide the definition of the flow stress-

depending on empirical observations. So, this kind of model is used in a limited applications fields which covering the limited ranges of strain rate and temperature and they exhibit the reduced flexibility. Yet, since phenomenological models are easy to handle, still form the backbone of the libraries of material properties in FEM codes[12].

2. Physical-based constitutive models. This type of model takes into account the physical aspects of material behaviors. The majority of the models are based on the thermally activated dislocation movement theory. Compared to the phenomenological model, they allow an accurate definition of material behavior under wide ranges of loading conditions with some physical assumptions and large number of the material constants. In addition, they are reasonably affective for simple microstructures, but become increasingly complex for alloys in which several micro mechanisms coexist, which is the normal case in practice[12].

3. Artificial neural network (ANN). This approach solves the problems that are very difficult to solve by a normal methods. Therefore, it can provide a different approach for materials modeling than a statistical or numerical method[12].

2.4.1. Arrhenius equation

The Arrhenius equation is widely used especially at high temperature to describe the relationship between the strain rate, flow stress and temperature. The effects of the temperatures and strain rate on the deformation behavior can be then represented by Zener–Hollomon parameter (Z) in a power-law type equation[12].

The hyperbolic law in Arrhenius type equation gives better approximations between Zener–Hollomon parameter and flow stress.

$$\dot{\epsilon} = AF(\sigma) \exp \left(-\frac{Q_{HW}}{RT} \right) \quad (2.1)$$

$$Z = \dot{\epsilon} \exp \left(\frac{Q_{HW}}{RT} \right) \quad (2.2)$$

$$\dot{\epsilon} = A_1 \sigma^{-n'} \exp \left(-\frac{Q_{HW}}{RT} \right) \quad (\alpha\sigma < 0,8) \quad (2.3)$$

$$\dot{\epsilon} = A_2 \exp(\beta\sigma) \exp \left(-\frac{Q_{HW}}{RT} \right) \quad (\alpha\sigma > 1,2) \quad (2.4)$$

$$\dot{\epsilon} = A [\sinh(\alpha\sigma)]^n \exp \left(-\frac{Q_{HW}}{RT} \right) \quad (\text{all}) \quad (2.5)$$

where $\dot{\epsilon}$ is the strain rate (s^{-1}), R is the universal gas constant ($8.3145 \text{ J mol}^{-1} \text{ K}^{-1}$), T is the absolute temperature (K), and Q is the activation energy of hot deformation (J mol^{-1}), A , n' , β and n are the materials constants. α is stress multiplier, MPa^{-1} defined as $\alpha = \beta/n'$ for all stress level. Eq. (2.1) can be represented as shown in Eq.2.5. Then, the flow stress σ can be written as a function of Z parameter, considering the definition of the hyperbolic law given as,

$$\sigma = \frac{1}{\alpha} \ln \left[\left(\frac{Z}{A} \right)^{1/n} + \left[\left(\frac{Z}{A} \right)^{2/n} + 1 \right]^{1/2} \right] \quad (2.6)$$

The lower the Zener–Hollomon parameter is, the larger the extent of flow softening becomes. Moreover, the higher the Zener–Hollomon parameter, the lower the power dissipation rate is. Flow instability occurring under high Zener–Hollomon parameter manifests itself as flow localization.

In the recent years, investigations [13][14][15] established the flow behavior of different metals and alloys during hot deformation by the Arrhenius equation. Lin et al.[6],for example, revised the models to describe the flow behaviors of 42CrMo steel over wide range of forming temperatures and strain-rates by compensation of strain and strain-rate. They found that the values of Q , A , n and α should be expressed as polynomial functions of strain, Eq.2.7.

$$\begin{aligned}
 Q &= E_0 + E_1 \varepsilon + E_2 \varepsilon^2 + E_3 \varepsilon^3 + E_4 \varepsilon^4 + E_5 \varepsilon^5 \\
 \alpha &= C_0 + C_1 \varepsilon + C_2 \varepsilon^2 + C_3 \varepsilon^3 + C_4 \varepsilon^4 + C_5 \varepsilon^5 \\
 n &= D_0 + D_1 \varepsilon + D_2 \varepsilon^2 + D_3 \varepsilon^3 + D_4 \varepsilon^4 + D_5 \varepsilon^5 \\
 \ln A &= F_0 + F_1 \varepsilon + F_2 \varepsilon^2 + F_3 \varepsilon^3 + F_4 \varepsilon^4 + F_5 \varepsilon^5
 \end{aligned} \tag{2.7}$$

In order to accurately predict the flow behavior of the 42CrMo steel, the Zener–Hollomon parameter should be compensated by multiplying both sides of Eq. (2.2) by $\varepsilon^{1/3}$. Then, the modified Zener–Hollomon parameter, Z' , can be expressed as,

$$Z' = \varepsilon^{4/3} \exp \left(\frac{Q_{HW} R}{T} \right) \tag{2.8}$$

Fig. 2.6 [12] shows the comparisons between predicted and measured flow stress curves of 42CrMo steel. It can be easily found that the proposed deformation constitutive equations can gives an accurate and precise estimate of the flow stress for 42CrMo steel, and can be used for the analysis problem of metal forming processes.

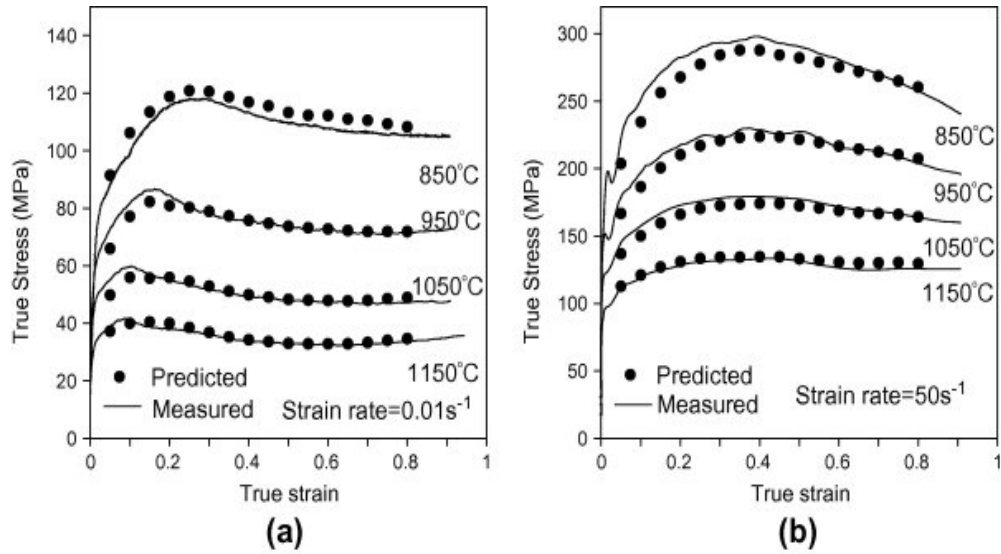


Figure 2.6: Comparisons between predicted and measured flow stress curves of 42CrMo steel under strain-rates of (a) $0.01s^{-1}$ and (b) $50s^{-1}$ [12].

The proposed modifications by Lin et al.[6] was verified by Mandal et al. [15] and Samantaray et al. [14]. Mandal et al.[15] modified the material constants by incorporating fourth-order polynomial function of strains, and their model can accurately predict the high-temperature flow stress of a Ti-modified austenitic stainless steel. Samantaray et al [14].modified them with third-order polynomial function of strains, and their modified constitutive model is effective for describing the high-temperature flow behaviors of modified 9Cr–1Mo (P91) steel. In addition, this modification method by strain compensation is also useful for the aluminum alloy [13].The examples mentioned above are typical of empirical models developed to describe a single material, which can be useful for the specific case, But are of little-

interest when one considers different alloys or even the same material with a different microstructure.

2.5. The material for high temperature application: what is the superalloy?

A superalloy, or high-performance alloy, is an alloy that exhibits an excellent mechanical strength, creep resistance, good surface stability, and corrosion resistance. The face-centered cubic is the crystal structure, some examples for such alloys are Hastelloy, Inconel, Waspaloy, Rene alloys, Incoloy, MP98T, TMS alloys, and CMSX single crystal alloys. Superalloys develop high temperature strength through solid solution strengthening. Precipitation strengthening is an important strengthening mechanism, which forms secondary phase precipitates such as gamma prime and carbides. Aluminum and chromium give a good corrosion resistance, so this mean that the primary applications for such alloys is in the hot sections parts of the aircraft engines[1][16].

2.5.1. Classification of superalloys

The Superalloys are classified into three categories, depending on the main metal present in the alloy:[16] [17]

- Iron-based superalloys
- Nickel-based superalloys
- Cobalt-based superalloys

2.5.1.1. Iron-based superalloy

Iron-based super alloys were developed from austenitic stainless steels and are based on the principle of combining a closed-packed FCC matrix with both solid-solution hardening and precipitate forming elements. The austenitic matrix is based on nickel and iron, with at least 25% Ni needed to stabilize the FCC phase [17]. Other alloying elements, such as chromium, partition primarily to the austenite for solid solution hardening. These alloys are less expensive than cobalt and nickel-based superalloys, and can be classified into three types: alloys that can be strengthened by a martensitic type of transformation, alloys that are austenitic and are strengthened by a sequence of hot and cold working (usually, forging at 1093.3 to 1148.8 °C followed by finishing at 648.8 to 871.1°C) and austenitic alloys strengthened by precipitation hardening. The last group can be considered as a superalloy, the other are usually categorized as high temperature and high strength alloys. The martensitic types are mainly used at temperatures below 537.7 °C and the austenitic types are used above 537.7 °C [17][18].

The AISI 600 series of superalloys consists of six subclasses of iron-based alloys[16]:

- 601 through 604: Martensitic low-alloy steels.
- 610 through 613: Martensitic secondary hardening steels.
- 614 through 619: Martensitic chromium steels.

- 630 through 635: Semi-austenitic and Martensitic precipitation-hardening stainless steels.
- 650 through 653: Austenitic steels strengthened by hot/cold work.
- 660 through 665: Austenitic superalloys; All grades except alloy 661 are strengthened by second-phase precipitation.

Iron-based super alloys give a good high temperature as well as room temperature strength and resistance to creep, oxidation, corrosion, and wear. The wear resistance increases by the carbon content. Alloys 611, 612, and 613, have a maximum wear resistance which are used in high-temperature aircraft bearings and sliding machinery parts. The martensitic chromium steels, particularly alloy 616, are used for steam-turbine blades. Austenitic alloys are more difficult to machine than martensitic types, which can be better machined in the annealed condition. The most of the martensitic steels are difficult to weld because of the crack sensitivity. These alloys should be annealed or tempered prior to welding; also, pre-heating and post-heating are recommended [17][18].

2.5.1.2. Nickel-base superalloys

Nickel-base superalloys are very complex, widely used for the hottest parts, and, for many metallurgists, the most interesting of all superalloys[17]. They currently constitute over 50% of the weight of advanced aircraft engines[19].

The high phase stability of FCC nickel matrix gives a principal characteristic and the capability to be strengthened by a variety of direct and indirect means. So, chromium and aluminum are improve the surface at ability of nickel [20]. Nickel 'based superalloys are extensively used in aerospace industry, for the manufacture of gas turbines in military and commercial aircraft, due to their high corrosion resistance, high strength and long creep life at elevated temperature[21]. Ni-base superalloys can be divided into three types[16]:

- Solid solution strengthened alloys, such as Haynes 230 and HastelloyX, which usually contains the following alloying elements: Fe, Co, Cr, Mo, W, Ti, Nb and Al. Among these Al, Cr, W and Mo are potential solid–solution strengtheners because of different atomic radius as compared to Ni. They are more suitable for processing, for example Mby welding and can also be manufactured into complex geometries from powders using laser melting techniques.
- Precipitation (age) hardened alloys, such as In718, 738, 939 and Waspalloy. Usually they contain Al, Ti, Ta and sometimes Nb that facilitate the formation of γ' and γ'' precipitates in the γ matrix. From figure 2.7[16], it is evident that precipitation hardened alloys possess higher strengths compared to solid solution strengthened alloys and are widely used in high temperature applications.
- Oxide dispersion strengthened (ODS) alloys: they are alloys that contain fine oxide particles of Y_2O_3 about 0.5 to 1%.

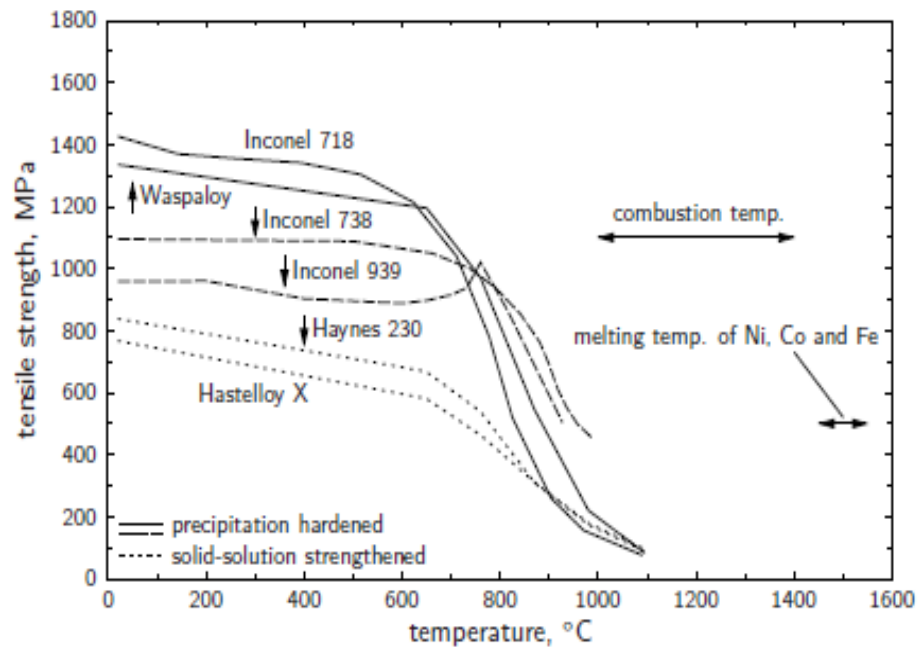


Figure 2.7: Tensile strength of superalloys at different temperature ranges[16].

Nickel-based superalloys can be subdivided in many categories, depending on their composition, below are listed the types and some of the applications[16]:

- Inconel Alloy 600 (76Ni-15Cr-8Fe), used for construction of nuclear reactors & chemical industry;
- Nimonic alloy 75 (80/20 nickel-chromium alloy with additions of titanium and carbon), used in gas turbine and heat-treatment equipment;
- Alloy 601. Lower nickel (61%) content with aluminium and silicon additions, used aerospace, and power generation;

- Alloy X750. Aluminium and titanium additions for age hardening. Used in gas turbines, rocket engines and aircraft structures;
- Alloy 718. (55Ni-21Cr-5Nb-3Mo). Niobium addition to overcome cracking problems during welding. Used in aircraft and land-based gas turbine engines and cryogenic tanks;
- Alloy X (48Ni-22Cr-18Fe-9Mo + W). High temperature flat-rolled product for aerospace applications;
- Waspaloy (60Ni-19Cr-4Mo-3Ti-1.3Al). Proprietary alloy for jet engine applications;
- ATI 718Plus. A lower cost alloy which exceeds the operating temperature capability of standard 718 alloy by 100 F° (55 C°) allowing engine manufacturers to improve fuel efficiency;
- Nimonic 90. (Ni 54% min Cr 18-21% Co 15-21% Ti 2-3% Al 1-2%) used for turbine blades, discs, forgings, ring sections and hot-working tools;
- Rene' N6. (4Cr-12Co-1Mo-W6 -Ta7- Al5.8 - Hf 0.2 - Re5- BalNi) 3rd generation single crystal alloy used in jet engines;
- TMS 162 (3Cr- 6Co-4Mo-6W-6Ta-6Al-5Re-6Rubalance Ni) 5th generation single crystal alloy for turbine blades.

2.6. Application of Superalloys

The superalloys are mainly used in the high temperature applications, including components for aircraft[20]. Fig.2.8. shows the materials for the aircraft engine, the huge used of this alloy are in (a)gas turbines; like disks, combustion chambers, bolts, casings and blades, (b) space vehicles and rocket engine parts, (c) Nuclear applications[22].

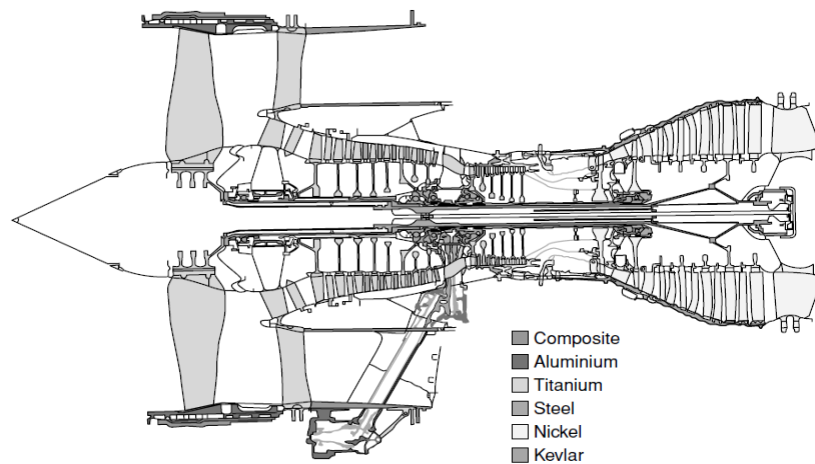


Figure 2.8: Cross section of the Rolls-Royce jet engine (extensive use of nickel-based superalloys in the combustor and turbine sections)[1].

2.7. Physical metallurgy of nickel and its alloys

Nickel is one of the most widely used elements on earth and has a Face Centered Cubic (FCC) crystal structure as shown in Fig. 2.9[16]; it belongs, to the family of transition metals and exists in the form of five stable-isotopes. The elements that are alloyed with Ni to form superalloys and the phases they contribute to also is mentioned in the Fig. 2.10[16]. The melting temperature is 1455 °C and has a density of 8907 kg/m³ at room temperature. The low diffusion rate in FCC metals give good microstructural stability even at very high temperatures [1].

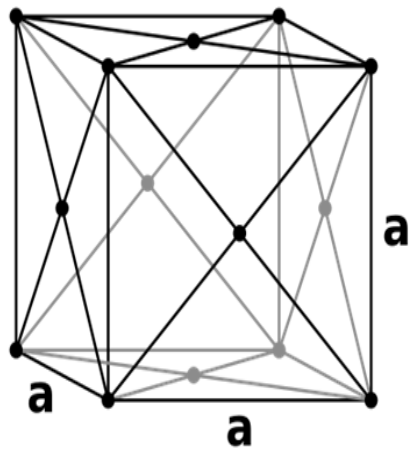


Figure 2.9: Face Centered Cubic (FCC) crystal structure[16].

IIA	IIIA	IVB						
	B 0.097	C 0.077						
	Al 0.143		IVA	VA	VIA	VIIA	VIIIA	VIIIA
		Ti 0.147	V 0.132	Cr 0.125		Fe 0.124	Co 0.125	Ni 0.125
	Y 0.181	Zr 0.158	Nb 0.143	Mo 0.136		Ru 0.134		
		Hf 0.159	Ta 0.147	W 0.137	Re 0.138			

γ' former
 Minor alloying additions
 γ former

Figure 2.10: Representation of different alloying elements present in Ni base alloys[16] .

Ni based superalloys belong to the family of austenitic nickel chromium based materials that typically contains 80% Ni and 20% Cr. Several alloying elements are included in different percentages depending on the need to achieve better mechanical properties. Ni based alloys are usually strengthened by precipitation (age) hardeners, they may be wrought or cast depending on the application and composition involved [17]. The microstructure consists of different phases. The important ones such as gamma phase (γ), gamma prime (γ'), gamma double prime (γ''), delta phase (δ) and various carbides and borides are explained below [1]. The gamma phase (γ): The gamma phase is the matrix phase of nickel-based superalloys in which the other phases reside[1][16].

It exhibits an FCC crystal structure and its composition mainly consist of Ni with other elements such as Co, Cr, Mo, Ru, Re, & Fe[1][16].

Gamma prime (γ'): forms the precipitate phase, which is usually coherent with the γ -matrix and is the main strengthening precipitate in nickel-based superalloys. Similar to the γ phase γ' have an ordered FCC crystal structure. γ' mainly consist of Ni, Al, Ti, and Ta i-e $\text{Ni}_3(\text{Al,Ti})$ [1][16].

Gamma double prime (γ''): is a strong coherent metastable precipitate with a body center tetragonal (BCT) structure, it is the primary strengthening precipitate[1][16].

The γ'' unit cell precipitate i-e Ni_3Nb consist of Ni and Nb is shown in Fig.2.11[16], is usually found in Ni-Fe superalloys. At higher temperature γ'' become unstable and can transform into δ phase[1][16].

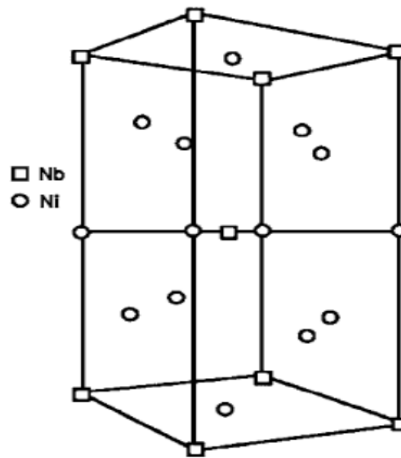


Figure 2.11: The unit cell of γ'' precipitate[16] .

Delta phase (δ): is a non-hardening precipitate usually present at grain boundaries. The loss of hardening is due to depletion of γ'' . The structure is orthorhombic and the δ phase improves the creep rupture and grain boundary sliding resistance. It is composed mainly of Ni, Nb and Ti.

Carbides and borides: Carbide usually forms when carbon reacts with Ti, Ta and Hf and result in MC carbides, where M represents elements such as Cr, Mo, Ti, Ta, or Hf. The MC carbides break down during service to other species, such as $M_{23}C_6$, M_6C , M_7C_3 , and M_3B_2 . These decomposed compounds usually reside in the γ grain boundaries. Borides are found in superalloy in the form of M_3B_2 , having a tetragonal unit cell. Which is also present in grain boundaries and improve the creep rupture resistance of superalloys[1][16].

2.8. Inconel 718: Features and characterization

Inconel 718 alloy is an age-hardenable Ni-Cr-Fe based wrought superalloy, it is extensively used in the aerospace industry due to its high corrosion and oxidation resistance, high strength and long creep life at elevated temperatures [23]. Inconel 718 has a good machinability and welding capability in comparison with other superalloys [1]. Fig 2.12 shows the comparison of creep strength for all three types of superalloys with different type of strengthening[1][16]. Nickel based alloys, have a relatively high yield (700–1200 MPa) and tensile (900–1600 MPa) strength at room temperature, the most remarkable property is that they maintain their mechanical properties within a wide range of temperatures, (up to 600–800 °C)[16][17]. The mechanical properties (Table 2.2) depend on the chemistry and the microstructural features, such as grain size, γ'/γ'' size and distribution, carbide and boride size and content, and grain boundary morphology. The metastable phase may finally transform into the stable phase δ (Ni_3Nb) at temperatures above 650 °C after long term thermal exposure[1]. During the hot forming process, the high-temperature deformation behavior of metals or alloys is generally very complex[20]. It is well known that the hot deformation behavior is sensitive to the thermo-mechanical parameters, such as the deformation temperature (T), strain rate ($\dot{\epsilon}$) and strain (ϵ)[24][25]. Complex deformation mechanisms, such as the work hardening (WH), dynamic recovery (DRV) and dynamic recrystallization (DRX), often occur in the metals or alloys with low stacking fault energy during the hot deformation [20].

For the multi-pass hot forming process, the static and metadynamic recrystallization behavior also occurs. At the beginning of hot deformation, the obvious work hardening behavior can often be observed for the low stacking fault energy alloy. So, actually the high temperature deformation is a competitive process of the strain hardening and dynamic softening mechanisms. Therefore, developing the suitable constitutive relations to describe the complex strain hardening and dynamic softening behavior of metals or alloys are significant [20].

Alloy	UTS (MPa) at temperature			Y.S. (MPa) at temperature			Tensile elongation (%) at temperature		
	21 °C	540 °C	760 °C	21 °C	540 °C	760 °C	21 °C	540 °C	760 °C
Ni based									
Astroloy	1415	1240	1160	1050	965	910	16	16	21
Inconel 587®	1187	1035	830	705	620	605	28	22	20
Inconel 600	660	560	260	285	220	180	45	41	70
Inconel 718	1435	1275	950	1185	1065	740	21	18	25
Nimonic 75	745	675	310	285	200	160	40	40	67
Nimonic942®	1405	1300	900	1060	970	860	37	26	42
René 95	1620	1550	1170	1310	1255	1100	15	12	15
Udimet 720	1570	...	1455	1195	...	1050	13	...	9
Fe-Ni based									
A -286	1005	905	440	725	605	430	25	19	19
Alloy 901	1205	1030	725	895	780	635	14	14	19
Incoloy 801 ®	785	660	325	385	310	290	30	28	55
Incoloy 909	1310	1160	615	1020	945	540	16	14	34
Co based									
Haynes 188	960	740	635	485	305	290	56	70	43
MP159	2025	1620	10

Table 2.2: Mechanical properties depending on temperature for selected Fe-, Ni- and Co based superalloys[3][16].

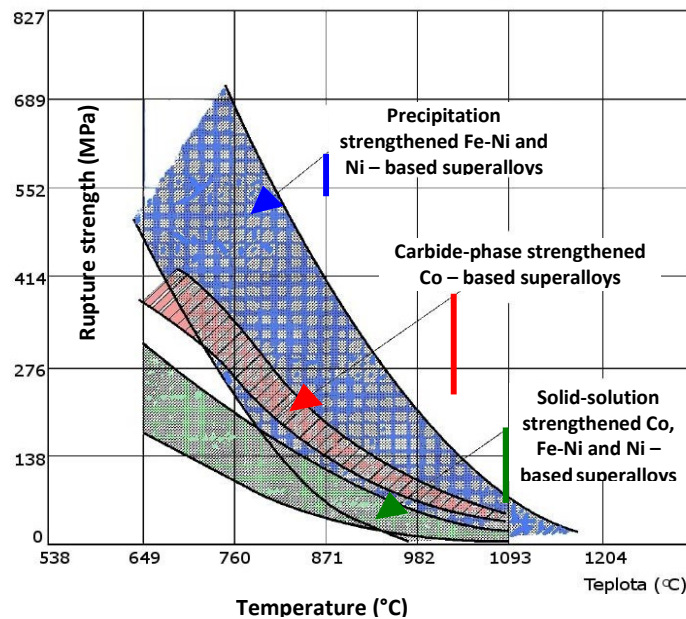


Figure 2.12: Stress-rupture characteristics of wrought Ni-, Fe-Ni- and Co-based superalloys depending on the strengthening mechanism[3].

2.9. Workability and hot deformation behavior of IN718

The hot deformation behavior of IN718 is usually investigated by using hot compression and torsion tests.[26][27][28]. Several models have been proposed in the form of a hyperbolic-sine[29], an exponential and a power law for hot compression of IN718[30]. Experimental data obtained by J.M. Zhang et al[31], who analyzed the shape of the flow stress curves vs. deformation parameters, to develop a mathematical model.

Recently, M.Z. Hussain et al.[32] proposed a constitutive relationship for thermo-mechanical processing of IN718 through double multivariate nonlinear regression. Considering hot deformation of IN718, it is worth noting that it is essential to develop comprehensive equations for a wide range of temperature (T) and strain rate ($\dot{\epsilon}$). The mechanical properties of the alloy generally depend on the microstructure which is controlled by hot deformation parameters such as temperature, strain and strain rate. So, the Arrhenius-type equation and processing map could play important roles in characterization of flow stress behavior, optimization of process parameters and microstructure control for metals and alloys during hot deformation. Tan et al.[20] studied the hot deformation behavior of fine grained Inconel 718 superalloy. The flow stress values predicted by the developed Arrhenius-type constitutive equation were in reasonable agreement with the experimental values, and optimum process parameters were determined based on the established processing maps. The hot working characteristics of Ni-Cr-Mo-based C276 superalloy based on the flow stress curves and microstructure were investigated by Zhang et al[21]. Fig. 2.13[28] shows the true stress–true strain curves obtained from the Gleeble tests.

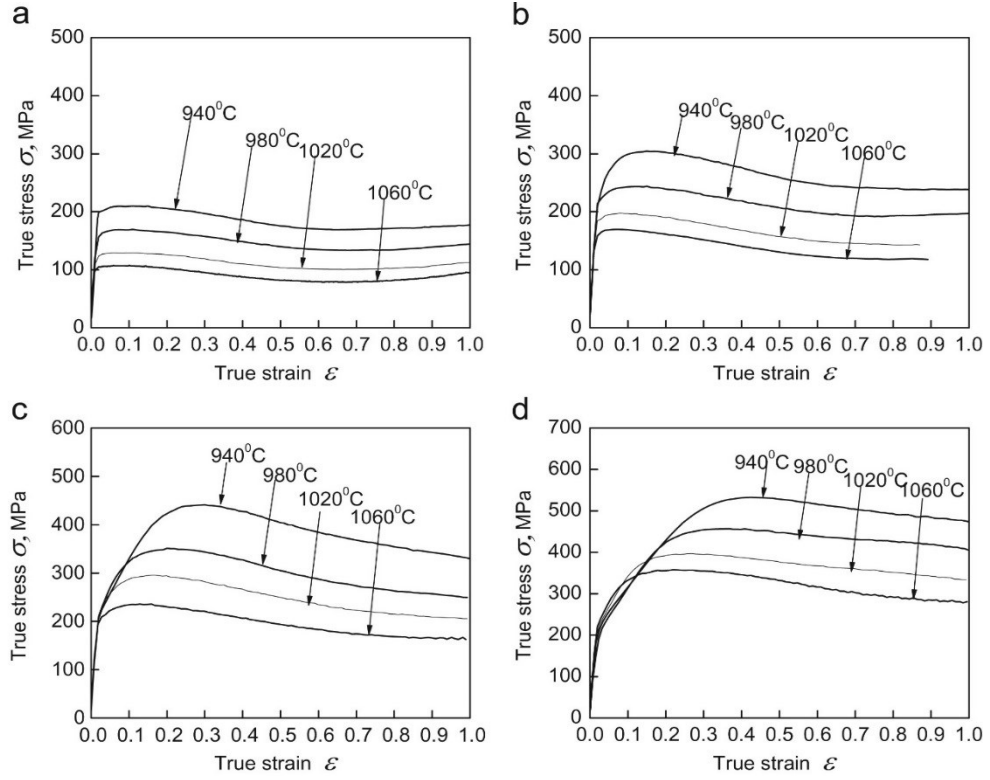


Figure 2.13: The true stress–true strain curves of IN718 at various strain rates: (a) $\dot{\epsilon}=0.001 \text{ s}^{-1}$, (b) $\dot{\epsilon}=0.01 \text{ s}^{-1}$, (c) $\dot{\epsilon}=0.1 \text{ s}^{-1}$, (d) $\dot{\epsilon}=1 \text{ s}^{-1}$ [28].

Fig. 2.14[28]. Shows the the relationship between $\ln \sigma_p$ and $\ln \dot{\epsilon}$ and the relationship between $\ln(\sinh(\alpha\sigma_p))$ and $\ln \dot{\epsilon}$ that are analysed within a value of n_1, β and n_2 are 6.6, 0.0247 and 4.9, respectively. The value of the activation energy (Q) was 429.56 KJ/mol (Fig. 2.15) [28].

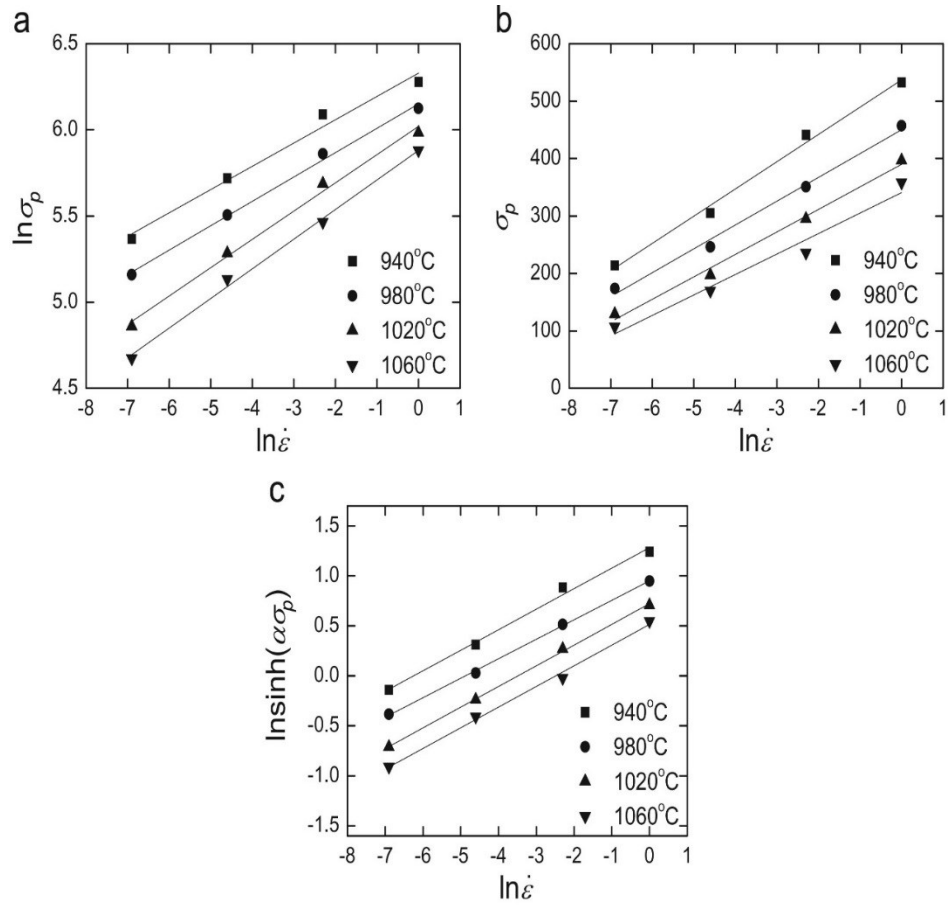


Figure 2.14: The dependence of the peak stress on strain rate at different temperatures: (a) $\ln \sigma_p$ versus $\ln \dot{\epsilon}$; (b) σ_p versus $\ln \dot{\epsilon}$ (c) $\ln(\sinh(\alpha \sigma_p))$ versus $\ln \dot{\epsilon}$. [28].

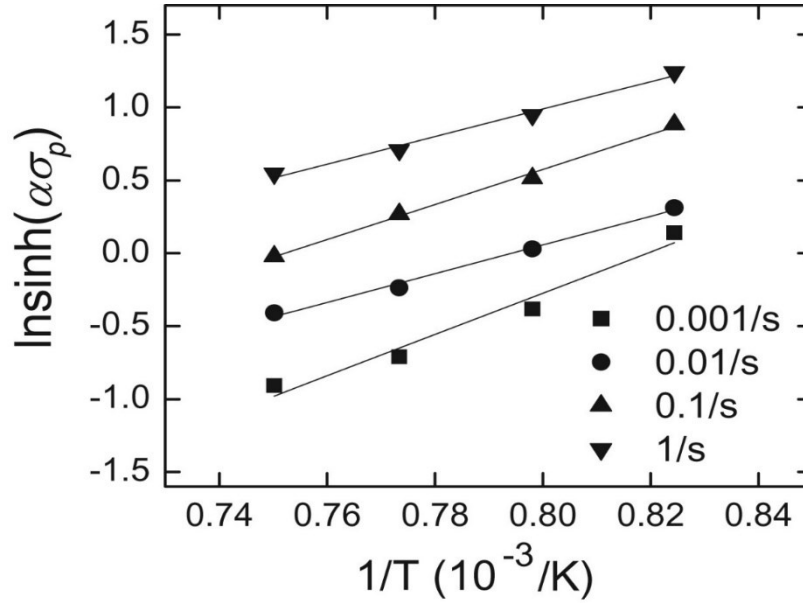


Figure 2.15: $\ln(\sinh(\alpha\sigma_p))$ versus $1/T$ [28].

2.10. Titanium Alloys

Titanium alloys are widely used in aerospace, primarily due to excellent strength to weight ratio and good high temperature properties. The high strength, coupled with low density (60% of that of steel) offer attractive weight saving[4]. For example, the landing gear of the Boeing 777 and the Airbus A380 achieved weight savings of over 580 kg by substituting certain struts, rods and beams of steel (4340M) for the titanium alloy Ti-10V-2Fe-3Al. Due to its corrosion and temperature resistance, titanium can be widely used in Jet engine component, airframes casing [33][34].

It's very interesting also to note that using titanium in landing gear; can reduce the maintenance costs. Specific Titanium alloys have been designed to operate at over 600°C. Other advantages of titanium alloys for aerospace applications include their compatibility with carbon fiber reinforced polymer (CFRP); low modulus of elasticity and high ballistic resistance. Fig. 2.16. shows the typical titanium alloy usage in the aero-engine[35].

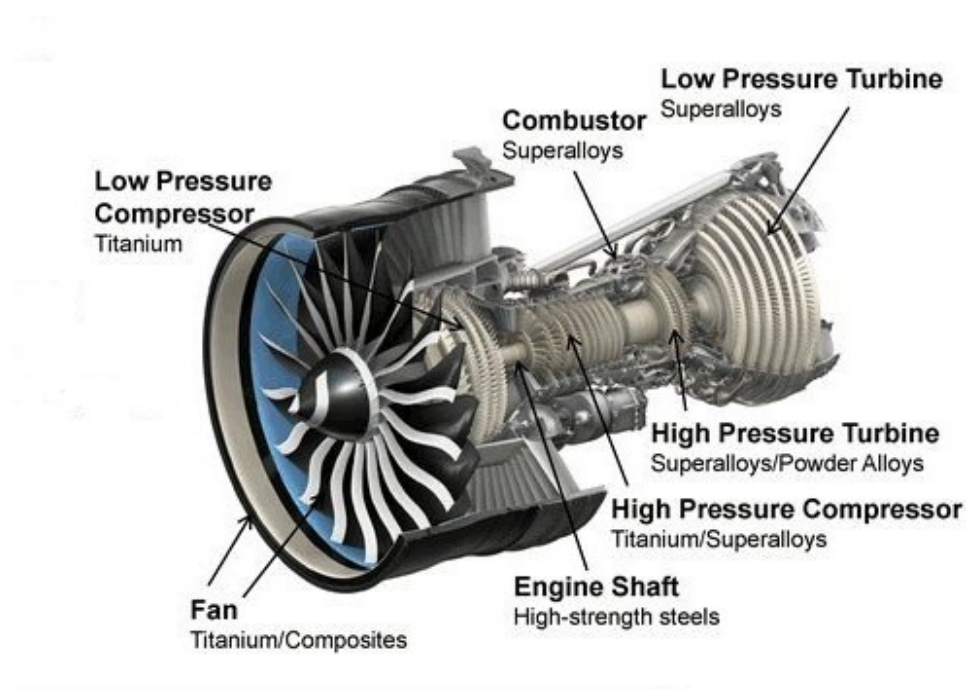


Figure 2.16: Titanium usage in the aero-engine[4].

Titanium alloys find interesting applications also in chemical industry (e.g. reaction vessels) due to their corrosion resistance, and also in heat exchangers. Beside of the chemical and aerospace applications, titanium alloys can be used also in other sectors, like marine and offshore applications. The sports car industry uses titanium alloys for coil springs and engine valves because of its high strength to weight ratio. Furthermore, Titanium alloys also find their use in medical applications such as hip and dental implants due to its biocompatibility [4].

2.10.1. Classification of titanium alloys

Titanium has a two elemental crystal structures, hexagonal close packed (hcp) at room temperature and body centered cubic (bcc) at higher temperatures (Fig.2.17)[4]. These two systems are the basis for the five classes of titanium alloys: α , near- α , $\alpha+\beta$, near- β and β . The temperature at which the material transforms to 100% β is known as the β transus temperature (T_β) [35].

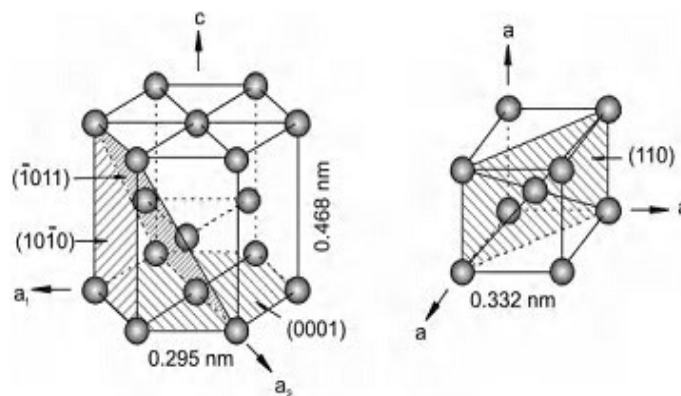


Figure 2.17: Crystal structure of hcp α and bcc β phase[4].

Properties such as plastic deformation and diffusion rate are closely connected with the respective crystal structure. Fig.2.18[4] classifies the alloying elements as neutral, α -stabilisers or β -stabilisers depending on their influence on T_{β} [4].

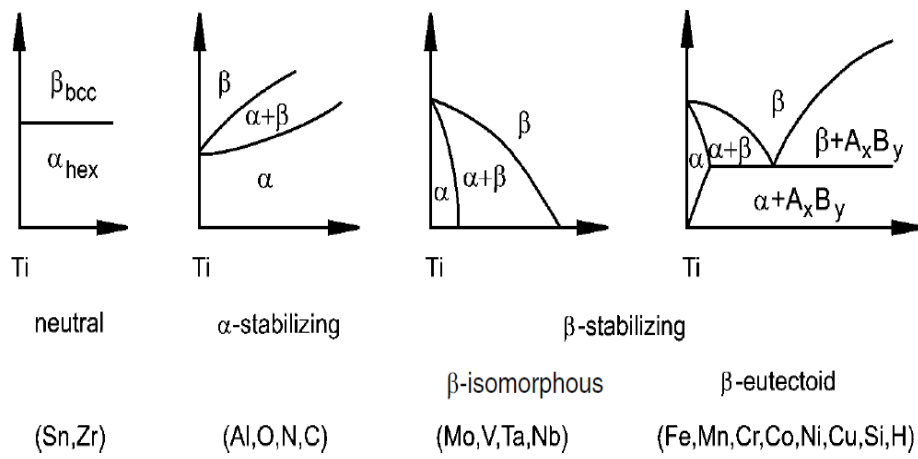


Figure 2.18: Influence of alloying elements on phase diagrams of titanium alloys[4].

The α phase field is extended to higher temperatures by α -stabilising elements, while the β phase field is shifted to lower temperatures by β - stabilising elements. Neutral elements have a negligible effect on T_{β} . Examples of α stabilisers include Al, O and N, and β stabilisers include Mo, Cr, Mn, V and Fe. [35]. Fig. 2.19 shows a schematic quasi-vertical section of a ternary titanium system containing both α and β stabilising solute species. The schematic shows the martensitic start and finish lines denoted-

as M_s/M_f which are close together. The classes of titanium alloy are marked at the top of the diagram [4].

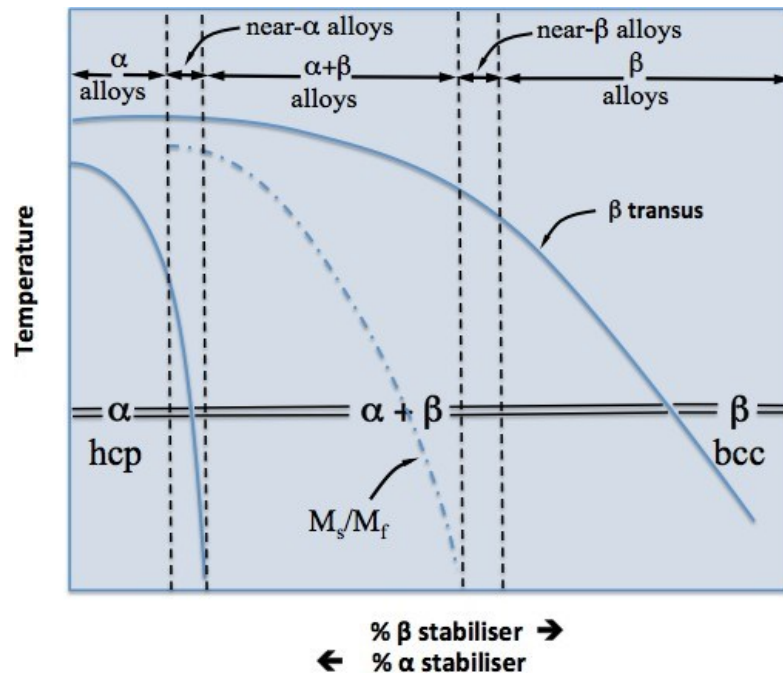


Figure 2.19: Schematic quasi-vertical section for ternary titanium alloys containing both α and β stabilising solute elements [4].

2.10.1.1. α alloys

Mainly consist in pure titanium (commercially pure Titanium), Ti-5Al-2.5Sn and Ti-0.3Mo-0.9Ni. This class of alloys is mostly α phase with a very small volume fraction (few per cent maximum) of β . Small alloying addition gives the α alloys an excellent weldability.

Furthermore, contrary to $\alpha+\beta$ and β alloys, thermomechanical processing is used to control the grain size rather than manipulate the microstructure. In addition to their high weldability, α alloys exhibit excellent corrosion resistance. For this reason, commercially pure Titanium is the material of choice for manufacture of chemical and petrochemical processing equipment [4][36]. The weldability is useful in heat exchangers and other piping applications.

2.10.1.2. $\alpha+\beta$ alloys

Ti-6Al-4V (Ti-64) is the most popular titanium alloy in the aerospace industry. Today this type of ($\alpha+\beta$) alloy accounts for more than 50% of all alloys in use and for near 90% of the titanium used in the aerospace market. Ti-64 can be heat treated up to tensile strengths of 1100 MPa via a solution treatment and aging process. These alloys have the best combination of processability, strength, ductility and durability [36][37]. Ti-64 is weldable by almost all welding methods too. So, Ti-64, is used in almost every section of the aircraft including the fuselage, wing, empennage, nacelle and landing gear, usually in the annealed condition[4][38].

2.10.1.3. β alloys

β - alloys contain an extremely high concentration of β stabilizing elements which results in the β phase being thermodynamically stable at room temperature. An example of a β alloy is Ti-13V-11Cr-3Mo. β alloys give a high tensile and fatigue strengths along with easy fabrication into sheet-

type products. On the other hand, the disadvantages are low resistance to crack propagation and poor weldability[4][37].

2.11. Ti-6Al-4V features and characterization

Ti6Al4V is an $\alpha+\beta$ alloy, with 6 wt% aluminium stabilizing the α phase and 4 wt% vanadium stabilizing the β phase. At room temperature the microstructure at equilibrium consists mainly of the α phase (hcp) with some retained β phase (bcc) [39]. Ti6Al4V provides a good machinability and excellent mechanical properties, which offer the best performance for a variety of weight reduction applications in aerospace, automotive and marine equipment, racing and aerospace industry[38][40]. The Heat Treatment by hot Isostatic Pressing (HIP) is recommended for fatigue-loaded components. The higher the solution heat treatment temperature, the smaller is the vanadium enrichment in the β phase [41], leading to transformation into hexagonal α' upon quenching (from temperatures above 900°C)[33]. Fig.2.20[4] is a schematic illustration of the microstructures resulting from quenching from various temperatures. The figure attempts only to illustrate the principle transformations upon quenching; in reality mixtures of both α' , α'' and metastable/stable β can occur, depending on chemical compositional variations[4].

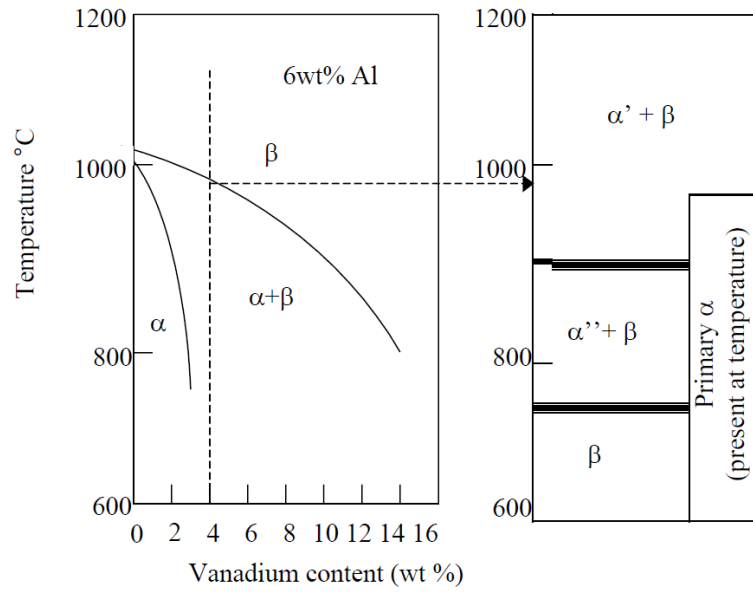


Figure 2.20: A schematic illustration of microstructures occurring in Ti-6Al-4V after quenching from different temperatures [4].

The β – phase contains lower concentration of those elements (especially oxygen) that promote age hardening by formation of coherent Ti_3Al particles[4]. The mechanical properties of Ti-6Al-4V are also affected by the texture of the alpha phase[38]. Forming processes are usually performed by hot rolling or hot forging in the β phase field or in the $\alpha+\beta$ phase field which generally induces relatively sharp textures in the α phase formed upon cooling[39]. Different investigations have been carried out to study the influence of the deformation parameters on microstructures and texture[36].

In the hot rolled of Ti-6Al-4V products, N. Gey et. al. found that the degree of deformation in the β field (high temperature) significantly affects the inherited resulting α texture[39]. Albrecht et. al. made some well-defined comparisons between mechanical properties and texture for Ti-6Al-4V[42]. Their work shows that the orientation of the basal plane with respect to the loading direction is of primary importance.

2.12. Workability and hot deformation behavior of Ti-6Al-4V

Also in the case of titanium alloys, the hot workability is studied by using hot compression or hot torsion tests[43][44]. With hot torsion it is possible to apply large deformations while keeping the sample length constant[44]. Hot compression tests are suitable for determining material behavior at low strains[45]. The hot behavior of the Ti6AL4V was already investigated by Reddy[46], who limited his study on low strain-rates and low strains obtained during hot compression. Steady-state flow stress was also modeled by mean of regression for strain-rate up to 10/s taking into account the initial grain size. Prasad et al. investigate the Mechanisms of deformation of Ti-6Al-4V in the β phase domain using a hot compression; also he used an Arrhenius type equation to model the steady state flow stress; the prior β grain size was also modeled as a function of the Zener-Hollomon parameter using a power law[47]. Fig. 2.21[44] shows the flow curves for the torsion results under different strain rate; the steady-state flow stress and the maximum stress increase by increasing the strain rate and decrease by increasing the temperature.

During hot torsion of Ti-6Al-4V, different deformation modes were observed according to the allotropic form: dynamic recrystallization for the $\alpha + \beta$ phase domain and dynamic recovery for the β phase domain [44].

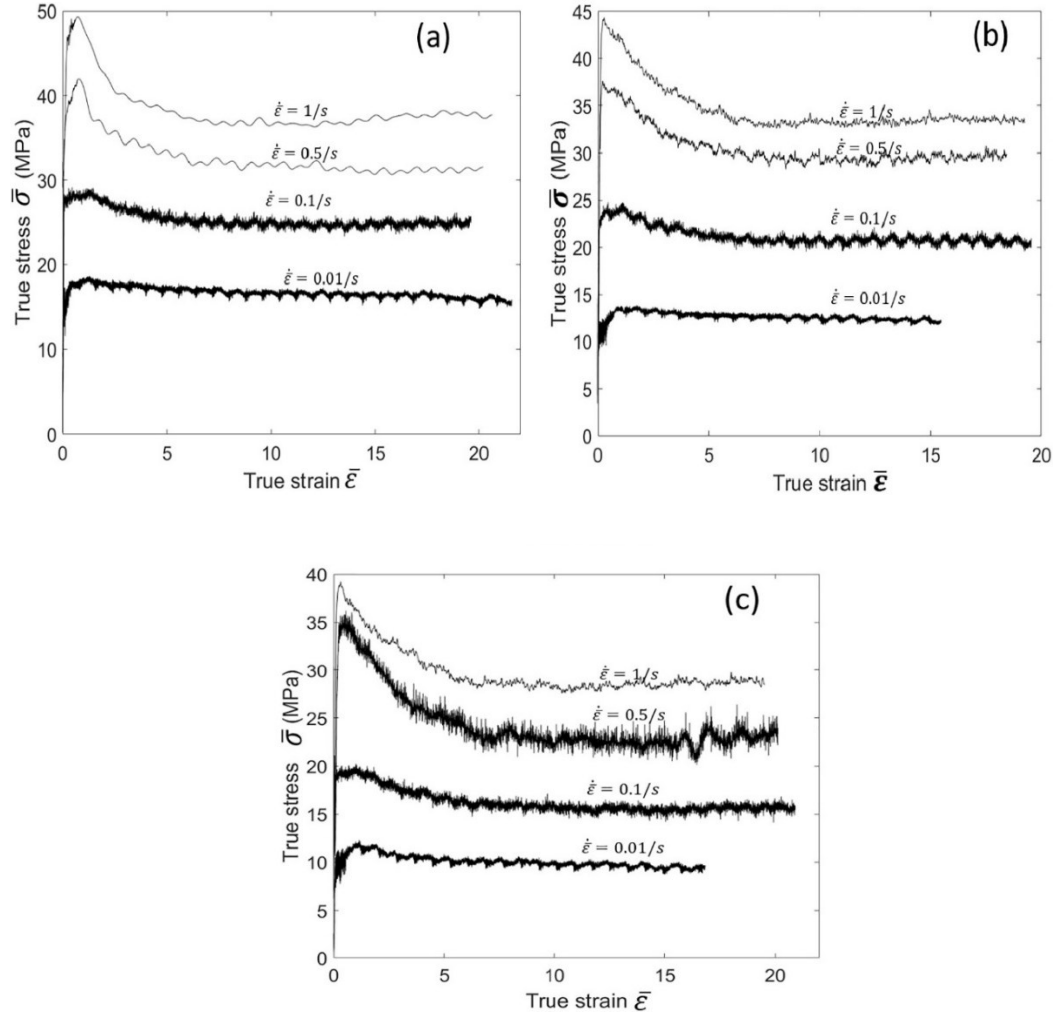


Figure 2.21: Flow curves obtained at 1000 °C (a), 1050 °C (b), 1100 °C (c) at different strain rates [44].

2.13. Aluminum and Aluminum Alloys

Aluminum is one of the most versatile, economical, and attractive metallic materials for a wide range of uses ranging from soft, highly ductile wrapping foil to the most demanding engineering applications. Aluminum has a density of only 2.7 g/cm^3 , approximately one-third as much as steel (7.83 g/cm^3). Aluminum typically displays excellent electrical and thermal conductivity, but specific alloys have been developed with high degrees of electrical resistivity. These alloys are useful, for example, in high-torque electric motors. Aluminum is often selected for its electrical conductivity, which is nearly twice that of copper on an equivalent weight basis. The thermal conductivity of aluminum alloys, about 50 to 60% that of copper, is advantageous in heat exchangers, evaporators, electrically heated appliances and utensils, and automotive cylinder heads and radiators [5][48].

2.13.1. Alloy Categories

Aluminum alloys are classified in two types; wrought alloys and cast alloys. Each category has a nomenclature that is based on the primary mechanism of the property development. Based on phase solubilities many alloys respond to thermal treatment, like solution heat treatment, age hardening and quenching. Both casting and wrought alloys include heat treatable materials. The majority of the other wrought compositions rely instead on work hardening through mechanical reduction, usually in combination with various annealing procedures for property development[5].

These materials are referred as a work hardening alloys. Several cast alloys are essentially not heat treatable and used only in as cast or in thermally modified conditions unrelated to solution or precipitation effects [5]. In general, the families of aluminum alloys are represented by 1XXX, 2XXX, 3XXX up to 8XXX as shown in the Table 2.3.

Table 2.3: *Standard Terminology and Principle Alloy Element of Aluminum Alloy [5].*

Aluminum Alloy Designation	Principle Alloy Element
1XXX	99% pure
2XXX	Cu
3XXX	Mn
4XXX	Si
5XXX	Mg
6XXX	Mg and Si
7XXX	Zn
8XXX	Others

Casting alloys have a 3-digit number identifying the alloy group. Table 2.4. describes the general classifications of aluminum for cast alloys. The number after the decimal is referring to the casting process [5] [49]. These designations include:[5][50].

XXX.0 = casting;

XXX.1 = ingot used to make the casting;

XXX.2 = ingot used to make the casting (having typically tighter chemical limits than the XXX.1 ingot designation)

Table 2.4: *Aluminum Alloy Series Designation of Casting Alloys [5].*

Aluminium Series	Principle Alloy Element
100's	Aluminum 99%
200's	Copper
300's	Silicon+ copper and/or magnesium
400's	Silicon
500's	Magnesium
600's	Presently Unused, future alloys
700's	Zinc
800's	Tin
900's	Other

2.13.2. Wrought Alloy Classes

The general characteristics of the wrought alloy groups are described as;

1xxx Series.is a high purity alloy that contains 99% of aluminum, it has an excellent corrosion resistance and a high thermal conductivity, and is especially used in the electrical and chemical application[5].

2xxx Series. Alloying element is copper, with magnesium as a secondary addition. The alloy requires a solution heat treatment followed by ageing to gain an optimum property. Fig. 2.22[5] shows the relationships between some of the more commonly used alloys in the 2xxx series[5].

3xxx Series. Major alloying element is manganese, with an increase of 20% in strength compared with 1xxx series. They are mainly used for a moderate strength application[5].

4xxx Series. Silicon is the major alloying element, they have a low thermal expansion coefficient with high wear resistance; thus these alloys are well suited to production of forged engine pistons [5] [48][49].

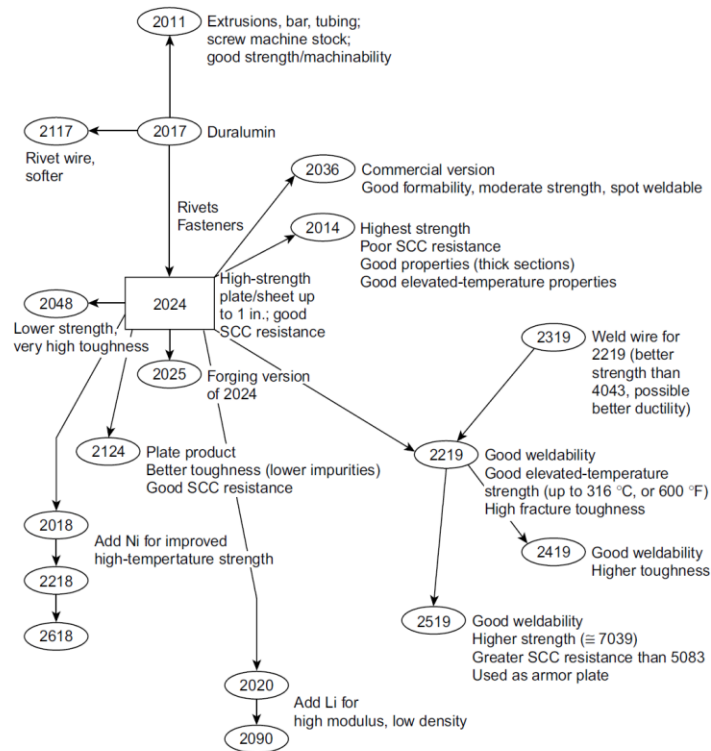


Figure 2.22: Relationships among commonly used alloys in the 2xxx series (Al-Cu)[5].

5xxx Series. Magnesium is used as a major alloying element or with manganese. The alloys have a moderate to high strength, good weldability and corrosion resistance[5][51].

Fig. 2.23. shows the relationships between some of the more commonly used alloys in the 5xxx series [5][48].

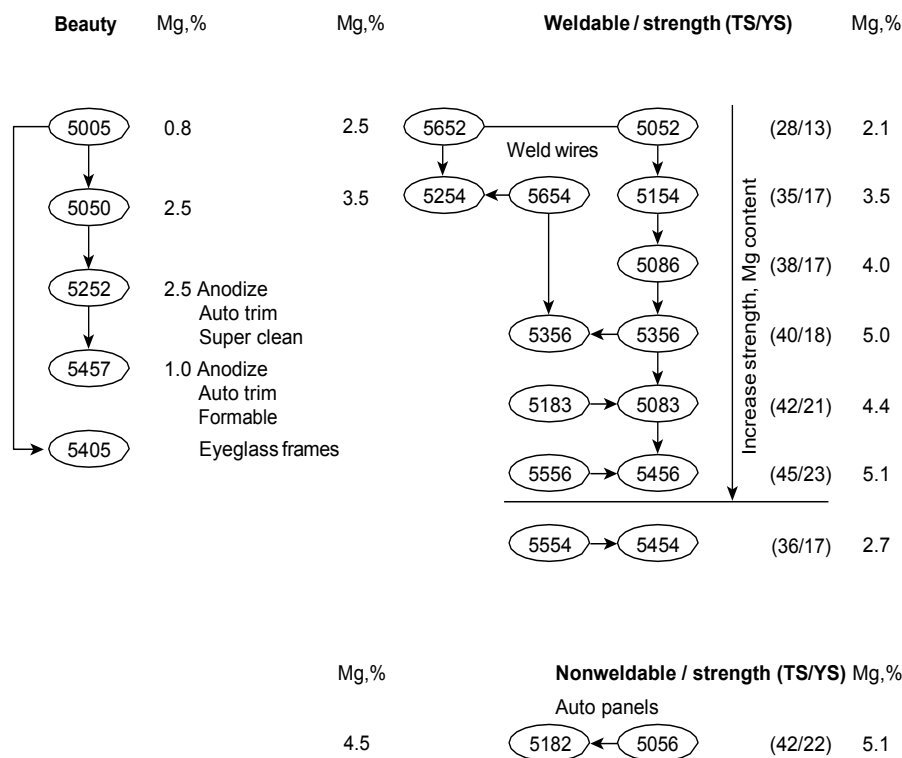


Figure 2.23: Relationships among commonly used alloys in the 5xxx series (Al-Mg). Tensile strength (TS) and yield strength (YS) are in ksi unit[5].

6xxx Series. Alloying elements are silicon and magnesium approximately in the proportions required for formation of magnesium silicide (Mg₂Si), that make them heat treatable. These alloys have a good weldability,

formability and corrosion resistance and are heat treatable[52]. The alloy may be formed in the T4 temper and strengthened after forming to full T6 properties by precipitation heat treatment. Fig. 2.24[5] Show the relationships among commonly used alloys in the 6xxx series (Al-Mg-Si)[5][48].

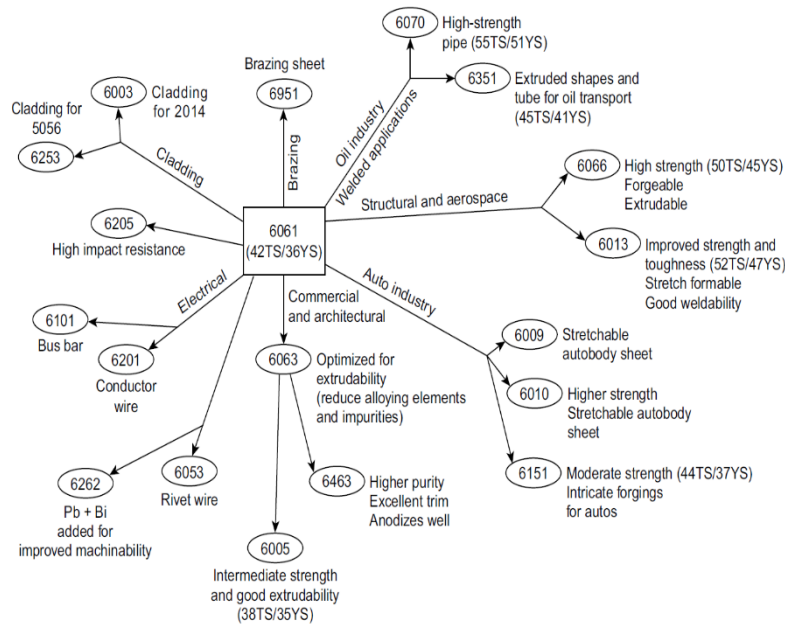


Figure 2.24: Relationships among commonly used alloys in the 6xxx series (Al-Mg-Si). Tensile strength (TS) and yield strength (YS) are in ksi units[5].

7xxx Series. Zinc is the major alloying elements with amounts of 1 to 8%, other elements like copper and chromium are added in a small quantity. The alloys can be used in the airframe structure, but exhibit a reduced resistance to stress corrosion cracking[53].

Fig. 2.25 shows the relationships between some of the more commonly used alloys in the 7xxx series [5][48].

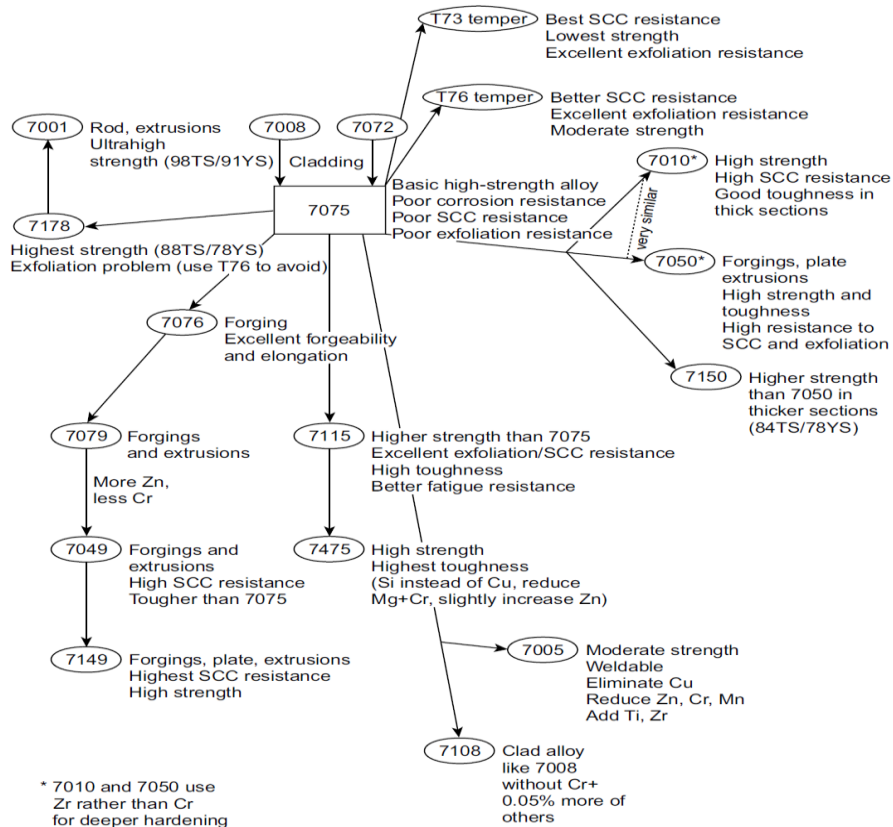


Figure 2.25: Relationships among commonly used alloys in the 7xxx series (Al-Zn-Cu-Mg-Cr). Tensile strength (TS) and yield strength (YS) are in ksi units[5].

2.14. Hot deformation and creep of Aluminum alloys

Many researches have been performed on the aluminum alloys, especially on 6xxx and 2xxx. An example are the Al–Si–Mg alloys, that are widely applied in automotive and aerospace industries due to their excellent weldability, desirable wear resistance, and corrosion resistance. The constitutive model is found to be an effective method to describe the change in mechanical response during hot deformation [12]. An accurate constitutive model can be embedded into the commercial FEM software for numerical simulation and analyzing the hot forming process. Thus, lots of constitutive models have been established to characterize the high-temperature flow behaviors of alloys in recent years. These approaches mainly include the above mentioned physically-based models [54][55], phenomenological models[56], and artificial neural networks [57][58].

2.15. Conclusions

This brief literature review has outlined the fundamentals behind the proposed work, describing the metallurgical background of IN 718 Superalloy, titanium (Ti-6Al-4V.) and aluminum. A study of the high temperature deformation behavior of the alloys mentioned above was performed by using different techniques under a wide range of temperature (T) and strain rate ($\dot{\epsilon}$). The study will present 3 case-studies of the hot deformation of complex alloy, investigated by increasingly complex approaches.

In particular, the first part of the study deals with a material (a Ti alloy) deformed in a single-phase field. In this case, the traditional approach based on phenomenological equations was used, purposely modified to describe the whole shape of the flow curves.

The second part will deal with another alloy (a Ni-base superalloy) tested in the single-phase field, but described by using a recently developed basic model, which took into account dislocation theory. The complexity of the model required that, at least in a first instance, the microstructure was as simple as possible.

The third and last part deals with the study of the creep response of a friction stir welded 2024 alloy. In this case the microstructure was extremely complex, so a number of different mechanisms, such as Hall-Petch strengthening, solid solution hardening and particle strengthening had in principle to be taken into account. Nevertheless, the basic model already used for the Ni-base superalloy was successfully used to describe the experiments.

Chapter 3.

Constitutive Modeling On β Transus of Ti-6Al-4V Alloy at High Temperature and Strain Rates

This chapter will describe the hot deformation behavior of Ti-6Al-4V alloy by a hot compression test in β phase in a wide range of temperature and strain rate range from 1010 °C - 1150 °C and 0.001 s⁻¹ – 100 s⁻¹ respectively. The effects of the hot deformation parameters (deformation temperature and strain rate) on the flow stress will be analyzed by a phenomenological model. The influence of strain in the constitutive equation of Ti-6Al-4V alloy (β phase) will be included in a modified formulation of the Hensel and Spittel equation. The peak flow stress dependence on temperature and strain rate will be described by the classic phenomenological approach, based on Garofalo and Arrhenius equations.

3.1. Introduction

For the Ti-6Al-4V alloy the β transus temperature is close to 1000 °C [59]. Hot compression tests in the dual-phase domain usually exhibit different results from tests in the β phase domain [60]. Different methods[61][62][63][64] have been proposed by researchers to evaluate a model for metal plasticity. Phenomenological models have relatively simple forms compared with the physic based models, and for this reason have been widely used to describe the deformation behaviors of different,

metallic materials[13][65] [66][67]. In recent years, researchers studied the hot-deformation mechanisms of β Ti-alloys with β -structure to analyse the deformation process and the microstructural evolution. For example, Zhao et al. [68]. investigated the deformation behaviour and mechanisms during hot compression at supertransus temperatures in Ti-10V-2Fe-3Al in the temperature range of 820–900 °C. Chen et al.[69] studied the high-temperature deformation behaviors of Ti–2Al–9.2Mo–2Fe alloy with boron alloy. They analyzed the microstructure evolution and softening mechanisms during the hot deformation, and found that dynamic recrystallization (DRX), is the dominant restoration mechanism at low strain rates, while dynamic recovery (DRV) dominates at high strain rates (10 s^{-1}) and low temperatures. Based on the previous works[46] [65][70], in this chapter we find a suitable constitutive equation to-model and study the hot deformation behaviour of Ti-6Al-4V over wide ranges of deformation temperature and strain rate in the β -state.

3.2. Compression test

The compression test is the most commonly used method for measure the flow curve of bulk material. In this test, a cylinder specimen is subjected to a compressive load, between two parallel dies with a constant strain rate. Obviously, the height and the diameter of the specimen change during the experiment, and these changes are calculated. So, when a cylinder specimen with a diameter D_0 and initial height h_0 is compressed to height h and spread out to diameter D according to the law of constancy of volume[71].

$$\pi \frac{D_0^2}{4} h_0 = \pi \frac{D^2}{4} h \rightarrow D_0^2 h_0 = D^2 h \quad (3.1)$$

The flow stress, σ is:

$$\sigma = \frac{F}{A} = \frac{4F}{\pi D^2} = \frac{4Fh}{\pi D_0^2 h_0} \quad (3.2)$$

and

$$\varepsilon = \ln \left(\frac{h_0}{h} \right) \quad (3.3)$$

where ε is the true compressive strain. These equations are used to obtain the flow curve. The main advantage of the compression test is that no necking occurs, in contrast with the tension test, so relatively large strain can be achieved. The disadvantage in this test is the friction between the specimen and the dies, which cause an effect called barreling. The equations described above are valid if there is a condition of uniaxiality, with friction neglected. The barreling establishes a triaxial state of stress tensor, because of interaction of the friction forces. This happens since the expansion of cross section in the center of specimen is greater than at the surface, see Fig. 3.1. The less deformed zone at the contact surface lead to the accumulation of stress and loss of uniaxial deformation.

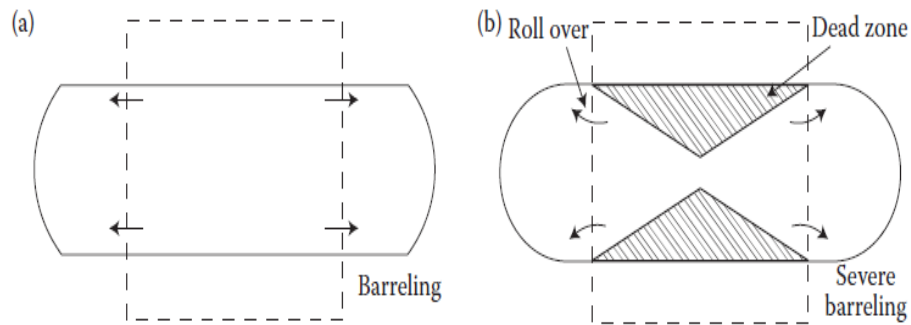


Figure 3.1: (a) slight barreling as a result of light friction which hinders sliding and (b) severe barreling as a result of high friction which prevents slipping[48].

3.3. Experimental Procedure

The chemical composition of the investigated alloy is given in Table 3.1. The β - transus for this material is close to 1010 °C. Compression specimens of Ti-6Al-4V (Fig 3.2.) were machined with 24.6 mm height and 15.96 mm diameter. The samples were heat treated before the deformation at 1100°C for 30 min to obtain a single-phase microstructure. The isothermal compression tests were carried out in the temperatures range of 1010, 1050, 1100 and 1150 °C under strain rates of 100, 50, 10, 1, 0.1 and 0.001 s⁻¹. The temperature was measured by thermocouple. After deformation, the specimens were quenched in water. The experiments were carried out in the Institute of Materials science, Thermomechanical Modelling Group, TuGraz, Austria.



Figure 3.2: Double cone specimens before and after the compression test for (Ti64).

Table 3.1: Chemical composition of the Ti6Al4V used in this study (in wt.%)

<i>Al</i>	<i>V</i>	<i>Fe</i>	<i>C</i>	<i>H</i>	<i>O</i>	<i>Ti</i>
6.33	4.00	0.20	0.03	0.004	0.17	<i>Balance</i>

3.4. Experimental results for Ti – 6Al – 4V

3.4.1. Peak flow stress dependence on strain rate and temperature.

Although different forms of constitutive equations can be used, the most accurate description is in fact obtained by the Garofalo equation. Fig. 3.3. shows the true-stress strain curve of Ti-6Al-4V alloy under different deformation conditions.

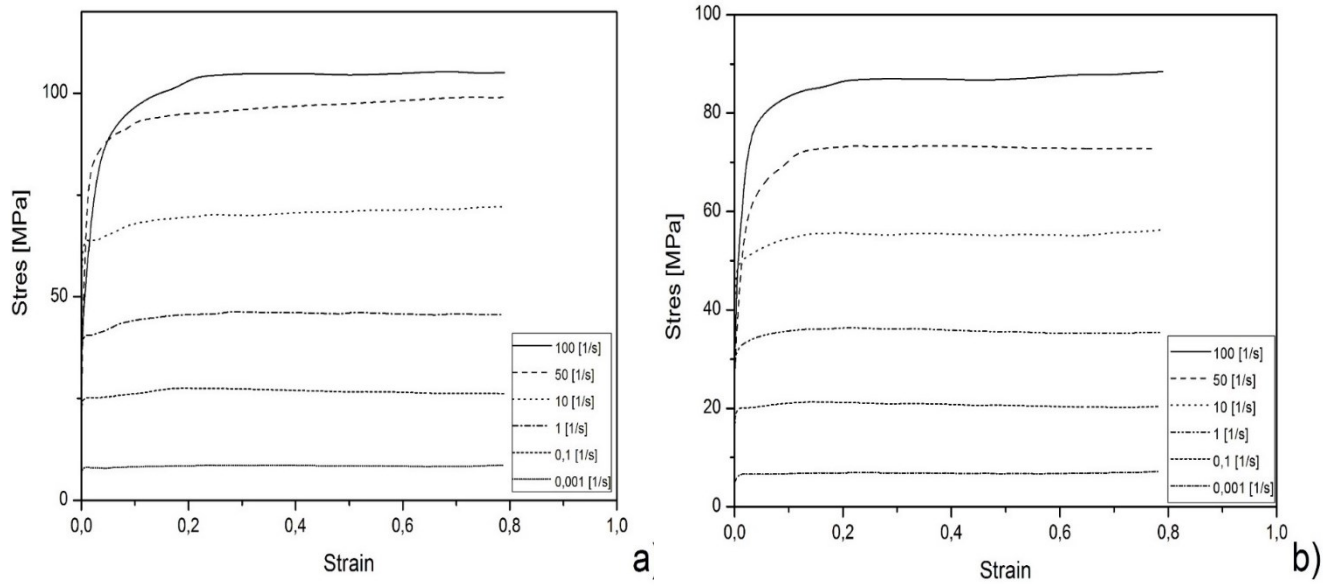


Figure 3.3: Representative stress-strain high temperature flow curves of the Ti – 6Al – 4V alloy under different compression deformation conditions: (a) 1050°C; (b) 1150°C.

Phenomenological constitutive equations were used to describe the relationship between the flow stress, strain rate and temperature. Arrhenius type equation is an accurate approach to describe the relationships between the flow stress, strain rate and deformation temperature. The strain rate values as a function of the peak flow stress shown in Fig. 3.4, described by Equation 2.5 (Chapter 2). A good parallelism of the isothermal curves is obtained with $\alpha = 0.0154 \text{ MPa}^{-1}$, which will be used in the following. The stress exponent n ranged from 3.9 to 4.2.

The activation energy is an important physical parameter and it can be determined by considering the average slope of $\ln[\sinh]$ vs. $(1/T)$, as shown in Fig.3.5. At strain of 0.79, Q_{HW} was 202 kJ/mol. This value is intermediate between the activation energy for self-diffusion in pure Ti (131 kJ/mol), and that observed in a similar alloy tested in β -field (270 kJ/mol)[72].

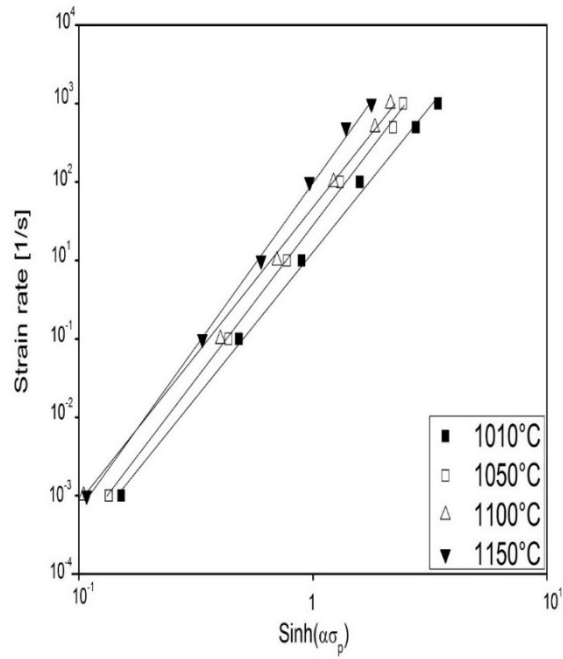


Figure 3.4: Strain rate dependence on the peak flow stress with $\alpha = 0.0154 \text{ MPa}^{-1}$.

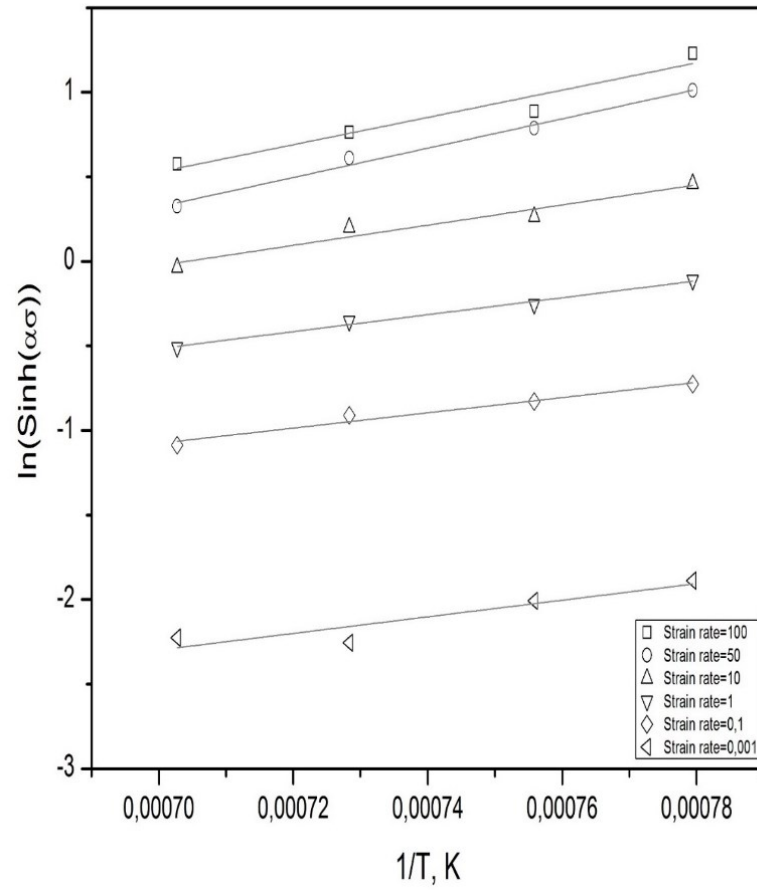


Figure 3.5: Plot used to calculate the activation energy, $\ln [\sinh (\alpha \sigma)]$ vs $1/T$.

The Zener-Hollomon parameter can be determined by Equation 2.2 (described in Chapter 2), showed in (Fig. 3.6). All the peak flow stress values align on the same straight line of slope close to 4, as expected.

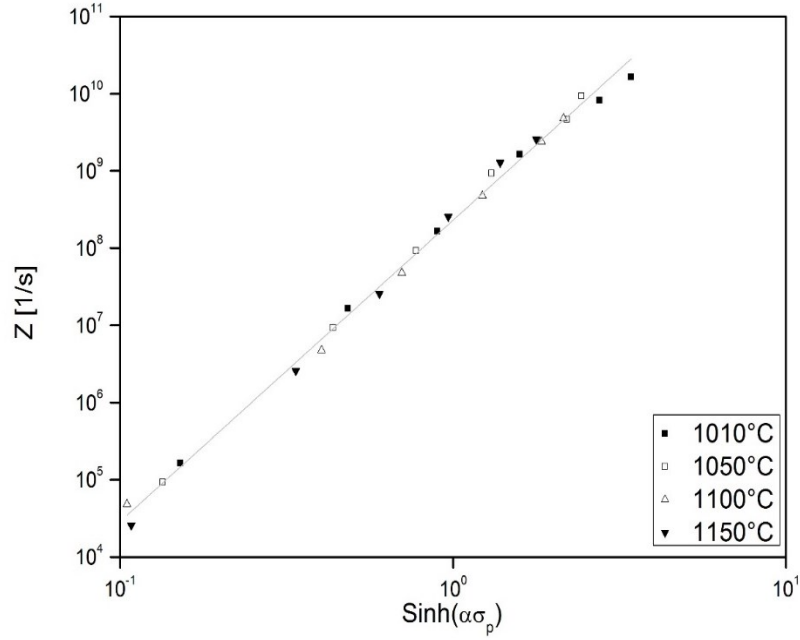


Figure 3.6: The relationships between the peak stress and the Zener-Hollomon parameter for the calculated peaks; compression test.

3.4.2. Flow stress variation with strain, strain rate and temperature

The combination of high-temperature testing and of a different computational approach was recently used to model the high-temperature response of the AA6082 alloy[73]. The constitutive model was based on an equation developed by Hensel and Spittel[74], in the form, Eq.3.4.

$$\frac{\sigma}{MPa} = B \exp\left(\frac{m_1 T}{K}\right) \varepsilon^{m_2} \left(\frac{\dot{\varepsilon}}{s^{-1}}\right)^{m_3} \exp\left(\frac{m_4}{\varepsilon}\right) (1 + \varepsilon)^{m_5 T} \exp(m_7 \varepsilon) \left(\frac{\dot{\varepsilon}}{s^{-1}}\right)^{m_8 T} \left(\frac{T}{K}\right)^{m_9} \quad (3.4)$$

where B , m_1 , m_2 , m_3 , m_4 , m_5 , m_7 , m_8 and m_9 are material parameters. The stress, the strain rate and the absolute temperature are normalized by the respective units (MPa, s^{-1} and K) to make B a dimensionless constant. Since the differentiation at constant strain of Eqn.3.4, gives a temperature-dependent but constant slope of the isothermal curve in double logarithmic coordinates, this equation leads to a power-law dependence of strain rate on applied stress, with a stress exponent $n = 1/(m_3 + m_8 T)$. By contrast, in the hot-working regime, the strain rate sensitivity of the flow stress decreases with increasing strain rate. Thus, a new constitutive model[75] was developed by replacing σ with $\sinh(\alpha\sigma)$, i.e.

$$\sinh(\alpha\sigma) = A \exp\left(\frac{m_1 T}{K}\right) \varepsilon^{m_2} \left(\frac{\dot{\varepsilon}}{s^{-1}}\right)^{m_3} \exp\left(\frac{m_4}{\varepsilon}\right) (1 + \varepsilon)^{m_5 T} \exp(m_7 \varepsilon) \quad (3.5)$$

The m_8 parameter has been omitted, since it was assumed that at a given strain the stress exponent n should be temperature independent, i.e. $m_8=0$. In addition, the m_9 parameter was also neglected in order to obtain a simpler formulation. Figures 3.7-3.10, plots the model curves obtained by the model equation 3.5, after the different parameters were calculated by a regression procedure. The correlation between the experimental data and the model curves is indeed very good, a major deviation being observed in the early stage of deformation under low strain rates. In this regime, the model tends to underestimate the work hardening response of the alloy, indicating a possible difference in the deformation mechanisms.

Notwithstanding the observed deviations in the low strain regime, the accuracy of the model in describing the material response is still more than satisfactory, in particular when one considers that the proposed equation is very easy to handle.

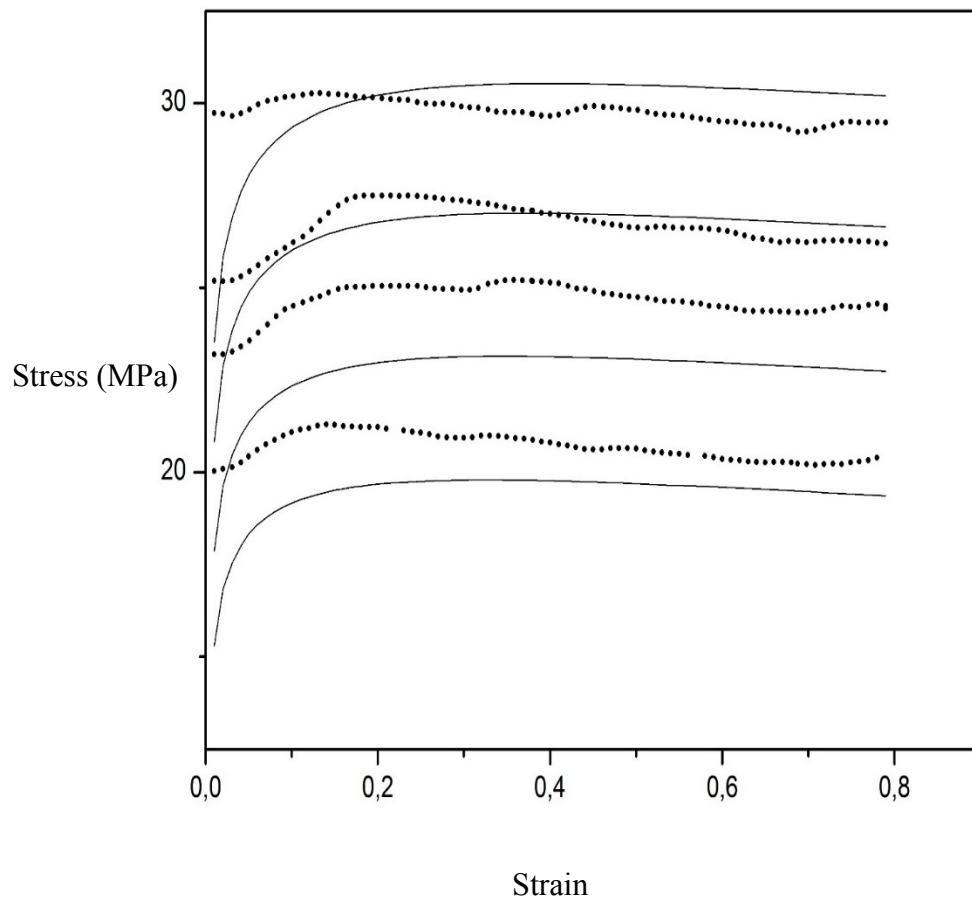


Figure 3.7: Comparison between the modelled flow curves and experimental data at 0.1 s^{-1} .

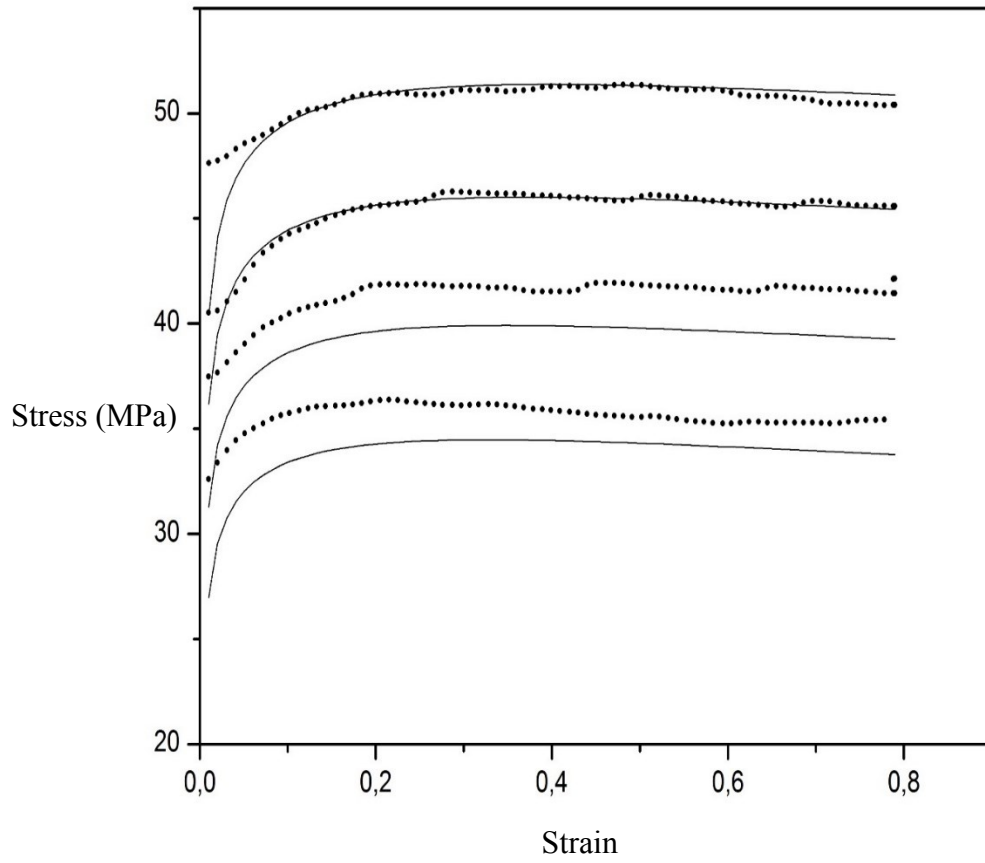


Figure 3.8: Comparison between the modelled flow curves and experimental data at 1 s^{-1} .

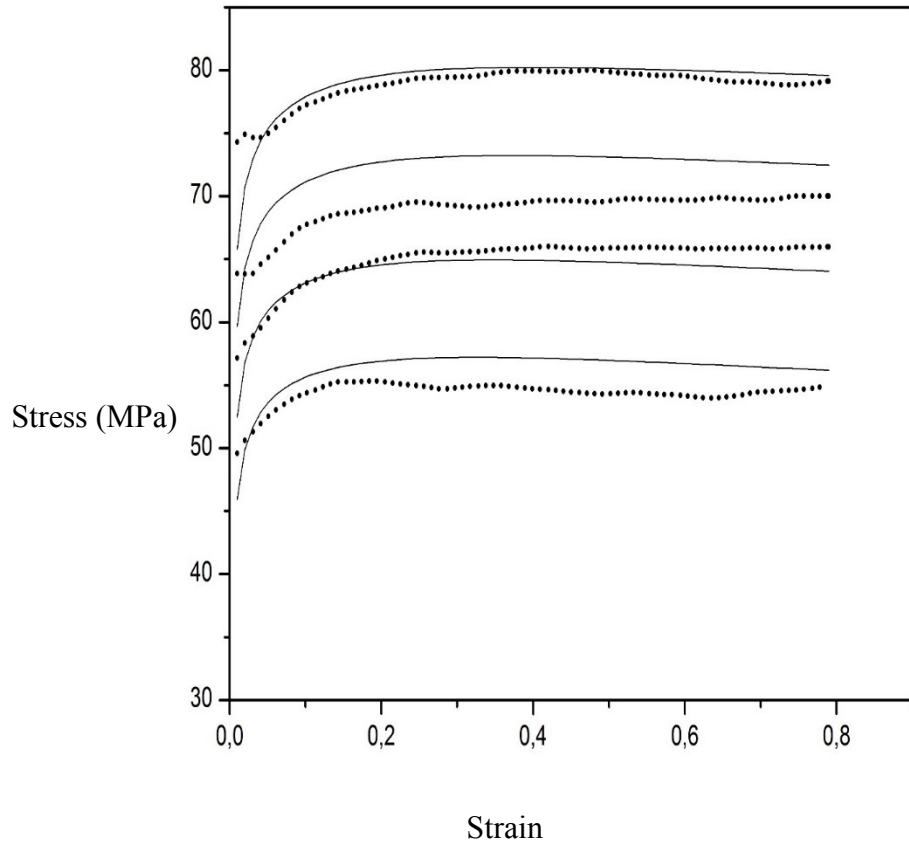


Figure 3.9: Comparison between the modelled flow curves and experimental data at 10 s^{-1} .

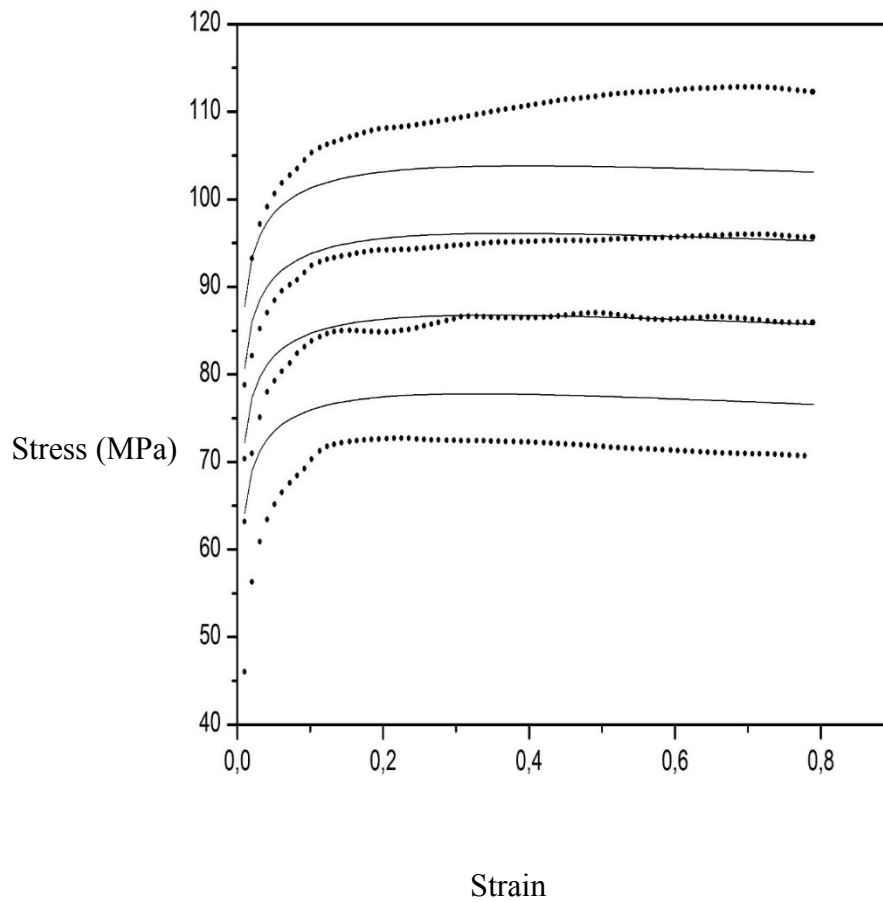


Figure 3.10: Comparison between the modelled flow curves and experimental data at 50 s^{-1} .

Although the study of hot deformation of a single-phase alloy, such as the Ti-6Al-4V above β -transus, should be a quite simple affair, the available evidences attest quite the contrary.

Values of the activation energy for hot-deformation ranging from 172 kJ/mol [76] up to 376 kJ/mol [59] have been indeed observed. At high temperature (1050°C), in particular, after straining in compression up to $\varepsilon = 0.8$, the alloy microstructure was still largely un recrystallized after testing at 10 s^{-1} , while under lower strain rates (0.001 s^{-1}) only a limited fraction of fine DRX grains were observed[77]. These results support the picture presented in [76], where DRX, for strains below 0.6 at 1100°C, is considered to be significant only for strain rates lower than 0.1 s^{-1} , and with the evidences presented in[78] , where recrystallization kinetics were described at 1000-1100°C, under a very low strain rate (0.001 s^{-1}). In the last study, on the other hand, the calculated volume fraction of recrystallized material approached 100% only for strain above 5.0 (1100°C), 7.5 (1050°C) and 10 (1000°C), i.e. well above the maximum strain achievable by a compression test. Testing in torsion permits to attain much larger deformations, and only in this case the flow softening which accompanies DRX will be observed[44]. In the present study, the model provides flow curves that are typical of materials in which deformation is controlled by recovery; thus, a strain hardening stage is followed by a “steady state”. This is actually the behavior one should observe in the high strain rate regime, where DRX has minor effects since it will become dominant only for much larger strains. The observed “steady state” should be actually more properly considered the “peak region” which precedes the flow softening associated to extensive, occurrence of DRX. The scatter in the values of the activation energy could be in part rationalized by accounting for the different experimental envelopes considered-

in the various studies. The value of 172 kJ/mol was obtained in [59] by considering only the data at 0.01 s^{-1} and $1000\text{-}1100^\circ\text{C}$, while 376 kJ/mol were calculated for tests carried out- between 1025 and 1075°C , under strain rates ranging from 0.001 to 1 s^{-1} , i.e. in a much wider regime, where DRX was operative on in a limited range of conditions.

3.5. Summary and Conclusions

In this chapter, the high-temperature deformation behavior of the Ti-6Al-4V was investigated by hot compression tests in β phase domain, within temperature range of from 1010°C - 1150°C and strain rates from 0.001 s^{-1} - 100 s^{-1} . Based on the experimental data, a constitutive model was developed to describe the high-temperature deformation behavior of the studied titanium alloy. As usual, the flow stress of Ti-6Al-4V increased with the strain rate and decreased with increasing deformation temperature. The influence of strain in the constitutive equation of Ti-6Al-4V alloy (β - phase) was incorporated in a modified formulation of the Hensel and Spittel equation. The peak-flow stress dependence on temperature and strain rate was described using the classic phenomenological approach, based on Garofalo and Arrhenius equations, obtaining an activation energy high-temperature deformation of 202 kJ mol^{-1} . The analysis of the Ti-6Al-4V here presented, provides an excellent tool for the prediction of the working loads during hot working of the alloy, but, due to its phenomenological nature, does not permit a generalization. Thus, the excellent results cannot be extended to similar materials. This obvious drawback requires the use of basic models, which will be dealt in the next chapters.

Chapter 4.

A model for the Hot Workability of Solution Treated *IN718* Superalloy

The work present in this chapter discusses the hot workability of *IN718* superalloy investigated by a hot torsion tests over a wide range of strain rate and temperature. Although the classical phenomenological approach, based on Garofalo and Arrhenius equations was used to describe the hot deformation behavior, an alternative physically-based approach was also applied. The model considered dislocation hardening and solid solution strengthening.

4.1. Torsion test

The torsion test has been used for about 50 years as a means of hot workability assessment in metals and alloys Fig. (4.1) [71]. For this method the specimen is mounted between the two heads of a testing machine and twisted Fig.(4.2).

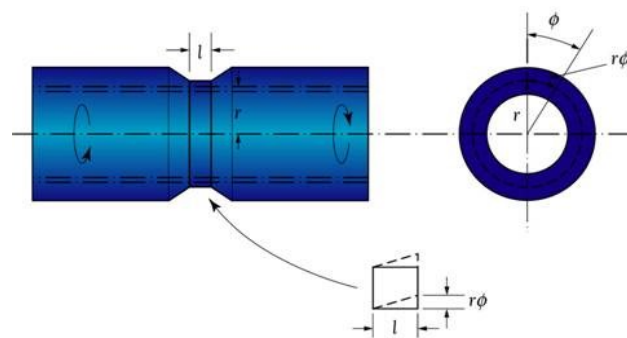


Figure 4.1: typical torsion-test specimen[71].

The main advantage of the torsion test is the fact that it is possible to reach very large strain and investigate the plastic behavior without friction or necking. Furthermore, the specimen does not present significant changes in shape during deformation as long as the gage section is restrained to a fixed length[71]. The disadvantage of the torsion test is the fact that it is characterized by non-uniform distribution of deformation over the length and cross-section of specimen, in fact the stress and strain are 0 at the center and maximum at the surface of the specimen. Hence the deformation in the torsion is not an accurate simulation of metalworking processes, because of excessive material reorientation at large strain[79]. The output of the torsion test is represented by torque versus twist angle, that must be converted into the stress and strain (determination of flow curve). For this purpose, there are several methods, such as Nadai's graphical method, Field and Backofen method etc. The problem of these methods is characterized by the fact that, for the conversion they use analytical equations that reproduce homogeneous deformation; this is in contrast with the nature of the torsion test that is an inhomogeneous process[80].

4.2. Test device

The torsion test is widely used as compression and tension test, Individual researcher, designed the apparatus for specific experiments, and most of these machines are designed to provide a range of constant twist rate only. In general, the torsion machines have: test frame, drive system, twist and torque monitoring device and a furnace[71][48]. The two major types of test frame are horizontal and vertical frame.

The test machine used for the experimental part of this thesis is an electrohydraulic machine, (Fig 4.2). In the torsion test the specimen is twisted around its axis without bending, therefore the test frame should have high rigidity and an accurate alignment. The drive system is the set of a twist head, a weight head and a motor. The twist and torque sensor (monitor system) record the twist of specimen and torque of the motor. The operation of the machine is controlled by a computer, which also records all the data and can print out stress–strain curves.

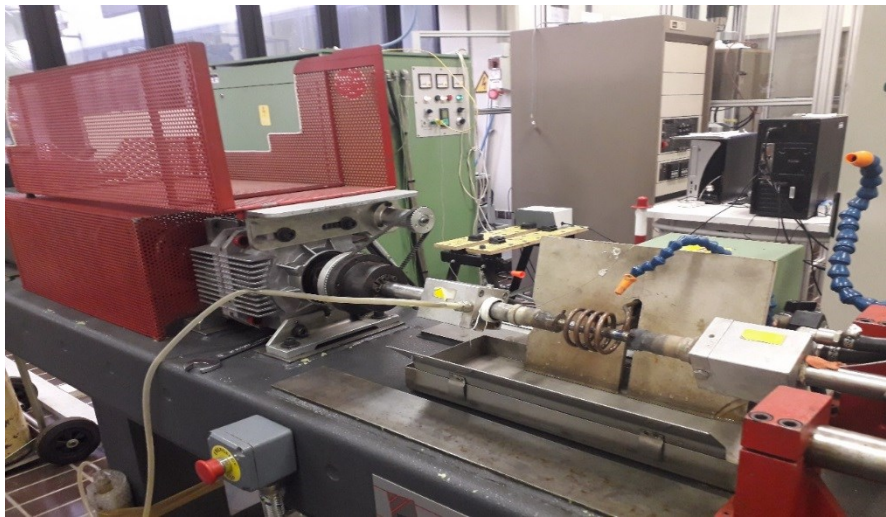


Figure 4.2: *Servo controlled, hydraulic torsion test machine.*

For investigating the workability at elevated temperatures using torsion tests, a heating system is necessary. The two most common methods of heating are furnace and induction [71].

4.3. Evaluation methods

In order to analyze and therefore predict the constitutive equation that represents the flow behavior of material, the raw data must be converted into flow curves. There are different methods for converting this raw data (torque-twist) to the shear stress-shear strain curve. In any case a cylinder solid bar is considered with length L and the radius R . The torque M is applied at one end of this bar which introduces the shear stress τ and shear strain γ ; Fig 4.3.

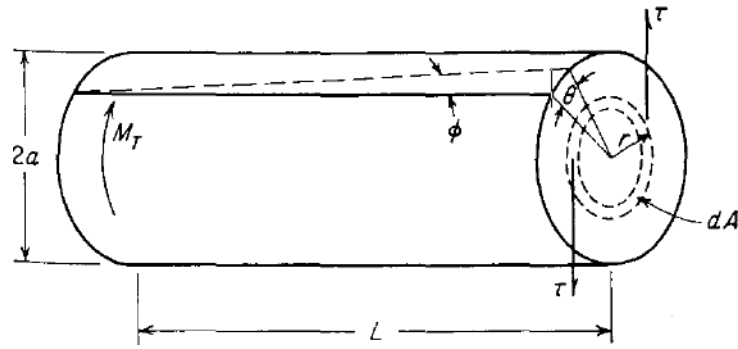


Figure 4.3. Torsion of solid bar specimen[80].

In according to the Hooke's law, the relationship between shear stress and shear strain can be expressed as:

$$\tau = G\gamma \quad (4.1)$$

Where the shear strain is:

$$\gamma = \frac{r\theta}{L} \quad (4.2)$$

Herein, θ is the twisted angle (in radians), r is the radial position and L the length of gauge. When the specimen is twisted, the component of torque, dM in area dA is given by:

$$dM = \tau r dA \quad (4.3)$$

Instead the total torque applied to the specimen is:

$$M = \int_m dm = \int_A \tau r dA = 2\pi \int_0^R \tau r^2 dr \quad (4.4)$$

The resistance to torsion is represented by the polar moment (I) of area (A), and can be expressed as:

$$I = \int_A r^2 dA \quad (4.5)$$

Combining Eq 3.3 and Eq 3.4, the shear stress is:

$$\tau = \frac{Mr}{I} \quad (4.6)$$

For a solid bar specimen, being that the polar moment is $I = \pi r^4/2$, the maximum shear stress is:

$$\tau_{max} = \frac{2M}{\pi R^3} \quad (4.7)$$

The maximum shear stress for a tubular specimen, instead, is:

$$\tau_{max} = \frac{2M}{\pi(a_1^3 - a_2^3)} \quad (4.8)$$

where a_1 is the outside radius of tube and a_2 the inside radius. In tubular specimen, the shear stress gradient can be neglected since the wall is very thin. The effective stress, σ , and effective strain ε are converted by means of the von Mises yielding criterion[81].

$$\sigma = \sqrt{3}\tau \quad (4.9)$$

$$\varepsilon = \frac{\gamma}{\sqrt{3}} \quad (4.10)$$

4.4. Experimental results for IN 718

Experimental testing was performed for the age-hardenable Ni-Cr-Fe-Mo-Al-Ti wrought superalloy (53% Ni, 18.3% Cr, 18% Fe, 2.97% Mo & 0.59% Al). This kind of material are extensively used in the aerospace industry due to their high corrosion and oxidation resistance, high strength and long creep life at elevated temperatures. Inconel 718 possesses remarkable machinability and welding ability, in comparison with other superalloys. These materials have a relatively high yield (700–1200 MPa) and tensile (900–1600 MPa) strength at room temperature. The most remarkable property of these materials is that they maintain their mechanical properties within a wide range of temperatures (up to- 600–800 °C). Therefore, these alloys are used in the hot section of jet engines[82][83]. In this work, the interest to study the mechanical behavior of Inconel 718 at high strain-rates and temperatures.

The specimen of Inconel 718 and the results of the torsion experimental tests are shown in Fig. 4.4., 4.5. Samples with a 10 mm diameter and a gauge length of 15 mm, were machined from the as received rod prior to the solution treatment (1100°C for 4 h) to obtain a single-phase microstructure. The true stress vs. true strain curves are reported in function of temperature (from 1050 °C up to 1100 °C) and strain-rate (from 0.01 up to 1 s⁻¹). Samples were heated by a high frequency induction coil at 1°C/s to the testing temperature and maintained at this temperature for 300 s. Subsequently the samples were strained up to a strain of 2.0 and quenched by a water jet. The torque M and the number of revolutions N were recorded and converted into von Mises equivalent stress σ and equivalent strain ε at surface by the simplified formulas:

$$\sigma = \frac{3\sqrt{3}M}{2\pi \cdot R^3} \quad (4.11)$$

$$\varepsilon = \frac{2 \cdot \pi \cdot N \cdot R}{\sqrt{3}L} \quad (4.12)$$

where R and L are respectively the radius and length of the gauge. All the tests were carried out up to an equivalent strain of 2.0, unless rupture occurred before this deformation was attained. The true stress-strain curves exhibited completely different shapes depending on the deformation temperature and strain rate. The deformation temperature and initial strain rate strongly affect the flow stress during hot deformation.

High deformation temperature is known to promote the nucleation and growth of dynamically recrystallized grains and dislocation annihilation, and thus reduces the stress level[65][84]. At the beginning of the deformation, the flow stress increases rapidly, due to work hardening caused by the rapid generation and multiplication of dislocation. With the increase of strain, the flow stress achieves a peak value, and then the flow stresses monotonically decrease due to the occurrence of dynamic recrystallization. The peak, thus usually associated with DRX, is well evident in the high-strain rate regime but becomes barely noticeable when the strain rate decreases. As expected, the material strength gradually decreases with increasing the temperature and the shape of the stress-strain curve dramatically changes at 1050 °C, where the material behaves like a perfectly plastic material. The strain at failure increases with strain-rate and temperature.

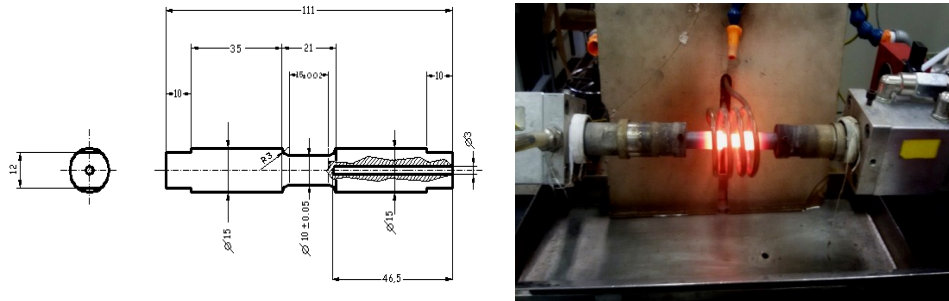


Figure 4.4: Specimen for torsion testing and experimental layout for torsion testing.

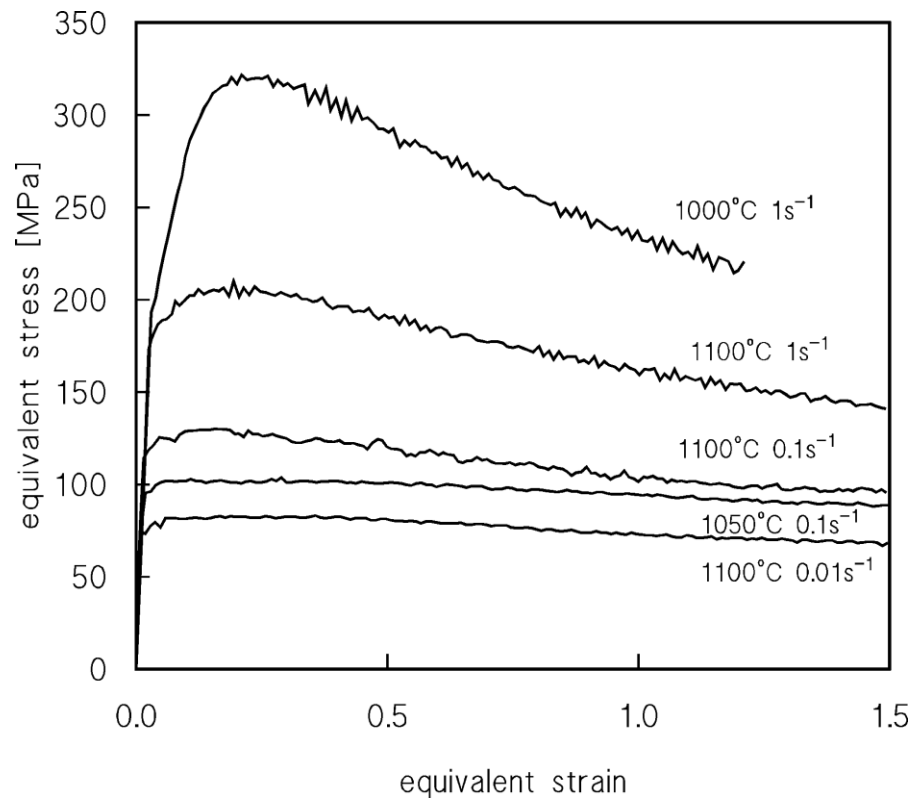


Figure 4.5: Representative flow equivalent-stress vs equivalent strain flow curves obtained by testing the IN718 in torsion.

The peak-flow stress variation with experimental strain-rate, is shown in Fig. 4.6. Peak stress usually corresponds, in materials that undergo DRX, to a condition in which a mere fraction, (roughly 30% at maximum) of the microstructure is recrystallized[85].

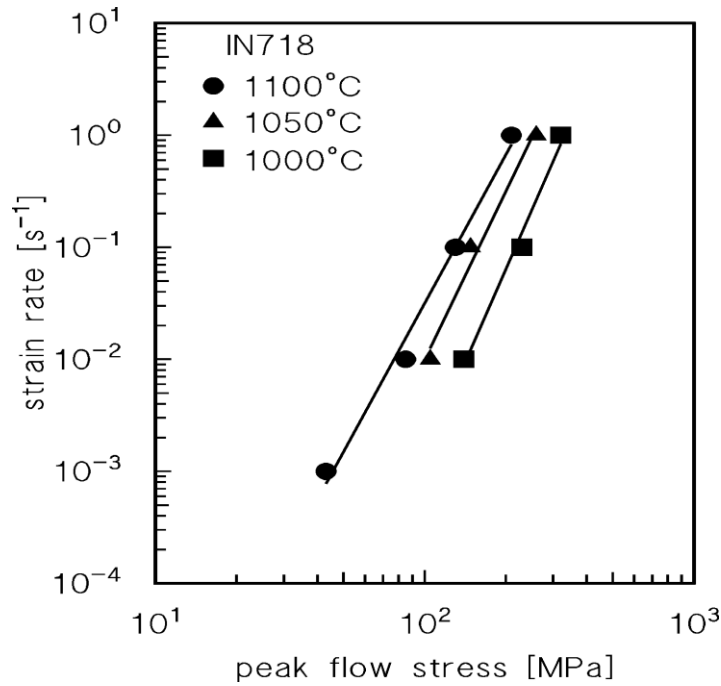


Figure 4.6: Peak flow stress in torsion as a function of the testing strain rate.

At steady-state, DRX is complete. In this sense, any model developed to describe high-temperature recovery-controlled deformation, where DRX does not occur, can be hardly applied to the steady state of a material that undergoes dynamic recrystallization. The situation is somewhat different if one considers the peak condition, since the peak stress (σ_p) is in most cases reasonably close to the “saturation stress” (σ_s^*). That is, to the steady-state stress the material would have, to reach in the absence of DRX. An estimate of the difference between the saturation and the peak stresses can be obtained by plotting, the strain-hardening rate ($\theta = \partial\sigma / \partial\varepsilon$) as a function of the flow stress.

The inflection in the curve indicates the start of DRX, i.e. the critical stress for the onset of recrystallization, while extrapolation at $\theta = 0$ of the linear part of the curve gives the saturation stress. The analysis of Fig. 4.7, which is representative of the behavior of IN718, suggests that the difference between σ_s^* and σ_p can be appreciated only under the high strain rates, but in any case, it is limited. (3% and 6% at $1150^\circ\text{C}\cdot 1\text{s}^{-1}$ and $1000^\circ\text{C}\cdot 1\text{s}^{-1}$ respectively).

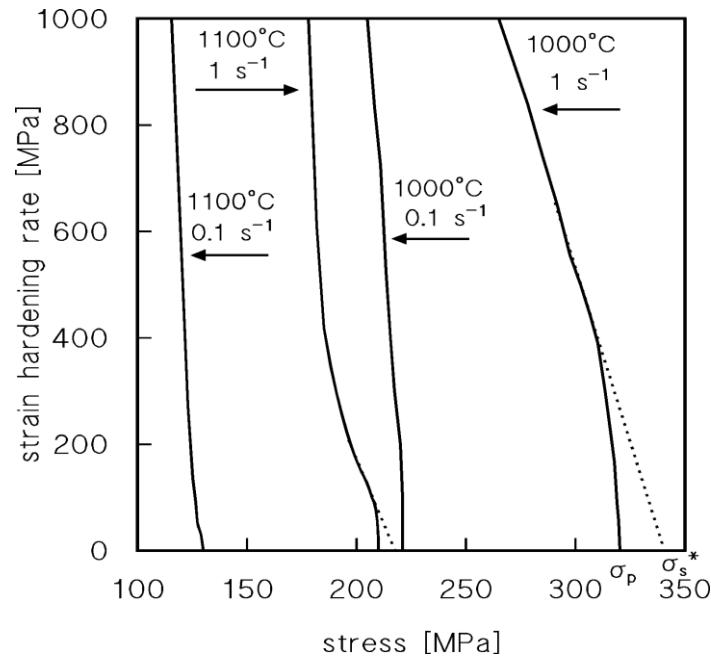


Figure 4.7: Strain-hardening rate ($\theta = \partial\sigma / \partial\epsilon$) as a function of flow stress for representative conditions. The Figure also plots the peak stress (σ_p) and the saturation stress (σ_s^*).

4.5. Effects of solid solution strengthening

A comparison between the peak flow stress in torsion obtained in this study on IN718, and the results in torsion and compression for pure Ni[61][86] is illustrated in Fig. 4.8. Although both pure Ni and the IN718 investigated in the present study were single-phase materials, the superalloy exhibited substantially higher values of the peak stress. In addition, the value of the activation energy was substantially higher in the superalloy (345 kJ mol^{-1} , to be compared with the value of 294 kJ mol^{-1} for the activation energy for self-diffusion in Ni). This behavior can be hardly rationalized by the phenomenological approach followed in the present study, which provides an excellent description of the data, but cannot be easily related to microstructural mechanisms. The increase of the peak flow stress and of the value of the activation energy for hot working, on the other hand, can be qualitatively explained as an effect of solid-solution strengthening, by introducing physical-based models such the one described in [87]. Solid solution hardening introduces a drag stress due to viscous motion of dislocations in solute atoms atmospheres, which can explain the higher Peak flow stress of the solution treated IN718. In addition, also the activation energy for hot deformation increases due to the presence of atoms in solid solution, since these atoms are forced to jump in and out the solute atmospheres as dislocations move[88].

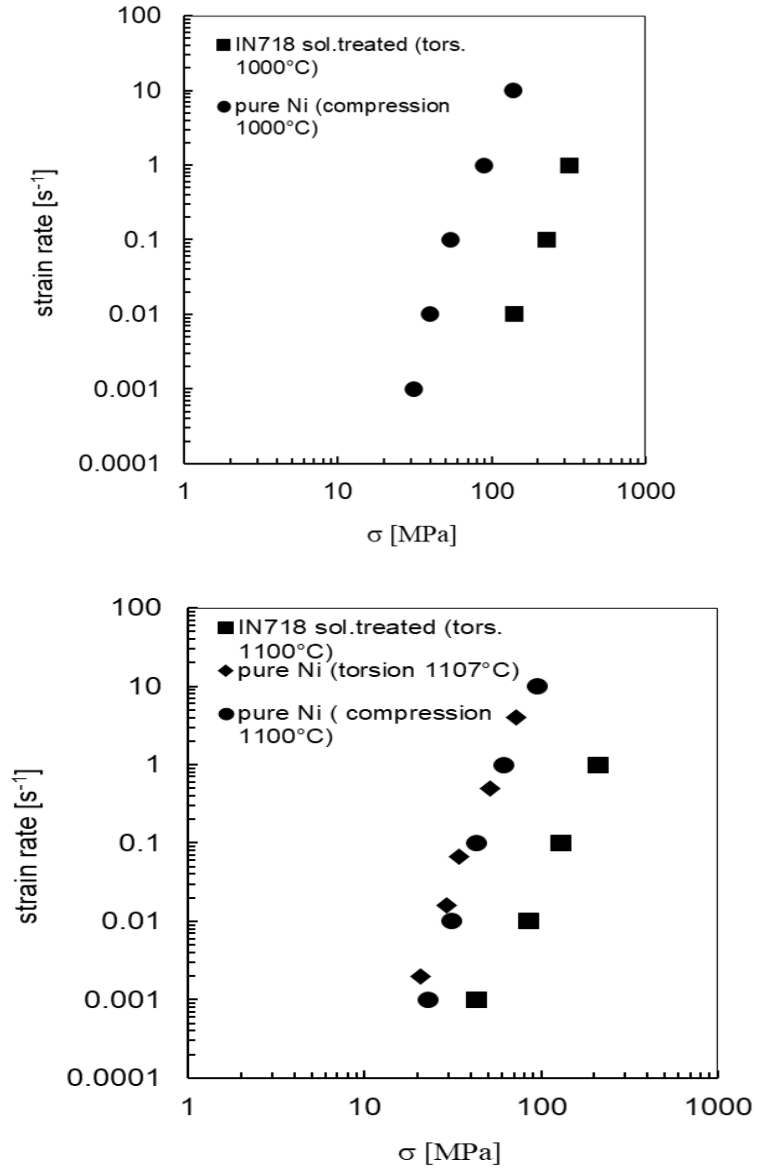


Figure 4.8: Comparison between the peak flow stress values obtained by testing in torsion single-phase IN718 (this study) and pure-Ni in torsion and compression at 1000 and 1100°C[61][86].

4.6. Material models

During the last decades several material models were proposed with the aim to reproduce the mechanical response of the materials varying the strain-rate and the temperature[89][90]. Among various phenomenological models, the combination of the Garofalo and Zener-Hollomon equations will be described for calculating the peak flow stress in the hot working regime[65] [61].

4.6.1. Constitutive analysis

The peak flow stress dependence on strain rate can be adequately expressed by the Zener-Hollomon parameter (Z), which is a function of temperature and stress:

$$Z = \dot{\epsilon} \exp \left(\frac{Q_{HT}}{RT} \right) = A [\sinh(\alpha \sigma)]^n \quad (4.13)$$

In this study, the strain rate as a function of $\sinh(\alpha \sigma_p)$, with $\alpha = 0.003$ is shown in Fig. 4.9, The experimental data align on almost parallel straight line of slope n close to 4.2, The activation energy for hot working was calculated ($Q_{HW} \approx 350 \text{ kJ mol}^{-1}$) by plotting $\sinh(\alpha \sigma_p)$ as a function of $1/T$ that shown in Fig 4.10, The Zener-Hollomon parameter as a function of $\sinh(\alpha \sigma_p)$ described in Fig. 4.11, since all the experimental data overlap on a single straight line of slope close to 4, so it can be found that the peak stress increases with the increase of the Z parameter, one can reasonably,

conclude that the constitutive model gives an excellent description of the experimental data.

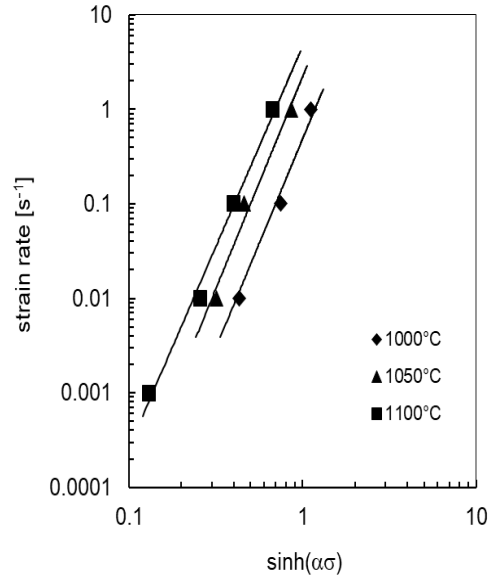


Figure 4.9: Strain rate as a function of $\sinh(\alpha\sigma_p)$, with $\alpha=0.003$.

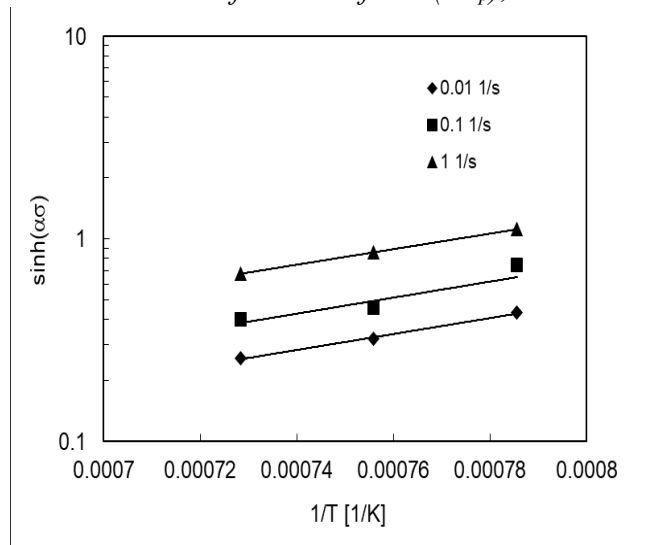


Figure 4.10: Calculation of the activation energy for hot working of single-phase IN718.

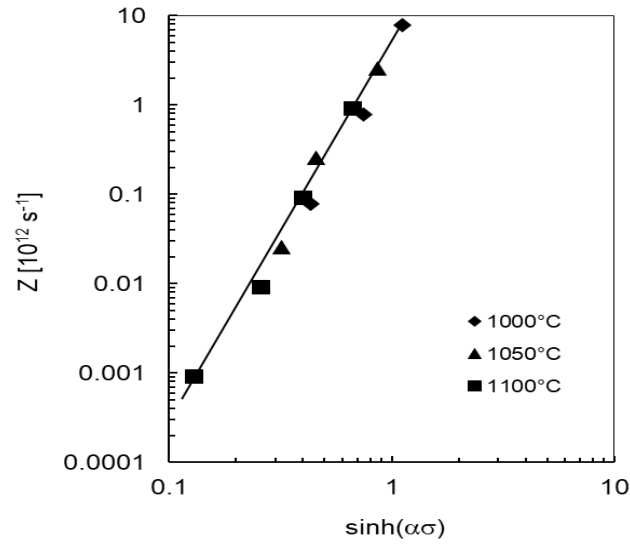


Figure 4.11: Zener-Hollomon parameter as a function of $\sinh(\alpha\sigma_p)$

4.7. Microstructure analysis

The microstructural evolution produced depends on processing and heat treatment. Fig. 4.12. shows the initial coarse microstructure produced by solution – treatment and analyzed by optical microscopy. As expected, the grain size increases after heat treatment for the microstructures of IN718 of the received alloy before hot torsion deformation. High temperature torsion results in substantial grain refining due to the occurrence of DRX.

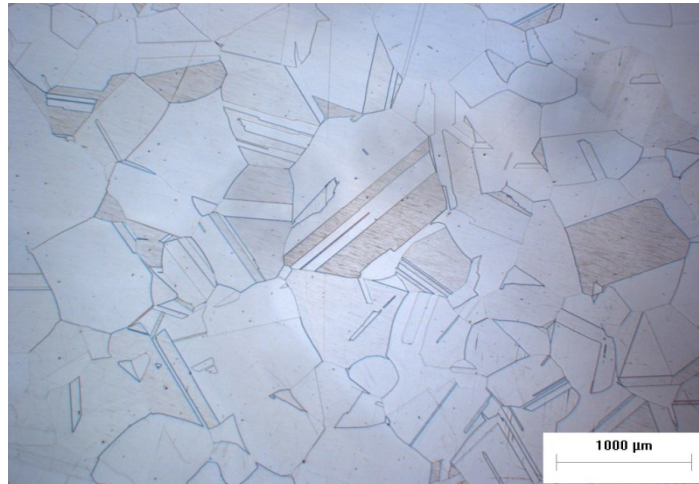
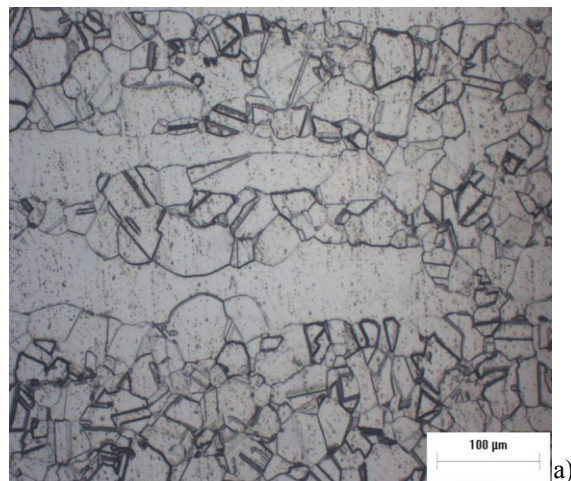


Figure 4.12: *Microstructure of the received alloy (IN 718), heat treatment 1150 °C for 4 h (Light optical microscopy), before a hot torsion deformation.*

In Fig. 4.13. (a, b, c & d), the microstructures results are reported for the specimens deformed at 1100 °C and 1000 °C at different strain rates corresponding to 1 and 0.01 s⁻¹. As expected, it is clearly observed that increasing temperature leads to higher tendency to DRX. Higher testing temperature produces coarser grains, which was expected, while the smaller grain size observed under lower strain rates is somewhat unusual. The sluggish kinetics of DRX in this material seems to be the characteristic of high Ni alloys and is in sharp contrast to the fast DRX in other alloys such as stainless steels. The figures below indicate the influence of increase in strain rate from 0.01s⁻¹ to 1s⁻¹ on the microstructure of DRX at two deformation temperatures of 1000 °C and 1100 °C.

It is quite evident that increasing strain rate has favored the progress of DRX, especially at 1100 °C. In order to shed more light on the mechanism of DRX, typical magnified views of deformed microstructures are shown in the figures. It is clear that the new small DRX grains have formed at the vicinity of grain boundaries. The strain gradient that is usually present inside the grains seems to be responsible for the nucleation of DRX grains around grain boundaries. It is well known that more slip systems operate at the grain boundary regions to adapt different strain levels of adjacent grains. Therefore, microstructural events commence primarily at the grain boundary regions and then are spread out to the grain's interiors.



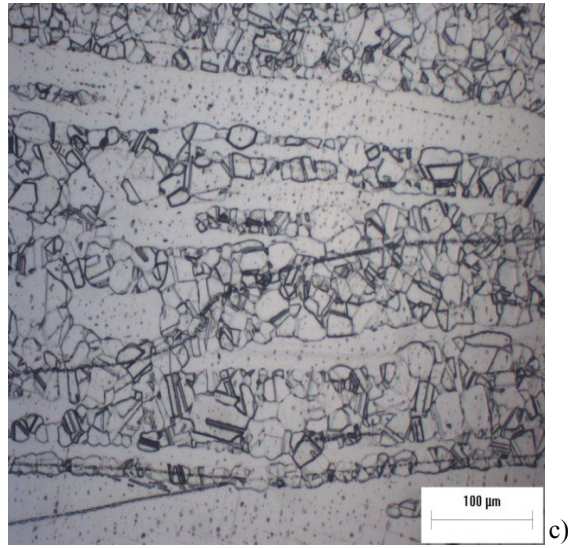




Figure 4.13: Optical images of the IN718 alloy microstructure deformed at: (a) 1100 °C, 1 s⁻¹; (b) 1100 °C, 0,01 s⁻¹; (c) 1000 °C; 1 s⁻¹; (d) 1000 °C, 0,01 s⁻¹.

4.8. Basic creep modelling of Nickel and single-phase Ni based superalloy

The basic model that will be used here to describe the high-temperature deformation under constant strain rate of IN718, was originally developed for Cu [91] [92]. The model is based on physically-derived equations, which will be illustrated here for a single-phase alloy containing elements in solid solution.

The free dislocation density (ρ)[91], is usually related to the applied stress by the Taylor equation,

$$\sigma = \sigma_i + \sigma_{ss} + \sigma_d = \sigma_i + \sigma_{ss} + \alpha m G b \sqrt{\rho} \quad (4.14)$$

where m is the Taylor factor (3.06 for fcc metals), b is the length of the Burgers vector and $\sigma_d = \alpha m G b \rho^{1/2}$ is the dislocation hardening term. The term σ_i represents the stress required to move a dislocation in the absence of other dislocations, while α is a constant. In solid solution alloys, where the viscous drag of dislocations reduces dislocation mobility, the term σ_{ss} represents the stress required for dislocations to move in presence of solute atoms atmospheres. The evolution of the dislocation density during straining can be expressed as[92].

$$\frac{d\rho}{d\varepsilon} = \frac{m}{bL} - \omega\rho - \frac{2}{\varepsilon} M \tau_l \rho^2 \quad (4.15)$$

where ω is a constant, τ_l is the dislocation line tension ($\tau_l = 0.5 G b^2$), M is the dislocation mobility and L is the dislocation mean free path, i.e. the distance travelled by a dislocation before it undergoes a reaction, customarily expressed as

$$L = \frac{C_L}{\sqrt{\rho}} \quad (4.16)$$

C_L being the strain-hardening constant[91][92].

The first term on the right-hand side of Eqn. (4.15) represents the strain hardening effect due to dislocation multiplication. The second and third terms at the right-hand side of Eqn. (4.15) describe the effect of dynamic recovery. Since at high temperature, the last term into Eqn. (4.15) largely predominates on the second term, and our main emphasis in this study is to describe high-temperature behaviour ($T \geq 950^\circ\text{C}$), Eqn.(4.15) can be simplified as,

$$\frac{d\rho}{d\varepsilon} = \frac{m}{bL} - \frac{2}{\dot{\varepsilon}} M \tau_l \rho^2 \quad (4.17)$$

The dislocation climb mobility in a solid solution strengthened alloy, assumes the form[87][91][92]:

$$M \cong \frac{D_{omb}}{kT} \exp\left[\frac{\sigma_d b^3}{kT}\right] \exp\left\{-\frac{Q_m}{RT}\left[1 - \left(\frac{\sigma_d}{R_{max}}\right)^p\right]^q\right\} \exp\left(-\frac{U_{ss}}{RT}\right) \quad (4.18)$$

where R_{max} , which depends on material structure, is the flow stress required to plastically deform the material in the absence of thermal activation and $D=D_{om}\exp(-Q_m/RT)$ is the appropriate diffusion coefficient, (Q_m is thus the activation energy to overcome the obstacle field). Recent studies[87][92][93], showed that Eqn.(4.18) works very well for pure Cu and Al with $p=2$ and $q=1$, with $R_{max}=1.2-1.5R_{uts}$, where R_{uts} is the ultimate tensile strength. The U_{ss} term has been introduced to take into account that during viscous glide in solid solution alloys, solute atoms have to jump in-

and out the atmospheres that spontaneously form around dislocations. Thus, an additional term, describing the energy due to overcome this barrier, must be added to the activation energy. This additional term has the form[94]:

$$U_{ss} = \frac{\beta R}{bk} \quad (4.19)$$

With

$$\beta = \frac{1}{3\pi} \frac{(1+\nu)}{(1-\nu)} bG\Omega\delta_i \quad (4.20)$$

where ν is the Poisson's ratio, Ω is the average atomic volume and δ_i is the volume atomic misfit for the i -species in solid solution, (details about Ω and δ_i calculation in complex alloys are given in [94]. At steady state, (a condition here assimilated to the peak) Eqn. (4.17) gives:

$$\dot{\epsilon} = \frac{2M\tau_l b C_L}{m} \left(\frac{\sigma_d}{\alpha m G b} \right)^3 \quad (4.21)$$

The model based on the combination of Eqns. (4.18) and (4.21), which obviously does not take into account DRX, requires the determination of C_L ($C_L = 86$ in pure Al[93]) and of the two terms which appear into Eqn. (4.14), namely σ_i and σ_{ss} . The determination of σ_i , which is temperature and strain rate dependent, in the case of a pure metal, was based on the assumption that the annealed dislocation density and the- σ_i values account for the annealed, yield strength of the pure metal[93]. The yield stress is thus given by Eqn.(4.14) [95], where the dislocation density is virtually nihil.

The traditional way of describing the temperature dependence of the yield strength is to assume that in the creep range, the yield strength is proportional to the creep strength, whereas below the creep range the yield strength is proportional to the shear modulus. On these bases, the following expression was used in[93]

$$\sigma_i = A_y \sqrt{\sigma G} \quad (4.22)$$

where σ was the creep stress which, for the considered pure metal, corresponded to a given steady state creep rate, or the peak flow stress obtained at a given testing strain rate. The A_y constant was determined to obtain a reliable estimate of the yield strength at room temperature. An equation for solid solution strengthening stress was given in[94], in the form:

$$\sigma_{ss} = \frac{v_d c_{iss} \beta^2}{b \Omega D_{iss} k T} I(z_0) \quad (4.23)$$

where v_d is the dislocation velocity, being c_{iss} the atomic concentration of the i-species in solid solution and $D_{iss} = D_{0iss} \exp(-Q_{iss}/RT)$ is the diffusivity of the i-species in the matrix. The term $I(z_0)$ can be calculated by numerical integration of

$$I(z_0) = \int_1^{z_0} \frac{2\sqrt{2\pi}}{3} z^{-5/2} \exp(-z) dz \quad (4.24)$$

with $z_0 = \beta/bkT$.

4.9. Description of pure Nickel

To properly describe the stress-strain rate relationship for a complex material like IN718, one has to first apply the basic model to the parent-alloy, i.e. pure Nickel. Fig.4.14 plots the peak flow stress as a function of strain rate for pure Nickel as obtained by Luton and Sellars [61].

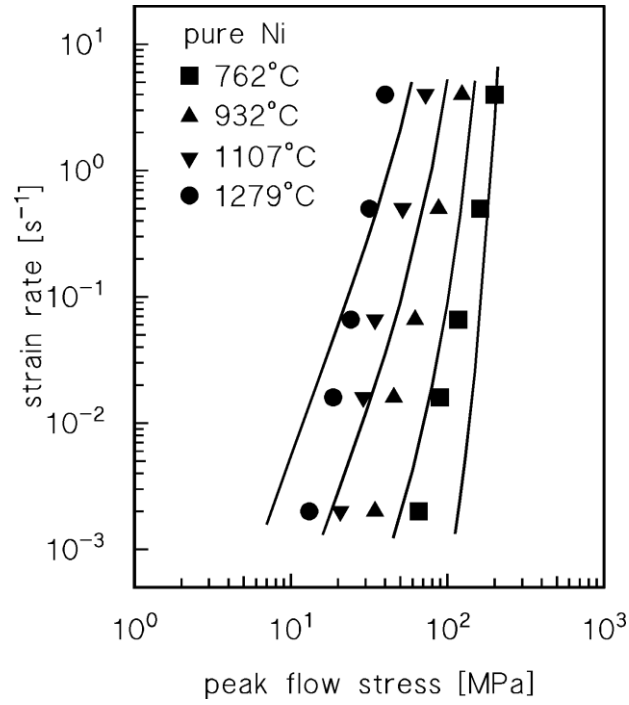


Figure 4.14: Peak-flow stress in pure Ni[61]. The curves were calculated by the model equation described in Section 3.6, with $G=(93 \times 10^4 - 36T)[\text{MPa}][96]$, $R_{\max}=570 \text{ MPa}$ ($=1.5R_{\text{UTS}}$), $D=D_{\text{Ni}}=2 \times 10^{-4} \exp(290/RT) [\text{m}^2 \text{s}^{-1}][97]$, $U_{\text{ss}}=\sigma_{\text{ss}}=0$, $p=2$, $q=1$ and $C_L=86$.

This data was used to assess the predictive capability of the basic model, taking $G=(93 \times 10^4 - 36T)$ [MPa] [96], $R_{max}=570$ MPa ($=1.5R_{UTS}$) and D equivalent to the vacancy diffusivity in Ni ($D=D_{Ni}=2 \times 10^{-4} \exp(290/RT)$ [m^2s^{-1}] [97]. The only variation with the procedure reported in [93] was that the R_{max} term was recalculated at each T by taking into account the temperature dependence of the shear modulus, (that is, it was here assumed that the ratio R_{max}/G remains constant with increasing temperature). The A_y term ($=0.0035$) was estimated by assuming a yield stress at room temperature close to 25 MPa with an initial (annealed) dislocation density of $1 \times 10^{11} m^{-2}$. The curves presented in Fig. 4.14 were then obtained with $U_{ss}=\sigma_{ss}=0$, $p=2$, $q=1$ and $C_L=86$ as in pure Al [93]. In fact, the model captures the general trend of the experimental data, but strongly overestimates the effect of temperature in the low stress regime. To fully understand the reasons for this behaviour, Fig. 4.15 plots the K_σ term:

$$K_\sigma = \left[1 - \left(\frac{\sigma_d}{R_{max}} \right)^p \right]^q \cong \frac{Q_{HT}}{Q_{sd}} \quad (4.25)$$

where Q_{HT} is the experimental value of the activation energy for high-temperature deformation, and Q_{sd} is the activation energy for vacancy diffusion, (the K_σ term does not exactly equal Q_{HT}/Q_{sd} due to the complex temperature dependence of the M term).

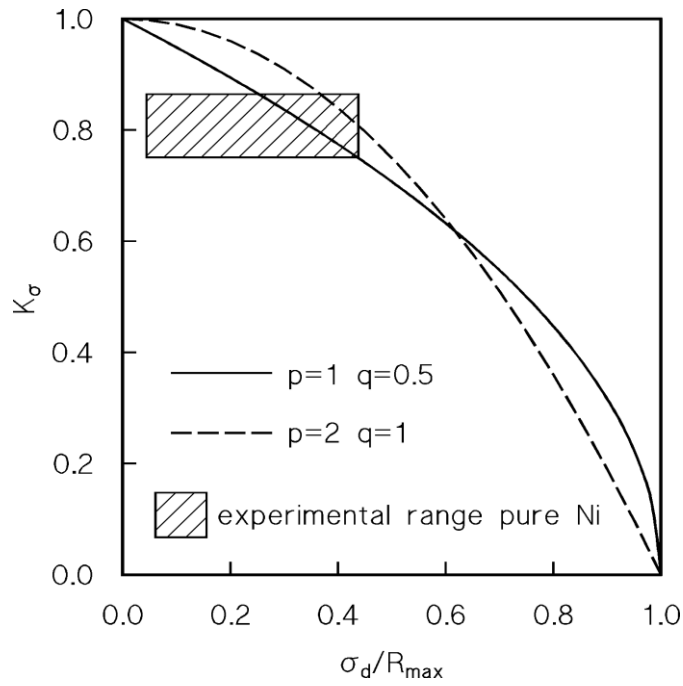


Figure 4.15: Plot of the K_σ term as a function of σ_d/R_{UTS} for $p=2$ and $q=1$, or $p=1$ and $q=0.5$. The boxed area represents the interval of activation energy values obtained in [61].

The activation energy for high-temperature deformation can be calculated as:

$$Q_{HT} = \left[\frac{\partial \ln \dot{\epsilon}}{\partial \left(-\frac{1}{RT} \right)} \right]_{\sigma} \quad (4.26)$$

Luton and Sellars reported an activation energy for high-temperature deformation of $234 \pm 16 \text{ kJ mol}^{-1}$, that is, for an activation energy for self-diffusion in Ni of 290 kJ mol^{-1} . The K_σ range should be between 0.75 and 0.86, with σ_d/R_{\max} ranging from 0.04 to 0.49.

Figure 4.15 clearly shows that assuming $p=2$ and $q=1$, this results in a too high of an estimate of the activation energy for high-temperature deformation. A more reasonable value can be obtained with $p=1$ and $q=0.5$. Fig. 4.16. plots the model curves recalculated with these new p and q values. The agreement with the Luton and Sellars data is now much better, a significant deviation being observed at the two extreme temperatures, in the low strain rate regime.

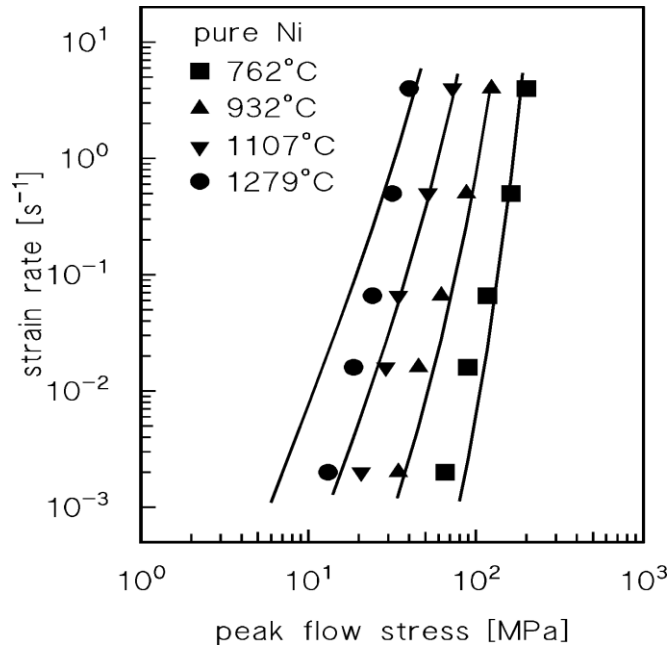
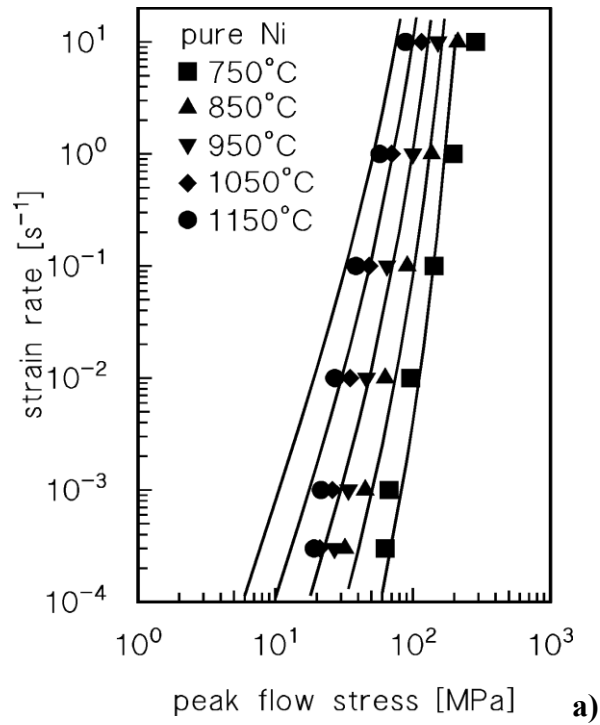


Figure 4.16: Peak-flow stress in pure Ni[61]. The curves were recalculated by the model equation described in Section 4.1, with $G=(93 \times 10^4 - 36T)$ [MPa] [96], $R_{\max}=570$ MPa ($=1.5R_{UTS}$), $D=D_{Ni}=2 \times 10^{-4} \exp(-290/RT)$ [m^2s^{-1}] [97], $U_{ss}=\sigma_{ss}=0$, $p=1$, $q=0.5$ and $C_L=86$

Fig. 4.17. plots the model curves for another dataset, obtained by compression testing [86], and for creep experiments carried out at lower temperatures [98]. In the case of compression data, the agreement between model curves and the experimental data is more than reasonable, although a deviation appears in the very low strain rate regime. Fig. 4.17 b., shows that the model provides a good description also of the creep data, obtained under lower stresses and at lower temperatures. On these bases, the assumption $p=1$ and $q=0.5$ will be maintained in the following.



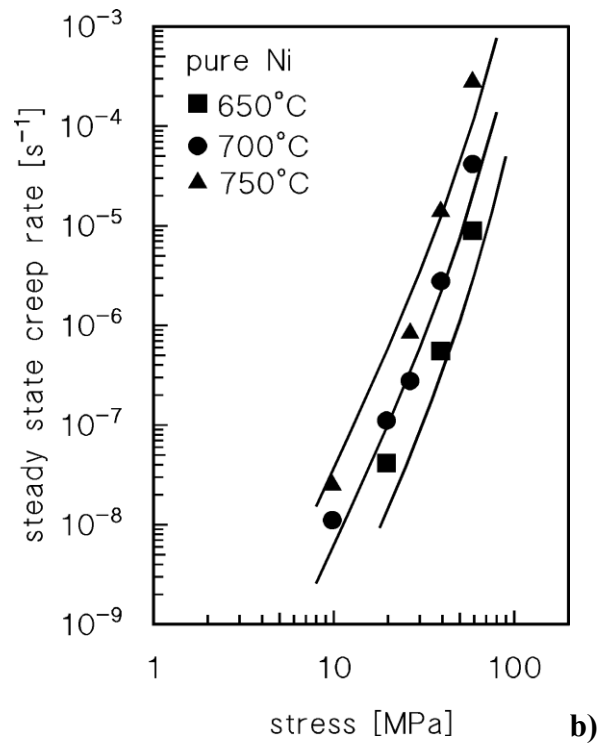


Figure 4.17: a) Peak-flow stress in pure Ni by compression testing[86]; b) steady state creep rate a function of applied stress[98]. The model curves were calculated as in Figure 4.15.

4.10. Description of IN718 solutioned alloy

The application of the basic modelling for pure Ni gave very good results with $D_{0sd}=2 \times 10^{-4} \text{m}^2 \text{s}^{-1}$, $Q_{sd}=290 \text{ kJ mol}^{-1}$, $A_y=3.5 \times 10^{-3}$, $C_L=86$, $p=1$ and $q=0.5$. The same values could be used to model the peak flow stress variation with strain rate for the solutioned IN718 alloy, provided that R_{max} , σ_{ss} and U_{ss} are properly estimated. This task, in the case of R_{max} is straightforward, since it could be obtained as $1.5R_{UTS}$, being $R_{UTS} \cong 800 \text{ MPa}$, and then be recalculated at each temperature to take into account the variation of G , as in pure Ni. The calculation of the U_{ss} and of the drag stress term is a more complex affair. An initial rough estimate of U_{ss} can be obtained for simple Ni-X binary alloys by Eqns. (4.19) and (4.20), where δ_i is obtained from [99]. Calculation for X=Al, Ti and Mo, for example, gives at $T/T_m=0.77$, $U_{ss}=9, 18$ and 32 kJ mol^{-1} respectively (to be compared with the value close to 14 kJ mol^{-1} in the same range of homologous temperature, for Al-Mg alloys). Although it has been demonstrated that a first-principles evaluation could also be made in the case of multi-component alloys containing different elements in solid solution[94][99], in which the average atomic volume should be calculated, a simpler procedure will be followed here. The first point to be discussed is the relationship between the applied stress and the drag stress. The analysis in[87] demonstrated that in Al-Mg solid solution alloys, the drag stress, in the high temperature and low stress regime, (that is, below the break-away of dislocation from solute atoms atmospheres), is roughly proportional to the applied stress, i.e.

$$\sigma_{ss} = K_c \sigma \quad (4.27)$$

with $K_c \approx 0.29$ for 2% Mg, independent on the testing temperature (Fig.4.18).

Let one maintain that Eqn. (4.27) is fulfilled in the case of IN718.

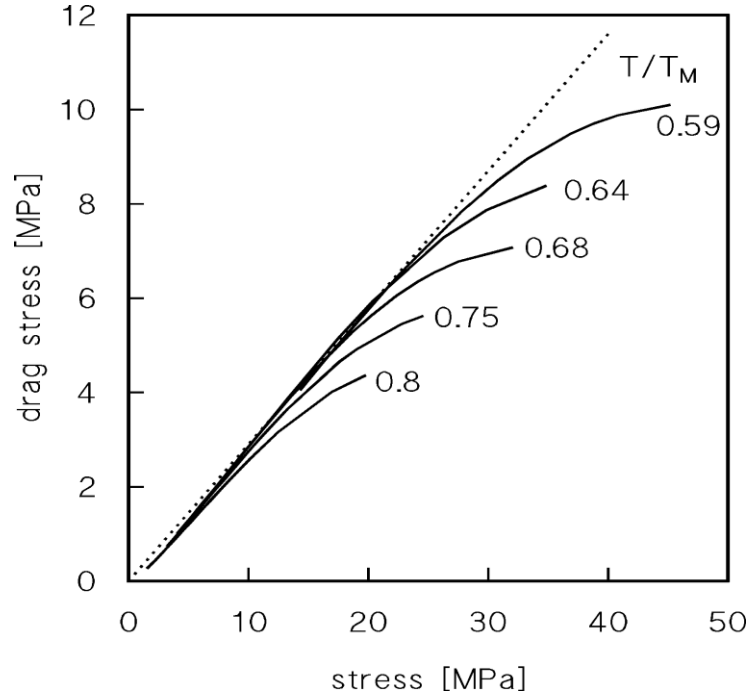


Figure 4.18: Plot of the drag stress as a function of applied stress for Al-2%Mg[87]. The curves obtained at different homologous temperatures overlap on a straight line in the low stress regime.

Then, any difference in the value of the activation energy for high-temperature deformation should only depend on the magnitude of the U_{ss} term. The analysis of the experimental data gave $Q_{HT} \approx 345 \text{ kJ mol}^{-1}$.

Eqn. (4.21), for a given material with a constant amount of elements in solid solution, could be rewritten, by considering only the temperature-dependent terms:

$$\dot{\epsilon}_{ss} \propto \left[\frac{\sigma - \sigma_i - K_c \sigma}{G(T)} \right]^3 M(T) \cong \left[\frac{\sigma - K_c \sigma}{G(T)} \right]^3 M(T) \propto \left[\frac{\sigma}{G(T)} \right]^3 M(T) \quad (4.28)$$

Substitution of Eqns. (4.18) and (4.28) into Eqn. (4.26) gives the variation of the activation energy for hot working with U_{ss} . Thus, once the complex temperature dependence of the M term is taken into account, one easily ascertains that $Q_{HT} = 345 \text{ kJ mol}^{-1}$ for $U_{ss} = 30 \text{ kJ mol}^{-1}$, which is comparable with the value obtained in Ni-Mo binary solid solutions. The last parameter to be calculated is the K_c constant. Equation (4.14), at room temperature, in correspondence with the ultimate tensile strength, becomes:

$$R_{UTS} = \sigma_i + K_c R_{UTS} + \alpha m G b \sqrt{\rho_{UTS}} \quad (4.29)$$

Where σ_i should be the same as that calculated for pure Ni, (the effect of a difference in grain size is neglected here), i.e. 19 MPa, $R_{UTS} = 800 \text{ MPa}$, and ρ_{UTS} is the dislocation density at rupture. Typical dislocation density values at rupture at room temperature should largely exceed $1 \times 10^{14} \text{ m}^{-2}$. Let one assume $\rho_{UTS} = 5-7.5 \times 10^{14} \text{ m}^{-2}$, one obtains K_c ranging from 0.33 and 0.45. Comparison with experimental data at 1000°C shows that an excellent description is indeed obtained with $K_c = 0.37$. Fig. 4.19 thus, plots the model, curves calculated with $R_{max} = 1215 \text{ MPa}$, $U_{ss} = 30 \text{ kJ mol}^{-1}$, $K_c = 0.37$. The description of the data is excellent.

Fig. 4.20. shows the experimental data obtained by Azarbarmas and coworkers[90] by testing in compression in an equivalent range of temperature an IN718 solutioned at 1050°C-1 h. The Figure also plots the model curves obtained in the present study, (actually, the same curves presented in Figure 4.19, extrapolated in a wider range of strain rates). The analysis of the Figure reveals that the model gives an excellent description of the tests carried out at 1100°C, while slightly underestimates the peak flow stress at the lower temperature.

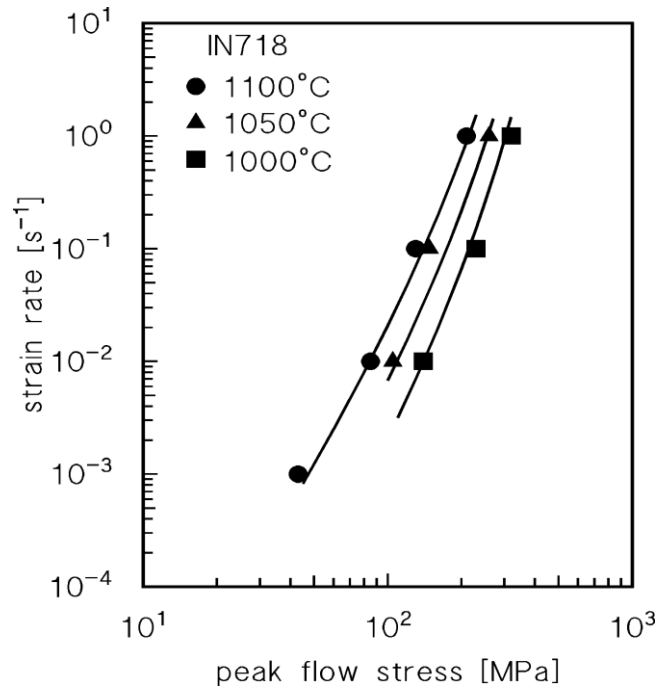


Figure 4.19: Peak flow stress as a function of the strain rate for solution treated IN718 ($G=(93 \times 10^4 - 36T)$ [MPa][96], $R_{max}=1215$ MPa ($=1.5R_{UTS}$), $D=D_{Ni}=2 \times 10^{-4} \exp(290/RT)$ [$m^2 s^{-1}$][97], $U_{ss}=30$ kJ mol⁻¹, $\sigma_{ss}=0.37\sigma$, $p=1$, $q=0.5$ and $C_L=86$)

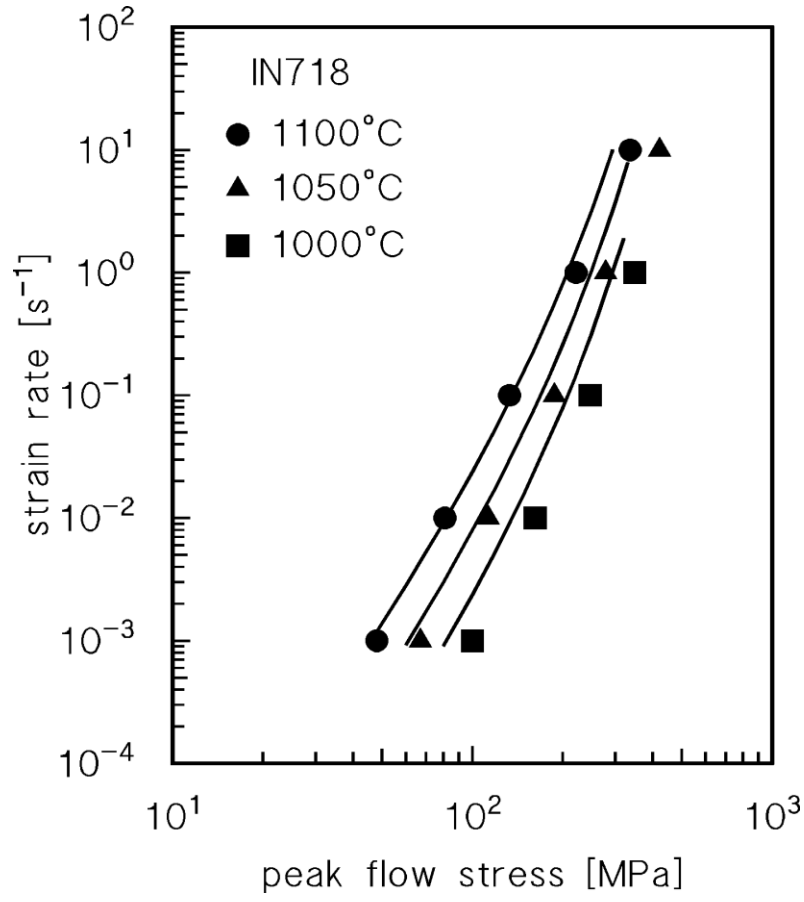


Figure 4.20: Peak flow stress as a function of the strain rate for 1050°C-1 h solution treated IN718[99], with $(G=(93 \times 10^4 - 36T) \text{ [MPa] [96]}$, $R_{max}=1215 \text{ MPa } (=1.5R_{UTS})$, $D=D_{Ni}=2 \times 10^{-4} \exp(-290/RT) \text{ [m}^2\text{s}^{-1}\text{][97]}$, $U_{ss}=30 \text{ kJ mol}^{-1}$, $\sigma_{ss}=0.37\sigma$, $p=1$, $q=0.5$ and $C_L=86$

As a matter of fact, Azarbarmas et al. [90] obtained an activation energy for high-temperature deformation of 437 kJ mol^{-1} , that is, 100 kJ mol^{-1} higher than in the present study. The deviation between the model and the data in [90], on the other hand, can be easily explained if one takes into account the different solution treatment temperatures and durations. Fig. 4.21. plots the variation of the tensile strength with solution treatment temperature (for 1h duration, from [100]). The curve for yielding is substantially parallel and shifted of 400 MPa toward lower values of the stress. It can be easily appreciated, that the increase of the solution treatment temperature from 1050 to 1100°C causes an 80 MPa decrease of the tensile strength. Since major grain coarsening was not observed due to the relatively low duration of high temperature exposure, the only reasonable explanation of the behaviour illustrated in Fig. 4.21, is that heating at 1050°C for 1h causes an incomplete dissolution of the secondary phase precipitates. Thus, a residual amount of precipitates can be expected when the material is deformed at 1050 or 1000°C, and, as a result, a particle-strengthening contribution should be considered. By contrast, heating at 1100°C before compression testing, causes the complete solubilisation of the alloy, which behaves as the IN718 solution treated at the same temperature investigated in the present study. The accuracy of the equations in describing the temperature and strain rate dependence of the peak stress of the single-phase IN718 superalloy provides an excellent validation of the model, which thus constitutes an ideal physical basis for further developments in the case of multi-phase microstructures.

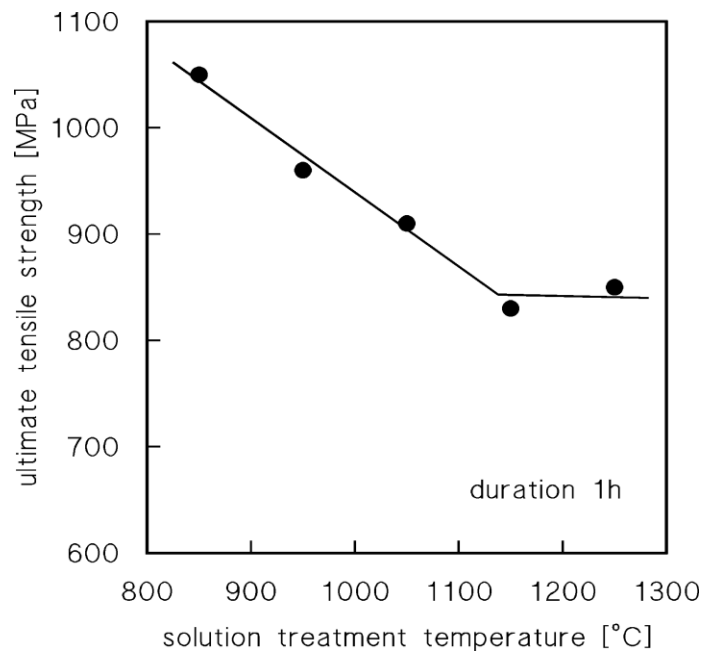


Figure 4.21: Variation of the ultimate tensile strength with solution treatment temperature, for a standard duration of 1h (data from[90]).

4.11. Summary and Conclusions

In this chapter, a basic model was applied to pure Ni and then to a single-phase superalloy. The high temperature deformation of the superalloy, a solution treated IN718, was investigated by torsion testing in a high-temperature regime (1000–1100 °C) where no precipitation of secondary phases was expected. The high-temperature deformation of the solution treated IN718 superalloy was investigated in a temperature range selected to avoid any form of precipitation during straining. The superalloy exhibited the classical behavior of materials that undergo DRX. The peak-flow stress dependence on temperature and strain rate was described using the classic phenomenological approach, based on Garofalo and Arrhenius equations, obtaining an activation energy high-temperature deformation of 345 kJ mol⁻¹. An alternative physically-based approach, developed for creep of fcc metals, was then used to describe the response of pure Ni in the first instance, and then applied to the solution treated IN718 single-phase alloy. The model, in the form used in the present study, takes into account both dislocation hardening and solid solution strengthening, and presents an important advantage over traditional phenomenological approaches, since it is predictive. Once the different parameters which appear in the model were properly calculated, an excellent description of the experimental peak flow stress dependence on strain-rate and temperature was obtained. This finding confirms that a model, originally developed for describing creep of pure Cu, is indeed fully able to describe the high-temperature deformation of Ni.

Chapter 5.

Physical Modeling of The Creep Response for Al-Cu-Mg Alloy Produced by Friction Stir Processing

Within this chapter, the creep response of an Al-Cu-Mg 2024 Aluminum alloy with refined microstructures produced friction stir processing (FSP) will be discussed. A constitutive model based on a thermotical approach has been used to correlate the microstructure features and creep properties. The hardness variation with creep duration is used to quantify the particle strengthening term.

5.1. Introduction

The creep response of AA 2024-T3 aluminium alloy with a refined microstructure produced by Friction Stir Processing (FSP) was considered. The material investigated in the present study was a commercial AA2024-T3 aluminium alloy. A thermomechanical process, such as the FSP, alters the temper condition of the parent metal and produces distinct variations across the affected regions of the material. Also, it is interesting to note that modifications in the FSP parameters can alter the corrosion susceptibility of an alloy.

This is because the modifications introduce different degrees of deformation and thermal cycles[101][102]. AA2024 alloy is an advanced aluminum alloys for aerospace application are required to possess high fracture toughness, high fatigue performance, high formability, and super plasticity to meet the needs for lower structural weight, higher damage tolerance, and higher durability[101][103].The heat-treatable 2024-T3 aluminum alloy, reported in this investigation, has attractive features of high strength and that its ductility does not significantly decrease during the strengthening heat treatment. This alloy has an excellent strength vs. density ratio, formability and corrosion resistance which make the high-copper Al-Cu-Mg alloys a potential candidate for a number of industrial applications[104]. Also, they are mainly considered as a substitute of iron-based materials for structural parts in the transportation industry, So, in this type of alloy, the aluminum is the primary constituent and Copper has been the most common alloying element almost since the beginning of the aluminum industry, and a variety of alloys in which copper is the major addition were developed. Magnesium is usually combined with copper. The constituents formed in the alloys containing only one or more of copper, magnesium, etc. are soluble ones. Depending on the alloy composition (% Cu content and Cu/Mg ratio), different phase distributions and consequently different material characteristics can be obtained[105]. A constitutive model based on a theoretical approach has been used to correlate microstructural features and creep properties. The basic models have been developed by Sandström, to describe the creep response of pure Cu[106], and was applied to Ni in the previous chapter.

5.2. Creep and Creep testing

Creep of materials is classically associated with time-dependent plasticity under a fixed stress at an elevated temperature, often greater than roughly $0.5T_M$, where T_M is the absolute melting temperature. The plasticity under these conditions is described in Figure 5.2 for constant stress (1) and constant strain rate (2) conditions. As the characteristic aspect of the curve, three regions are delineated; Stage I, or primary creep, denotes that portion where the creep rate (plastic strain rate), $\dot{\epsilon}$ ($= d\epsilon/dt$) is changing with increasing plastic strain or time. In Fig. 5.2a. the primary creep rate decreases with increasing strain, but with some types of creep, such as solute drag with “three power creep,” an “inverted” primary occurs where the strain rate increases with strain. Analogously, in Fig. 5.2b., under constant strain-rate conditions, the metal hardens, resulting in increasing flow stresses. Often, in pure metals, the strain rate decreases or the stress increases to a value that is constant over a range of strain. The phenomenon is termed Stage II, secondary, or steady-state creep. Eventually, cavitation and/or cracking increase the apparent strain rate or decrease the flow stress. This regime is termed Stage III, or tertiary creep, and leads to fracture. Sometimes, Stage I leads directly to Stage III and an “inflection” is observed. Thus, care must sometimes be exercised in concluding a mechanical steady state (ss).

The term “creep” as applied to plasticity of materials likely arose from the observation that at modest and constant stress, at or even below the macroscopic yield stress of the metal (at a “conventional” strain rate), plastic deformation occurs over time as described in Fig. 5.2a. This is in contrast with the general observation, such as at ambient temperature, where, a material deformed at, for example, $0.1\text{--}0.3 T_M$ shows very little plasticity under constant stress at or below the yield stress, again, at “conventional” or typical tensile testing strain rates (e.g., $10^{-4}\text{--}10^{-3} \text{ s}^{-1}$)[48][107]. The latter observation is not always true as it has been observed that some primary creep is observed (e.g., a few percent strain, or so) over relatively short periods of time at stresses less than the yield stress in some ‘rate- sensitive’ and relatively low strain-hardening alloys such as titanium and steels[107]. The creep test is conducted using a tensile specimen to which a constant stress is applied, often by the simple method of suspending weights from it. Surrounding the specimen is a thermostatically controlled furnace, the temperature being controlled by a thermocouple attached to the gauge length of the specimen, Fig.5.1. The extension of the specimen is measured by a very sensitive extensometer since the actual amount of deformation before failure may be only two or three per cent. The results of the test are then plotted on a graph of strain versus time to give a curve similar to that illustrated in Fig.5.2.

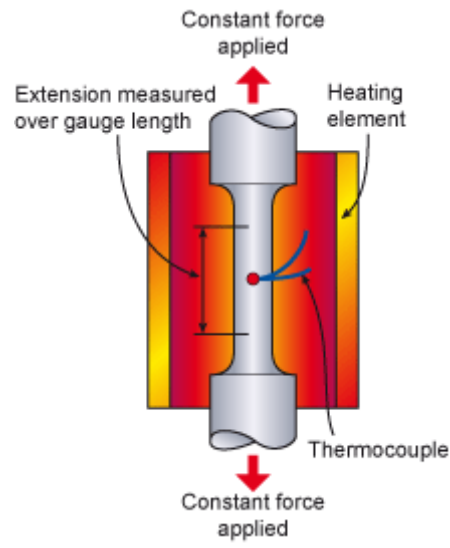


Figure.5.1: Schematic of a creep test[108].

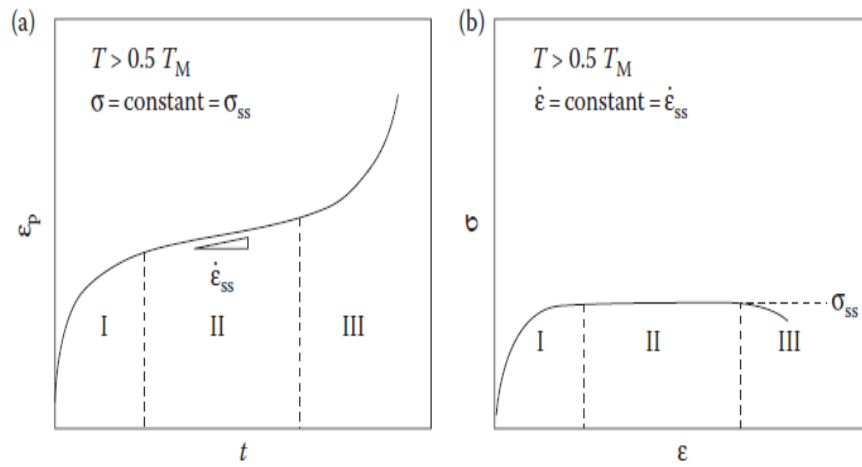


Figure.5.2: Constant true stress (a) and constant strain rate (b) creep behavior in pure and Class M (or Class I) metals[48].

The test specimen design is based on a standard tensile specimen. It must be proportional in order that results can be compared and ideally should be machined to tighter tolerances than a standard tensile test piece. In particular the straightness of the specimen should be controlled to within some $\frac{1}{2}\%$ of the diameter. A slightly bent specimen will introduce bending stresses that will seriously affect the results. The surface finish is also important - the specimen should be smooth, scratch free and not cold worked by the machining operation[109]. The extensometer should be fitted on the gauge length and not to any of the other load carrying parts as it is difficult to separate any extension of these parts from that in the specimen. Testing is generally carried out in air at atmospheric pressure. However, if it is necessary to produce creep data for materials that react with air these may be tested in a chamber containing an inert atmosphere such as argon or in a vacuum. If the material is to operate in an aggressive environment then the testing may need to be carried out in a controlled environment simulating service conditions. Fig.5.2. shows that creep failure occurs in three distinct phases - a rapid increase in length known as primary creep where the creep rate decreases as the metal work hardens[107]. This is followed by a period of almost constant creep rate, steady state or secondary creep and it is this period that forms the bulk of the creep life of a component. The third stage, tertiary creep, occurs when the creep life is almost exhausted, voids have formed in the material and the effective cross-sectional area has been reduced. The creep rate accelerates as the stress per unit area increases until the specimen finally fails.

The creep test has the objective of precisely measuring the rate at which secondary or steady state creep occurs. Increasing the stress or temperature has the effect of increasing the slope of the line, the amount of deformation in a given time increases. There are therefore two additional variations on the creep test that use the same equipment and test specimen as the standard creep test and that are used to provide data for use by the designer in the latter case. These are the creep rupture test and the stress rupture test[107][109]. As the names suggest both of these tests are continued until the specimen fails. In the creep rupture test the amount of creep that has occurred at the point of failure is recorded. The test results would be expressed as % age strain, time and temperature e.g, rupture occurs at 2% strain at 450°C in 85,000 hours. The stress rupture test gives the time to rupture at a given stress and temperature e.g 45N/mm² will cause failure at 450°C in 97,000 hrs. This data, if properly interpreted, is useful in specifying the design life of components when dimensional changes due to creep are not important since they give a measure of the load carrying capacity of a material as a function of time[109].

5.2.1. Phenomenological laws and coefficients

The analytical description of a creep curve as a function of time or strain, which is based solely on elementary mechanisms, is not easy at all. At least the microstructural details (metal, precipitates, grain size, etc.), as well as the contribution of different mechanisms (dislocations, diffusion, grain boundaries) have to be accounted for. In practice, in most cases, measured curves are used.

To estimate the effect of stress σ and temperature T , one focuses generally on stage II (constant creep rate). For those materials that do not exhibit a distinct stage II, the minimum creep rate is used[107]. Consideration of the constant creep rate stage is justified by the fact that it often represents a substantial part of the lifespan of a part. Stage I only lasts a short time, and stage III is not of engineering interest, since the useful lifespan of a structural part has expired by then and the part has to be replaced for safety reasons. In the following, we focus on stage II. The steady state creep rate $\dot{\epsilon}_{ss}$ is a function of both stress (a) and temperature (b), as shown in Fig. 5.3[107][109].

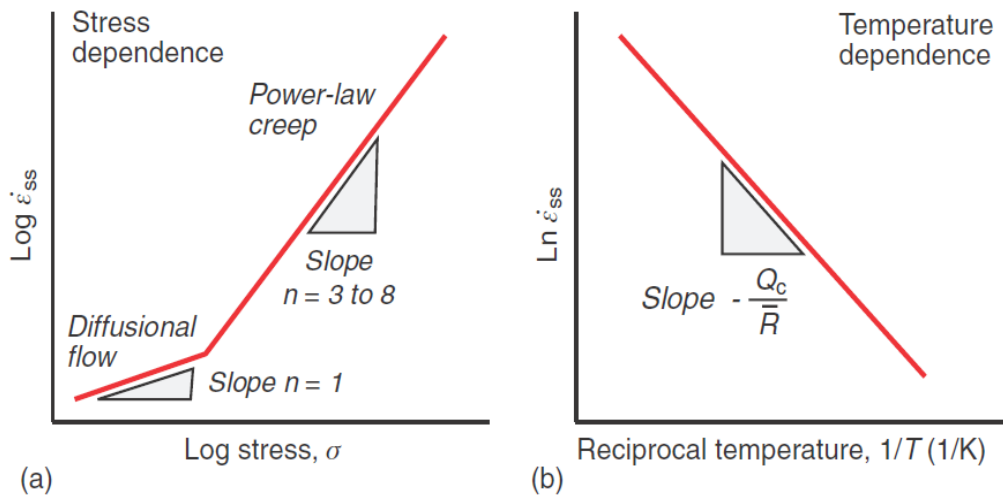


Figure 5.3: Stress and temperature dependence of the steady state creep rate[110].

The stress dependence can be described as:

$$\dot{\epsilon} = B \cdot \sigma \sigma^n \quad (5.1)$$

The temperature dependence as:

$$\dot{\epsilon}_{ss} = C \cdot \exp\left(\frac{-Q_c}{RT}\right) \quad (5.2)$$

Combining gives for the minimum creep rate (i.e., in steady state creep, stage II),

$$\dot{\epsilon}_{ss} = A \cdot \sigma^n \cdot \exp\left(\frac{-Q_c}{RT}\right) \quad (5.3)$$

where A : constant, σ : stress [MPa], n : exponent, Q_c : activation energy [J/mol], $R = 8.314$ J/mol·K (ideal gas constant). When the applied stress is not too high, this law usually gives a satisfactory description of the creep rate as a function of temperature and applied stress. The constant A , the exponent n , and the activation energy for creep Q_c are material characteristics and can be determined from a series of creep tests. The phenomenological law is not precise enough to calculate (by extrapolation) the creep rate at low- temperatures from measurements taken at high stress near the melting temperature, where things happen very fast. The exponent n can be easily determined through a double-logarithmic representation of the creep rate (at $T = \text{constant}$) and the stress.

When the observed results satisfy the law mentioned above, a straight line of slope n should be obtained. Similarly, the logarithm of the creep rate (at constant stress) can be plotted as a function of $1/T$. The slope of the straight line should equal Q_c/R . For pure metals only a few control measures need to be taken, since it is well established that the activation energy for creep corresponds to the activation energy for auto diffusion. This fact is also confirmed by theory, since the stationary creep rate is limited by rearrangements that require the climb of dislocations in the sub grain boundaries. In pure metals, the exponent n varies between 4 and 5 (Norton power law). For single phased alloys (solid solutions), n equals rather 3. In these two metal groups, results obtained at very high temperatures show an exponential dependence of stress such that the creep curve deviates from Norton's law. A very strong dependence can also be observed in precipitate hardened alloys. It is not unusual that n has to be chosen above 10 to describe the experimental results, even at low stress. In order to "save" Norton's law with reasonable exponents (3–5), one may argue that solely the difference between applied stress and the back-stress induced by the precipitates is available for driving creep deformation. The applied stress in Norton's law should then be replaced by the "effective" stress, which corresponds to this difference[107][110].

5.3. Experimental procedure for AA2024-T3

Specimens of a commercial AA2024-T3 aluminum alloy were machined from a plate of 200 mm x 100 mm, 3 mm thickness. The chemical composition is given in table 5.1., The plates were processed by Friction Stir processing (FSP) by using a SHARNOA CNC milling machine, with a rotational speed of 800 rpm and a transverse speed of 80 mm/min. The Friction stir Processing (FSP), invented by (TWI), UK in 1991[111][112], is one of the most promising joining processes for lightweight metals owing to its promising metallurgical advantages compared to conventional fusion welding. Friction stir Processing (FSP) joint generally contains four characteristic zones, i.e. stirred zone (SZ), thermo-mechanically affected zone (TMAZ), heat affected zone (HAZ), and base metal (BM). It has been demonstrated that temperature history, strain and strain rate evolution during FSP significantly affect microstructure of the zones in joints. A schematic diagram illustrating the FSP process is shown in Fig. 5.4. The creep sample shown in Fig. 5.5. with square 3 mm x 3 mm transversal section with 25 mm gauge length were machined from the FSP region of the plates. The longitudinal axis of the samples was parallel to the FSP direction, so that the whole body of the specimen was included in the stir zone. Constant load creep experiments (CLE) and variable load experiments (VLE) were carried out at 250 °C and 315 °C with the initial stress of 50 MPa and 12 MPa, all the experiments are maintained until the starting of the minimum creep rate range. Then, the applied stress was increased one of two times, and then maintained up to sample rupture.

The samples after creep were analyzed by a PhilipsTM CM-200[®] transmission electron microscope (TEM) operated at 200 Kev. The quantitative evaluation of volume, F_V , number fraction, N_V , spacing, λ , and mean size, d_{spp} , of the detected secondary phase rod particles was thus carried out on statistically meaningful number of elements (*i.e.*, at least 300 per experimental condition).

Table 5.1: chemical composition of AA2024-T3 (wt.%) [101]

Cr max	Cu	Fe max	Mg	Mn	Si max	Ti max	Zn max	Al	Other
0.1	3.8-4.9	0.5	1.2-1.8	0.3-0.9	0.5	0.15	0.25	Bal.	0.2

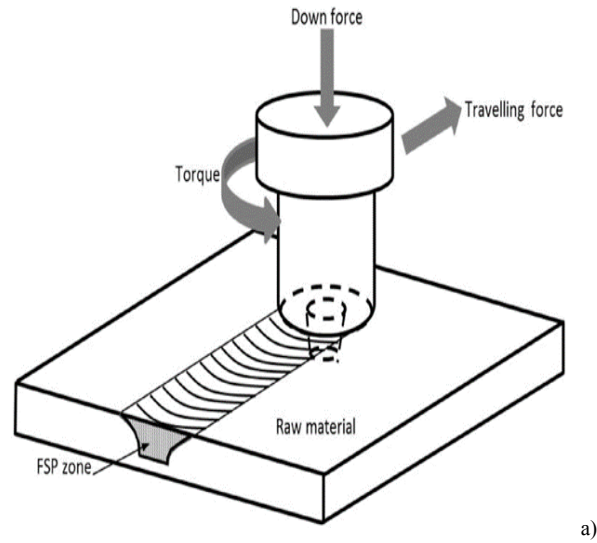




Figure 5.4: Schematic drawing of a) friction stir processing process and b) tool[113].

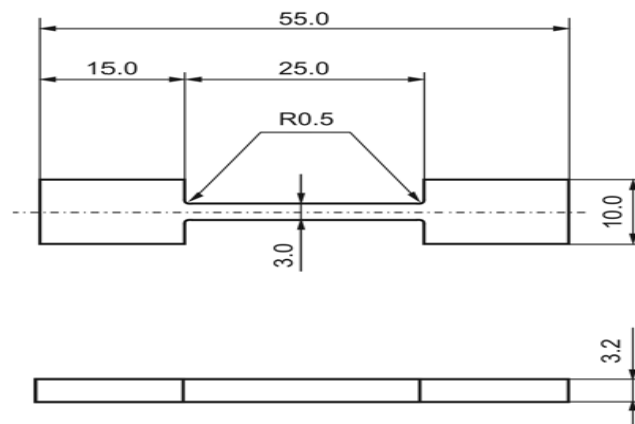


Figure 5.5: Schematic drawing of the Creep specimen[101].

5.4. Results for AA2024-T3

5.4.1. Microstructure evaluation during creep

Within this chapter, the microstructures as a result of FSP processing AA2024-T3 will be discussed. Work describing microstructures developed by FSP is relatively scarce and, of the available literature, processing conditions tend to be omitted. To the date, many publications in the field of FSP of the 2024 aluminum, has been published. Nadammal et al. [112] applied a bottom-up approach for optimizing the process parameters to obtain a defect-free processed material. Their results included mechanical properties and residual stress analysis together with grain size and precipitate studies conducted using Scanning Electron Microscopy (SEM). Charit and Mishra [111] studied the superplastic behavior of friction-stir-processed AA2024-T4. Based on Qualitative-Transmission Electron Microscope (TEM) examination, they claimed that the grain size obtained at the stir zone was $\sim 3.9 \mu\text{m}$. Cavaliere [114] also reported on the superplastic behavior of friction-stir processed 2024 Al alloy and further studied the effect of the addition of Sc and Zr, reporting on the average grain size of $1 \mu\text{m}$ at the stir zone. Suri et al.[115] reported that FSP yielded an improvement in tensile strength of about 20%, while they observed a negligible drop in yield strength with respect to the raw material. Concerning elongation to fracture, Suri et al.[115] pointed to a drop of approximately 40% in the case of processed material. Nadammal et al.[116] studied microstructure and texture evolution during single and multiple pass FSP.

They reported on the formation of equiaxed grains with an average size of 4–5 μm at the stir zone, claiming that Dynamic Recrystallization (DRX) was the dominant mechanism while Particle Stimulated Nucleation (PSN) was a participating nucleation mechanism. Ren et al.[117] studied crack repairing by FSP in the 2024 aluminum alloy. They used optical microscopy for their microstructure study and provided microhardness profiles, but they did not conduct any quantitative analysis of the microstructure at the repaired zone. The alloy after friction stir processing (FSP) is shown in optical and TEM micrographs in Fig. 5.6. The variation of the microhardness is reported in Fig 5.7, which shows that the hardness reaches a maximum value ($\cong 128$ HV), which is lower than the hardness of the parent alloy ($\cong 144$ HV), then it decreases down in the middle section to the minimum value ($\cong 113$ HV). Fig. 5.8. and table 5.2. illustrate the hardness variation with creep time (t_c) at 250 and 315 $^{\circ}\text{C}$, the lowest temperature (T) indicate a decrease in the hardness (HV).

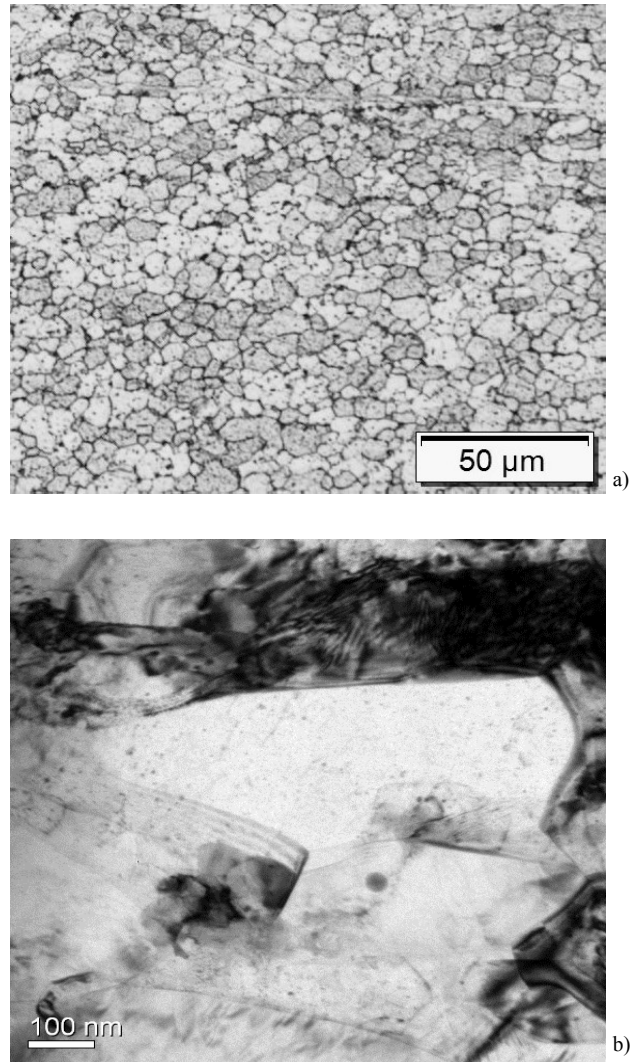


Figure 5.6: Microstructure of the FSP 2024-T3 alloy: a) optical micrograph; b) structure observed by TEM.

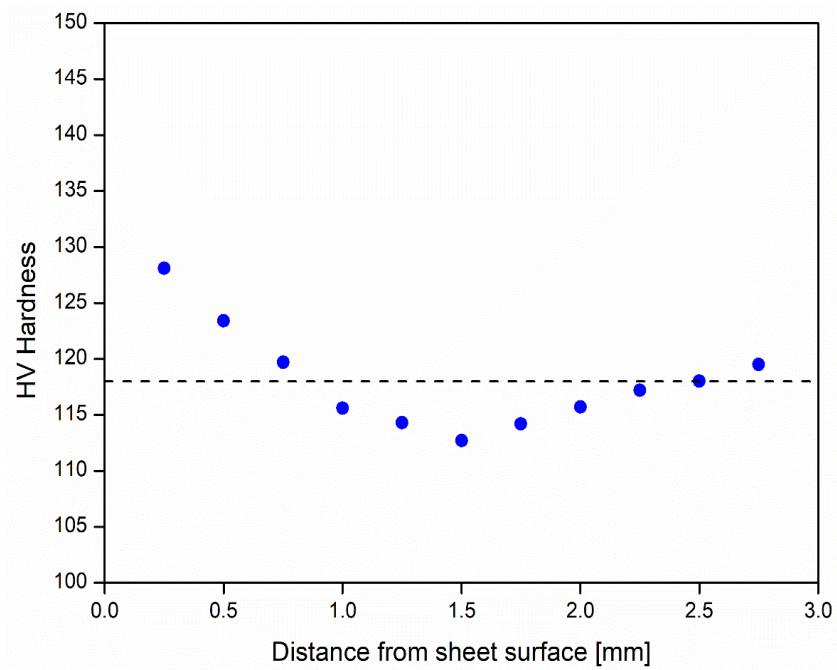


Figure 5.7: *Vickers hardness variation along the thickness of the FSP 2024-T3 alloy, measured in the center of the FSP zone. The broken line represents the average HV value.*

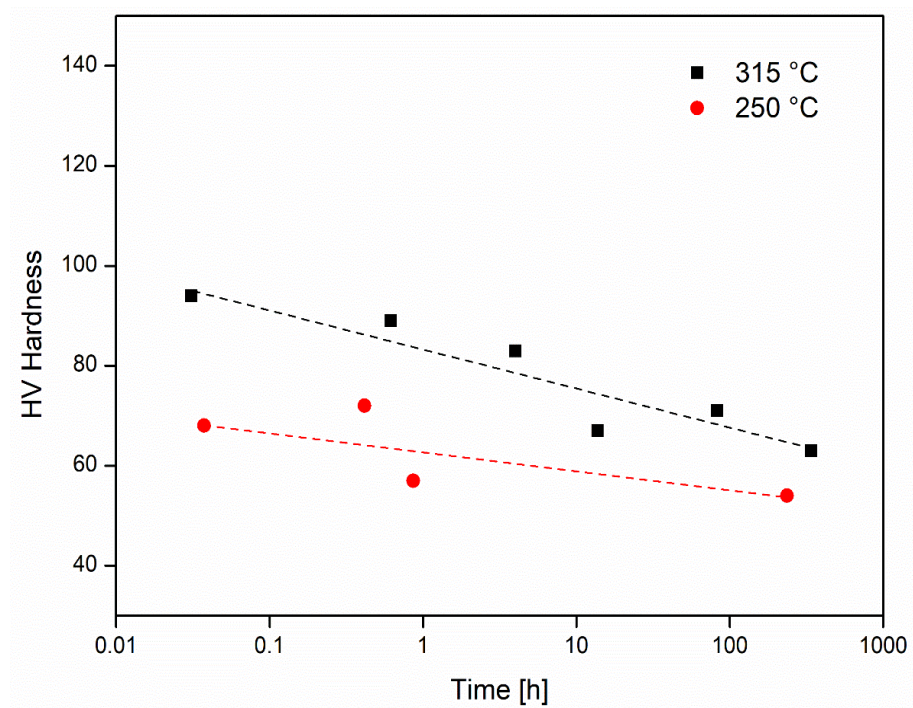


Figure 5.8: Hardness variation as a function of time of exposure (creep test duration) for the sample tested at 250 and 315°C.

Table 5.2: Summary of the experimental results. The strain rate values reported in italic font were those of the VLE.

<i>T</i> [°C]	Load sequence [MPa]	$\dot{\epsilon}_m$ [s ⁻¹]	<i>t_e</i> [h]	<i>HV</i>	λ [nm]	<i>F_v</i> [%]	<i>N_v</i> [μm ⁻³]
250	30	4.0·10 ⁻⁹	337	63 ± 1.0	550	0.06	1
	50-70- 100	1.8·10 ⁻⁷ -2.5·10 ⁻⁶ - 1.2·10 ⁻⁴	82.7	71 ± 0.6	-	-	-
	70	7.2·10 ⁻⁷	13.8	67 ± 2.4	-	-	-
	100	2.5·10 ⁻⁶	4.0	83 ± 1.0	190	0.74	26
	120	8.6·10 ⁻⁶	0.62	89 ± 0.5	-	-	-
	140	2.6·10 ⁻⁴	0.03	94 ± 0.5	110	1.73	138
	140	7.3·10 ⁻⁵	0.98	88 ± 0.5	-	-	-
315	12-50	6.0·10 ⁻⁹ -4.5·10 ⁻⁶	237	54 ± 1.9	-	-	-
	25	8.1·10 ⁻⁷	0.87	57 ± 0.6	-	-	-
	40	1.0·10 ⁻⁵	0.42	72 ± 0.6	-	-	-
	60	2.2·10 ⁻⁴	0.04	68 ± 0.6	-	-	-

In the case of the samples tested at the highest temperature, hardness remains invariably low, and just a moderate further decrease in HV can be observed. Fig. 5.9. shows the hardness as a function of temperature compensated time (*t_c*), expressed as equation (5.4):

$$t_c = t_e \exp \left(-\frac{Q}{RT} \right) \quad (5.4)$$

The hardness data, with $Q \cong 260 \text{ kJ mol}^{-1}$, collapse on a single master curve, that can be profitably used to recalculate the hardness value for the different experimental conditions.

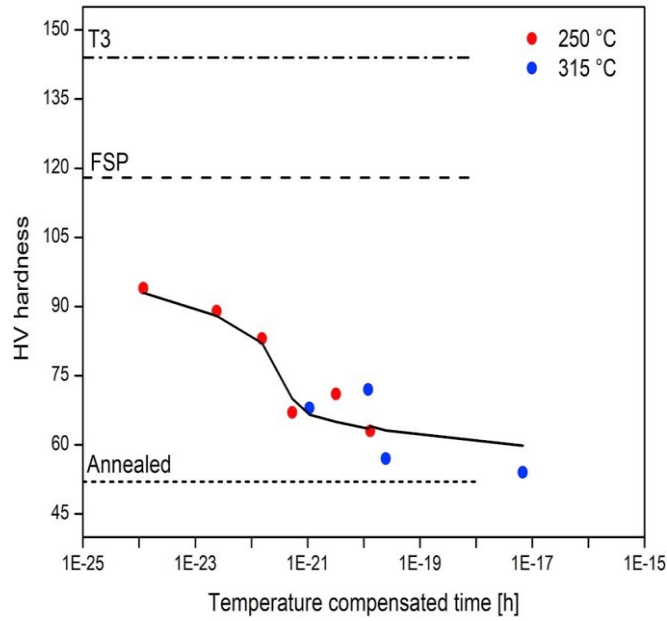


Figure 5.9: Hardness variation as a function of the temperature-compensated time, with $Q = 260 \text{ kJ mol}^{-1}$. The data substantially overlap on the same sigmoidal curve. The Figure also shows the hardness value for the T3 state, for the alloy after FSP, and for the fully annealed condition[118].

The reasons for the decrease in hardness clearly illustrated in Figures 5.8 and 5.9, can be easily found by analyzing the particle distribution after creep (Table 4.2). The table shows the interparticle spacing of the intergranular strengthening precipitates (λ), the respective volume fraction (F_v), and their number per unit volume (N_v). Figures 5.10 and 5.11. clearly shows the typical rod morphology of the particles, typically aligned along the (200)-Al crystallographic direction.

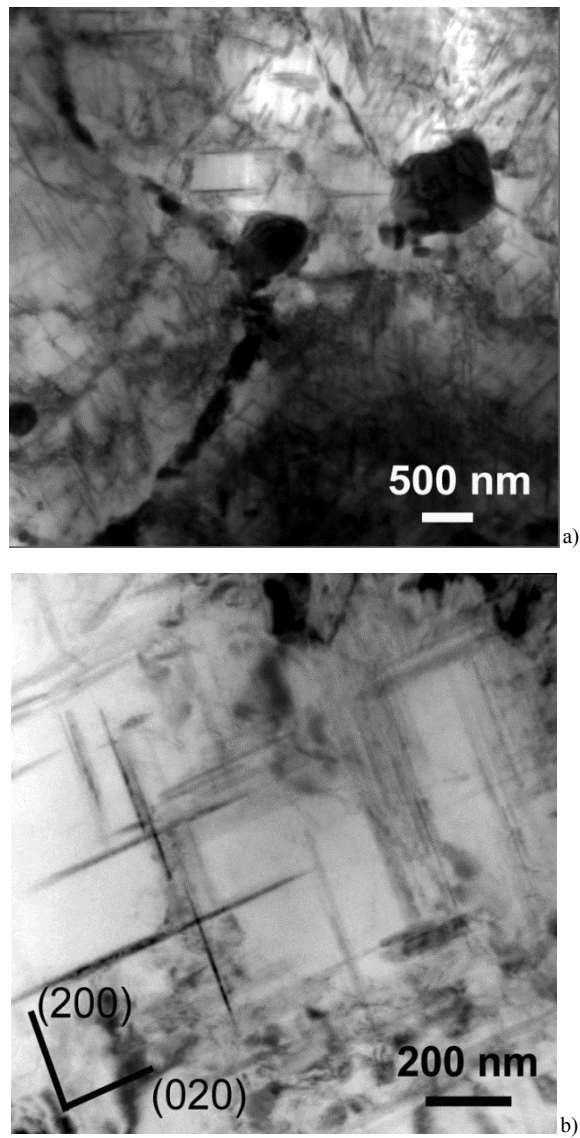


Figure 5.10: Representative TEM micrographs of the sample tested under 140 MPa at 250°C. (a) The presence of large intergranular precipitates is well documented; (b), an example of the fine intragranular particles is shown.

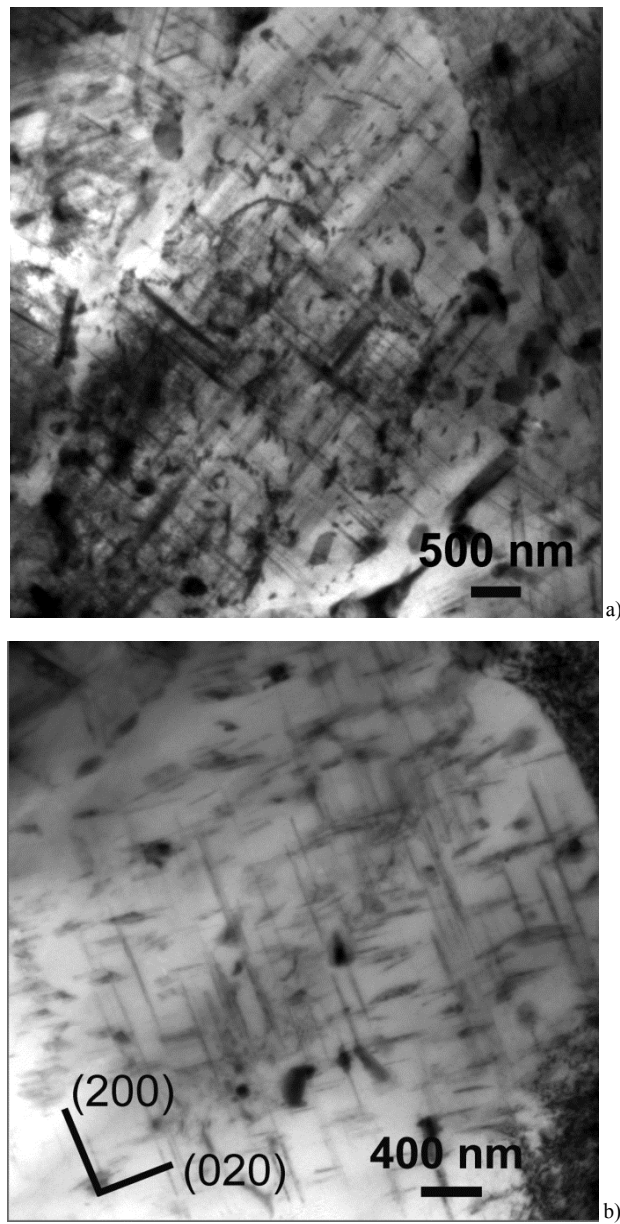


Figure 5.11: Representative TEM micrographs of the sample tested under 100 MPa at 250°C.

With this regard, the almost equiaxed precipitates visible in the TEM micrographs of Figures 5.10-to-5.12 are actually rods laying along the (002)-Al direction, *i.e.* the along the electron beam direction. The dramatic reduction of the volume fraction of intragranular precipitates, and their progressive loss of effectiveness as dislocation obstacles due to the very large interparticle distance (spacing, λ), are self-apparent. Other than these meaningful features, the secondary phase particle mean dimensions were also affected by the different creep loads at 250°C. It is worth to mention here that the volume size of the rod-shaped secondary phase particles did evolve primarily in their length. The lateral size ranged from 5 to 50 nm, while the thickness varied correspondingly only from 25 to 30 nm. On the other hand, the plate length greatly varied from typical minimum values of few tens to maximum of thousands of nanometers. Thence, Fig. 5.13. reports the cumulative size distribution of the plate length for the creep loads of 30, 100, and 140 MPa at 250°C, corresponding to the conditions inspected by TEM, which are representatively reported in Figure 5.12. It is apparent that the mean particle length reduced to almost half from 30 to 140 MPa, with concurrent dramatic volume fraction, F_V , increment of almost 30-times (shown in Table 5.2). The corresponding distribution appears to be rather similar among the three conditions spanning from ~10 to ~2600 nm.

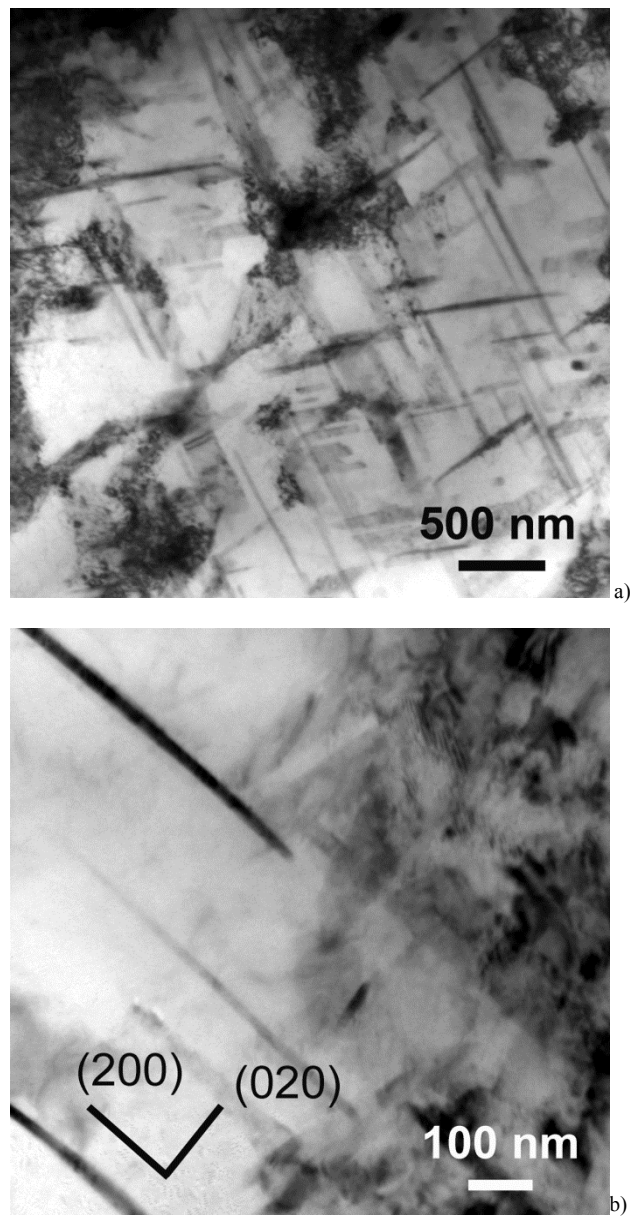


Figure 5.12: Representative TEM micrographs of the sample tested under 30 and 50 MPa at 250°C.

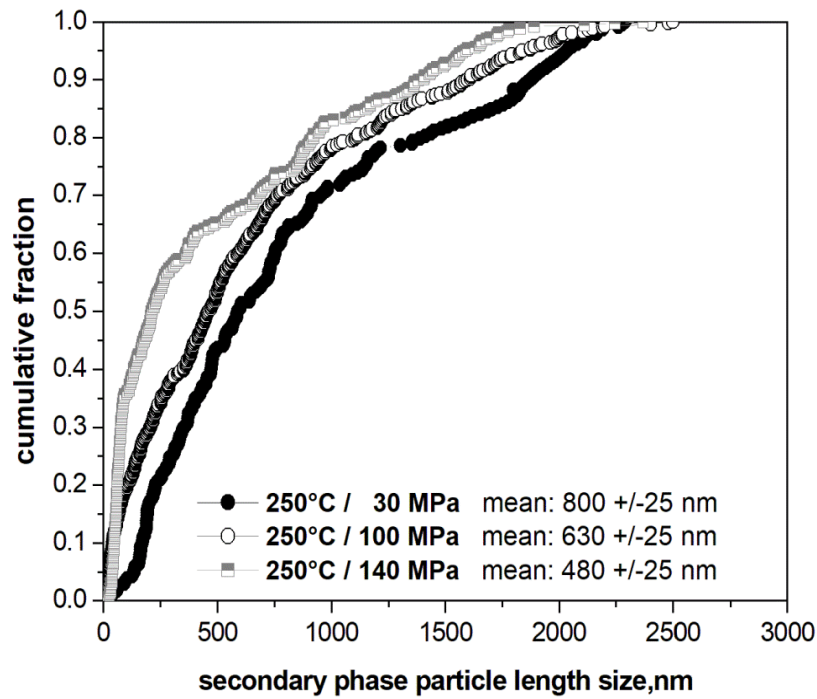


Figure 5.13: *Distribution of the secondary phase particle length, of the samples tested under 30, 100, and 140 MPa at 250°C.*

Creep exposure at 315°C, as suggested by Figure 5.9, leads to an even more pronounced softening of the microstructure, which closely corresponds to the dissolution of the finest particles, and the residual presence of coarse rods (Fig. 5.14), whose strengthening effect is limited.

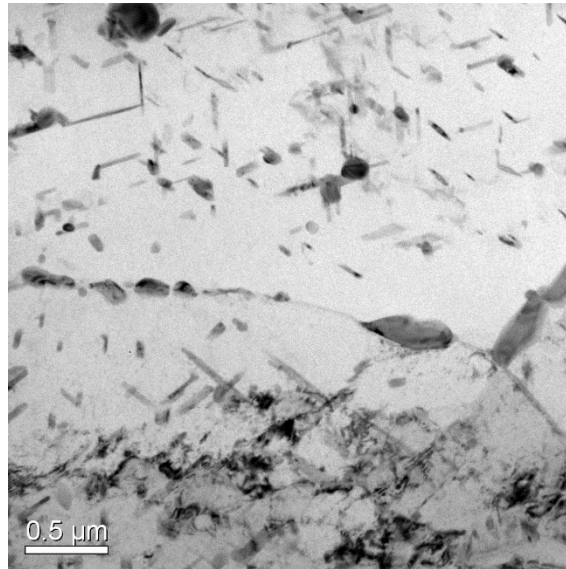


Figure 5.14: Representative TEM micrograph of the sample tested under 25 MPa at 315°C.

5.5. Creep data

The model curves obtained for 2024-T3 alloy at 250 and 315°C (Fig.5.15.), shows the minimum creep rate data for the FSP 2024-T3 alloy, compared with the model curve calculated in similar testing condition for the parent alloy[119]. The Figure clearly shows that FSP results in substantially higher creep rate. A significant scatter of the experimental data was indeed observed in the high-stress regime at 250°C (120-140 MPa).

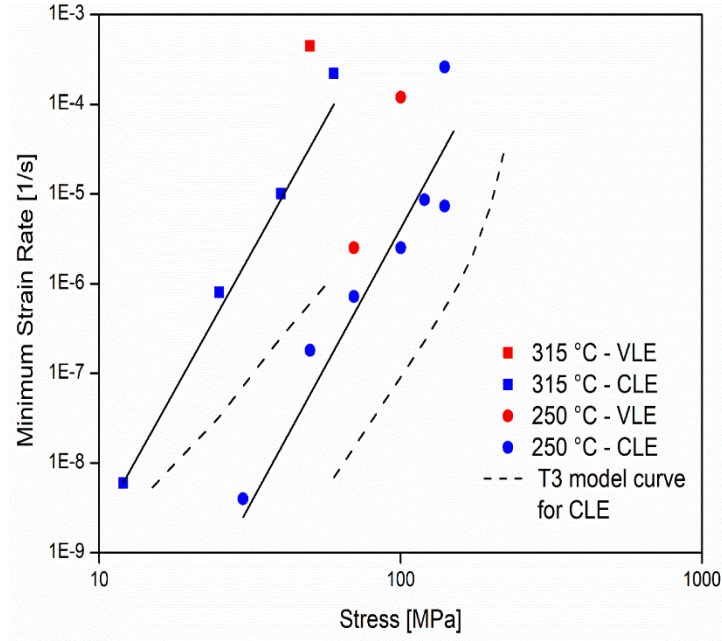


Figure 5.15: Minimum creep rate dependence on applied stress for 2024-T3 FSP alloy, tested both in constant (CLE) and variable (VLE) load conditions. The Figure also shows the strain rate for the base alloy tested by CLE (broken curves).

The temperature dependence of the minimum strain rate was in first instance calculated, based on the phenomenological equation (Eq. (5.5)):

$$\dot{\epsilon}_m = A(\sigma) \exp \left(-\frac{Q}{RT} \right) \quad (5.5)$$

where Q is the apparent activation energy for creep, and $A(\sigma)$ is a stress-dependent parameter. The value of the activation energy was obtained as $Q = 260 \text{ kJ mol}^{-1}$, so the value was substantially higher in AA2024-T3,

to be compared with the value of (122 kJ mol⁻¹ [93]) for the activation energy for self-diffusion in Al. This high value of the activation energy again clearly indicates that in this complex alloy, the microstructure is thermally unstable, i.e. it undergoes significant changes during prolonged holding at high temperature, as occurred in the case of the parent material[119]. This fact is confirmed by the substantially higher values of the minimum strain rate obtained in VLE when compared with CLE carried out under the same stress. A similar behaviour can be explained by the progressive softening of the microstructure as the time of exposure at high temperature under a given applied load increases. Fig. 5.16. shows the Zener-Hollomon parameter Z (Eq. (5.6)) as a function of applied stress.

$$Z = \dot{\epsilon}_m \exp \left(\frac{Q}{RT} \right) \quad (5.6)$$

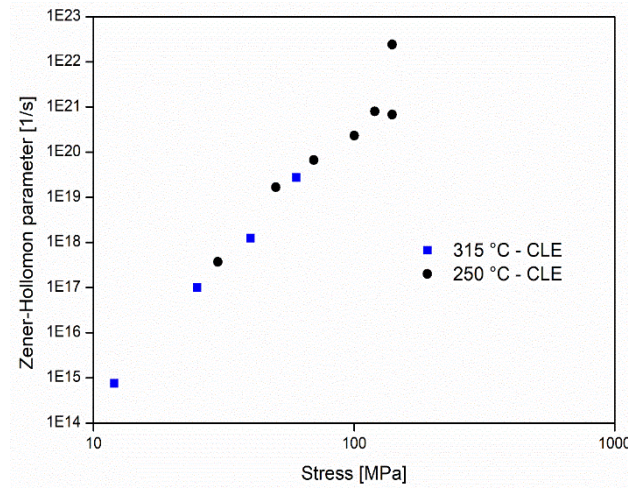


Figure 5.16: Zener-Hollomon parameter as a function of applied stress for 2024-T3 FSP tested under constant load conditions.

5.6. Creep modelling of AA2024-T3

The basic model that will be used here to describe the high-temperature deformation of *AA2024-T3*, was originally developed for Cu[106], and was illustrated in the previous chapter. Here, one can simply mention that the model is based on the Taylor equation, (Eq.5.7)

$$\sigma = \sigma_i + \sigma_{ss} + \sigma_\rho = \sigma_i + \sigma_{ss} + \alpha m G b \sqrt{\rho} \quad (5.7)$$

where m is the Taylor factor ($m = 3.06$ for fcc metals) and $\sigma_\rho = \alpha m G b \rho^{1/2}$ is the dislocation hardening term. The term σ_i represents the stress required to move a dislocation in the absence of other dislocations, and incorporates the effect of grain size, while α is a constant (in the following, $\alpha = 0.3$ will be considered). As already mentioned, solute atmospheres reduce dislocation mobility; the term σ_{ss} thus represents the stress required for dislocations to move through the viscous drag due to solute atoms (Cu and Mg in AA2024). Since Cu and Mg mostly combine with Al to form the precipitates, the drag stress is here assumed to be very low, i.e. quite negligible in comparison with the other terms in Equation (5.7). On this basis, the assumption $\sigma_{ss} \cong 0$ will be used in the following. Last, the threshold stress σ_0 represents the strengthening contribution due to the interaction between fine particles and dislocations. In aged AA2024 alloy, the aluminum matrix is reinforced with a densely spaced distribution of precipitates.

In Al-Cu-Mg alloys with Cu: Mg atomic ratio close to 1, the precipitation sequence is described as:

$\alpha_{ss} \rightarrow \text{Cu:Mg co-clusters/GPB zones} \rightarrow \text{GPB2/S'' phase} \rightarrow \text{S'/S phase}$

where α_{ss} is the super-saturated solid solution, GPB are the Guiner-Preston-Bagaryatsky zones and the S'' (GPB2) is an intermediate phase preceding the formation of the semicoherent S' phase[120]. The equilibrium S-phase in the peak-aged state assumes the shape of non-shearable rods aligned in the {100} directions, although equiaxed precipitates can be also observed in the alloy after long creep exposure[102]. Under high applied stress, the particle strengthening effect is equivalent to Orowan stress σ_{Or} as shown in equation (5.8)., $\alpha_p=0.7$ and 0.55 at 250°C and 315°C, for the investigated alloy (AA2024-T3) [119].

$$\sigma_0 = \alpha_p \sigma_{Or} \quad (5.8)$$

On other hand Equation (5.9) shows the constitutive model derivation for the creep rate dependence on applied stress at steady state, where λ is the interparticle spacing, τ_l is the dislocation line tension ($\tau_l=0.5Gb^2$) and $\sigma_\rho = \sigma - \sigma_0 - \sigma_i - \sigma_{ss} \cong \sigma - \sigma_0 = \sigma_e$ [119].

$$\dot{\epsilon}_m = \frac{2M_{cg}\tau_lb\lambda}{m} \left(\frac{\sigma_\rho}{\alpha m Gb} \right)^4 \quad (5.9)$$

Equation (5.10), shows the dislocation climb mobility M , assumes the form: where R_{max} , is the maximum strength of the alloy, k is the boltzman constant, D_{0L} and Q_L are the pre-exponential factor and the activation energy in the Arrhenius equation describing the temperature dependence of the vacancy diffusion coefficient. So R_{max} , which depends on material structure, is the flow stress required to plastically deform the material in the absence of thermal activation and $D = D_{0m} \exp(-Q_L/RT)$ is the appropriate diffusion coefficient, (Q_L is thus the activation energy to overcome the obstacle field).

$$M \cong \frac{D_{0L}b}{kT} \exp\left[\frac{\sigma_\rho b^3}{kT}\right] \exp\left\{-\frac{Q_L}{RT}\left[1 - \left(\frac{\sigma_\rho}{R_{max}}\right)^2\right]\right\} \exp\left(-\frac{U_{ss}}{RT}\right) \quad (5.10)$$

The U_{ss} is a term describing the energy necessary for Cu and Mg atoms still in solid solution to jump in and out of the atmospheres that spontaneously form around dislocations ($U_{ss} \cong 14.5 \text{ kJ mol}^{-1}$ [119]). So, the U_{ss} term has been introduced to take into account that during viscous glide in solid solution alloys, solute atoms have to jump in and out the atmospheres that spontaneously form around dislocations. Thus, an additional term, describing the energy due to overcome this barrier, must be added to the activation energy. This additional term has the former equations (5.11 & 5.12):

$$U_{ss} = \frac{\beta R}{bk} \quad (5.11)$$

With

$$\beta = \frac{1}{3\pi} \frac{(1+\nu)}{(1-\nu)} bG\Omega\delta_i \quad (5.12)$$

where ν is the Poisson's ratio, Ω is the average atomic volume and δ_i is the volume atomic misfit for the i -species in solid solution, (details about Ω and δ_i calculation in complex alloys are given in [119]).

The maximum strength R_{max} at the testing temperature is here tentatively quantified as (Eq 5.13)):

$$R_{max} = \frac{1.5 G \left(R_{UTS}^a + \sigma_{Or} \right)_{RT}}{G_{RT}} \quad (5.13)$$

Where R_{UTS}^a the tensile strength of an alloy with the same impurity level and similar content of elements in solid solution and coarse intergranular precipitates. The term σ_{Or} indicates the Orowan stress generated by a dispersion of particles equivalent to that observed in the crept samples after testing; the RT suffix, in turns, denotes the room temperature values of the considered parameters (tensile strength, Orowan stress, shear modulus). Equations (5.9) - (5.13) analyse the critical parameters for modelling the minimum creep rate. The σ_0 term, at high temperature, for example, can be considered to be proportional to the Orowan stress σ_{Or} , which, in turns, depends on the interparticle spacing λ and to particle shape. The detailed analysis reported in [119] gave an excellent description of the experimental data for the 2024-T3 alloy, by assuming that all the precipitates were in forms of rods. In addition, the model also accounted for the stress accelerated coarsening process of the strengthening particles.

It is obvious, that to properly use the model in this articulated and complex form, one should have a detailed knowledge of the microstructural evolution during creep exposure. In the case of the present study, a different approach was used, starting from the available information on the variation of hardness with creep time. So the variation of hardness with creep time is used, so the Vickers hardness HV_{MPa} can be described by equation (5.14).

$$\sigma_{ys} = \beta_a HV_{MPa} - \beta_b \quad (5.14)$$

where β_a and β_b are constants. Values of β_a is from 0.266 to 0.383 for Al-Mg-Si alloys[121]. The β_b value can be calculated for the material investigated in the present study, by assuming $\beta_a=0.303$, by considering the same alloy has a different state condition (-T3 and FSP) with hardness (HV_{MPa}) 1411 and 1152 MPa, for yield stresses 362 and 284 MPa. So β_b is calculated to be 65 MPa.

The next step consists in estimating the contribution of the particles in the yield strength. At yielding, Eqn. (5.4) can be rewritten by explicitly introducing the Hall-Petch hardening term (σ_g), giving (Eq. (5.15)):

$$\sigma_{ys} = \sigma_{i0} + \sigma_{ss} + \sigma_0 + \sigma_g + \alpha m G b \sqrt{\rho} \quad (5.15)$$

where σ_{i0} is the stress necessary to move the dislocations in the pure metal with very coarse structure.

In addition, one can reasonably assume that (Eq. (5.16)):

$$\sigma_y^a = \sigma_{i0} + \sigma_{ss} \quad (5.16)$$

where σ_y^a is the yield strength of the matrix, that is, of a fully annealed large-grained alloy with comparable levels of impurities and elements in solid solution, and with massive particles on grain boundaries, thus giving, for the considered alloy (Eq. (5.17)):

$$\sigma_0 = \sigma_y - \sigma_y^a - \sigma_g - \alpha m G b \sqrt{\rho} \quad (5.17)$$

Let one considers $\sigma_y^a \cong 55$ MPa (yield stress for an alloy containing 0.5 Mg and 0.5 Mn) [118], σ_g being: (Eq. (5.18)):

$$\sigma_g = \frac{k_{hp}}{\sqrt{d_g}} \quad (5.18)$$

with $k_{hp} = 2.6$ MPa mm^{-0.5} [119] and $d_g = 5 \times 10^{-3}$ mm; the last term to be determined for estimating the particle strengthening term from the curve presented in Fig. 4.9, is the dislocation density. Creep is known to introduce dislocation densities which can be well above 10^{13} m⁻³ [93]; yet, after rupture, the samples considered in the present study remained in the furnace for a sufficiently long time to consider that the free dislocation density underwent a substantial annealing. Thus, it is here assumed that $\rho = 1 \times 10^{12}$ m⁻³, irrespective of the applied stress or temperature.

Then, Eqn. (5.17) provides the estimates of the particle strengthening term (in this case the Orowan stress, since room temperature data are considered) presented in Fig. 5.13. These values can be considered to be reasonably accurate for the tests carried out in the low stress regime, where the dislocation density cannot be much larger than $1 \times 10^{12} \text{ m}^{-3}$. The situation could be somewhat different for the tests carried out under the lower stresses at 250°C, where higher values of the dislocation density can be expected, leading to a reduced value of σ_0 , that is, the values presented in Fig. 5.14. could be overestimated. On the other hand, this effect is balanced by the fact that in the following it will be assumed that the microstructure at the end of the test was substantially equivalent to that corresponding to the minimum creep rate. For CLE tests carried out in the high stress regime, this would lead to an underestimation of the value of the particle strengthening term in correspondence to the minimum creep rate.

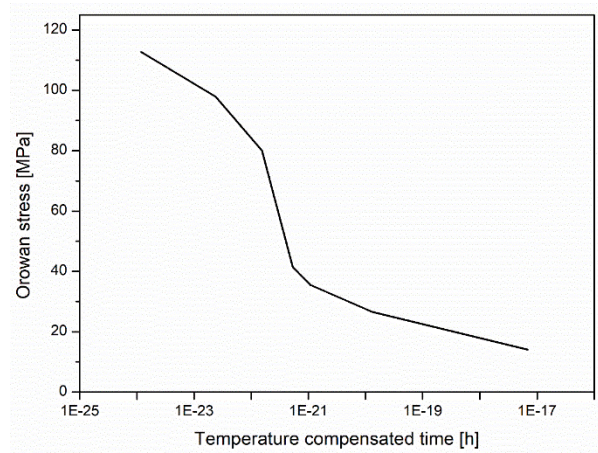


Figure 5.17: Particle (Orowan) strengthening term as a function of temperature compensated testing time.

The last missing major parameter in the model is the interparticle distance. The usual relationship between the Orowan stress and the interparticle spacing is of inverse proportionality. The interparticle values presented in Table 5.2., the corresponding yield stresses from Fig. 5.17 and the best fitting straight line are presented in Fig. 5.18., which can be then used to estimate λ for all the considered experimental conditions.

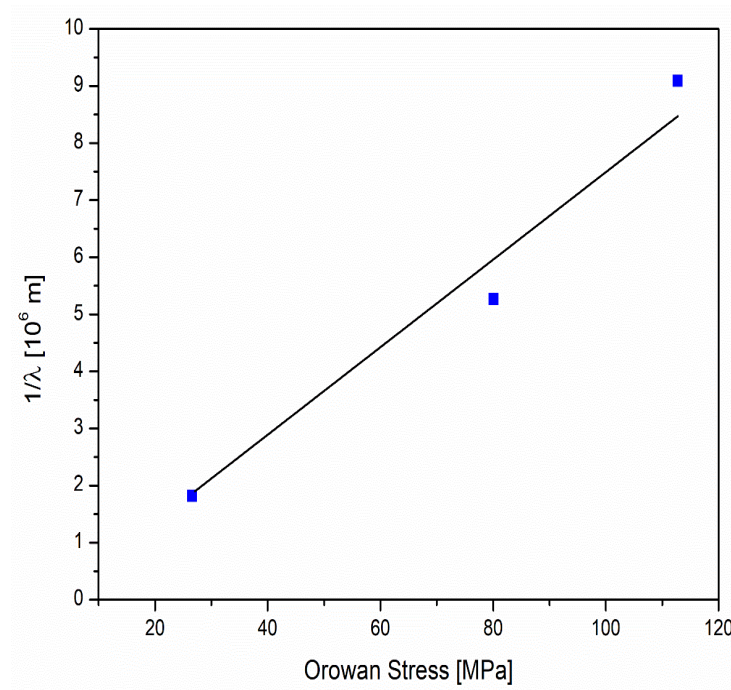


Figure 5.18: Reciprocal of particle spacing as a function of the Orowan stress at room temperature.

At this stage, all the necessary information is available, and equations (5.9) – (5.10) can be used, as in [119], with $\alpha_p = 0.7$ and 0.55 at 250 and 315°C respectively, $Q_{sd} = 122 \text{ kJ mol}^{-1}$, $D_{0sd} = 8.3 \times 10^{-6} \text{ m}^2 \text{ s}^{-1}$ and $b = 2.86 \times 10^{-10} \text{ m}$. The calculated model curves for both CLE and VLE are reported in Fig. 5.19. The curves for CLE data are actually obtained by connecting the value of the strain rate calculated for each stress, by assuming that the particle distribution in correspondence of the minimum creep rate is equivalent to that observed after the end of the test. Thus, the curve connects strain rate values that correspond to different microstructures, namely different particle sizes and distributions. By contrast, the curves modelling the VLE data, are obtained by assuming that the particle distribution for the whole loading sequence remains substantially unchanged, with respect to the one that could be observed in correspondence to the minimum creep rate under the first (and lowest) applied stress, just before load increase. Thus, each single VLE curve roughly corresponds to a constant microstructure, in terms of particle size and distribution. The description of the experimental data, which was obtained without any need of creep data fitting, is remarkably accurate, except under the highest stresses, i.e. in the region where a quite important scatter of the data was observed.

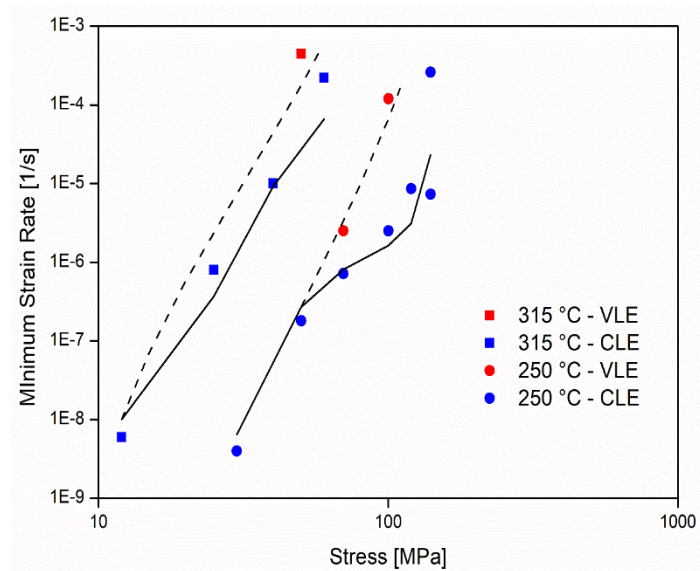


Figure 5.19: Basic creep modelling of the minimum strain rate dependence on applied stress for CLE (solid curves) and VLE (broken curves).

The analysis of Fig. 5.18. definitely confirms that the model presented in [119] is an excellent tool for describing the creep response of age-hardening alloys. In addition, the accuracy of the description suggests that the measure of the hardness variation after creep can give precious information to quantify the particle-strengthening term.

5.7. Summary and Conclusions

In this chapter, a constitutive model based on a theoretical approach has been used in the present study to describe the creep response of an AA2024-T3 alloy processed by FSP. The material, after FSP, exhibited a strong reduction in creep resistance, attested by higher values of the minimum creep rate, when compared with the base metal. The model, already successfully used for the description of the creep behaviour of the base alloy in –T3 state, was here applied to the transformed alloy with a fine recrystallized grain size and lower mechanical strength. This achievement represents a substantial advantage over conventional approaches based on phenomenological equations. The hardness variation with creep duration was used to quantify the particle strengthening term, in order to properly describe the softening phenomena associated to high-temperature exposure. The resulting model curves gave an excellent description of the experimental results, without requiring any data-fitting of the creep data, which represents a substantial advantage over conventional approaches based on phenomenological equations.

Chapter 6.

Conclusions

The conclusions from these chapters are summarized in the following sections.

In dynamic conditions, the behavior of metals is generally characterized by an increase of the strength due to the high strain rate (strain rate hardening) and, simultaneously, a decrease of the strength due to the increase of temperature (thermal softening), related to the conversion of plastic work into heat. Depending on the material, the strain rate and temperature sensitivities could be coupled or uncoupled and change as function of the strain. For this reason, it is fundamental to deeply investigate the material response varying the loading condition.

In particular, in this thesis, the attention was focused on some of the most common material models:

- i. the phenomenological constitutive model discussed in Chapter 3 (Garofalo and Arrhenius equations, combined with the Hensel and Spittel relationship) can successfully describe the material behavior, but each material (even each initial microstructure) should be treated independently. Thus, no generalizations can be obtained;
- ii. hot workability of IN718, discussed in Chapter 4, gave another insight into deformation behavior at high temperature deformation and strain rate with the corresponding microstructure. In this case both phenomenological approaches, based on Garofalo and Arrhenius-

equations and basic creep modelling were used to describe the response in IN718 and pure Ni and dislocation hardening and solid solution strengthening. The use of basic model is relatively easy here, since the material was deformed in a solid solution single phase state;

- iii. modelling of the creep response for AA2024-T3 produced by friction stir processing were discussed in Chapter 5. In this case the microstructure presents all the typical features of complex materials, in which particle strengthening and dislocation hardening coexist. The basic modelling was successfully used, although in a simplified form, to describe mechanical data (minimum creep rate as a function of applied stress).

On the bases of the previous results, one can reasonably conclude that basic modelling is a power tool for the prediction of material behavior, as long as a deep knowledge of the microstructural features of the alloy is available. On the other hand, phenomenological approach still maintains its validity in all those cases in which only a qualitative description of microstructural evolution is available. In addition, the state of art of the Finite Element Modelling tools only permit to fully exploit the phenomenological models, although implementation of basic models in FEM codes libraries is predictable.

References

- [1] R.C. Reed, *The Superalloys: Fundamentals and Applications*, Cambridge Univ. Press. (2006). doi:10.1016/j.laa.2011.01.014.
- [2] G.. Meetham, High-temperature materials- a general review, 26 (1991) 853–860.
- [3] A.S.M. International, A. Rights, *ASM specialty handbook: nickel, cobalt, and their alloys*, 2013. doi:10.5860/choice.38-6206.
- [4] M.J. Donachie, *Titanium: A Technical Guide*, 2nd Edition, 2000. doi:10.5772/1844.
- [5] J.R. Davis, *Light Metals and Alloys*, in: ASM Int., 2001: pp. 351–416. doi:10.1361/autb2001p351.
- [6] Y.C. Lin, M.S. Chen, J. Zhong, Constitutive modeling for elevated temperature flow behavior of 42CrMo steel, *Comput. Mater. Sci.* 42 (2008) 470–477. doi:10.1016/j.commatsci.2007.08.011.
- [7] Y.C. Lin, M.S. Chen, J. Zhong, Study of static recrystallization kinetics in a low alloy steel, *Comput. Mater. Sci.* 44 (2008) 316–321. doi:10.1016/j.commatsci.2008.03.027.
- [8] Y.C. Lin, M.S. Chen, J. Zhong, Prediction of 42CrMo steel flow stress at high temperature and strain rate, *Mech. Res. Commun.* 35 (2008) 142–150. doi:10.1016/j.mechrescom.2007.10.002.
- [9] A. Rusinek, J.A. Rodríguez-Martínez, A. Arias, A thermo-viscoplastic constitutive model for FCC metals with application to OFHC copper, *Int. J. Mech. Sci.* 52 (2010) 120–135. doi:10.1016/j.ijmecsci.2009.07.001.

- [10] H. Shin, J.-B. Kim, A Phenomenological Constitutive Equation to Describe Various Flow Stress Behaviors of Materials in Wide Strain Rate and Temperature Regimes, *J. Eng. Mater. Technol.* 132 (2010) 021009. doi:10.1115/1.4000225.
- [11] B. Lei, G. Chen, K. Liu, X. Wang, X. Jiang, J. Pan, Q. Shi, Constitutive Analysis on High-Temperature Flow Behavior of 3Cr-1Si-1Ni Ultra-High Strength Steel for Modeling of Flow Stress, *Metals (Basel)*. 9 (2019) 42. doi:10.3390/met9010042.
- [12] Y.C. Lin, X.M. Chen, A critical review of experimental results and constitutive descriptions for metals and alloys in hot working, *Mater. Des.* 32 (2011) 1733–1759. doi:10.1016/j.matdes.2010.11.048.
- [13] Y.C. Lin, Y.C. Xia, X.M. Chen, M.S. Chen, Constitutive descriptions for hot compressed 2124-T851 aluminum alloy over a wide range of temperature and strain rate, *Comput. Mater. Sci.* 50 (2010) 227–233. doi:10.1016/j.commatsci.2010.08.003.
- [14] D. Samantaray, S. Mandal, A.K. Bhaduri, Constitutive analysis to predict high-temperature flow stress in modified 9Cr-1Mo (P91) steel, *Mater. Des.* 31 (2010) 981–984. doi:10.1016/j.matdes.2009.08.012.
- [15] S. Mandal, V. Rakesh, P. V. Sivaprasad, S. Venugopal, K. V. Kasiviswanathan, Constitutive equations to predict high temperature flow stress in a Ti-modified austenitic stainless steel, *Mater. Sci. Eng. A*. 500 (2009) 114–121. doi:10.1016/j.msea.2008.09.019.
- [16] M.J. Donachie, S.J. Donachie, ASM International. *Superalloys: A Technical Guide*, 2002. doi:10.1016/B978-0-444-43022-9.50017-1.
- [17] J.C.H. Rafael Nunes, Richard D. Blaugher, ASM Handbook Volume 2 Properties and Selection : Nonferrous Alloys and Special-Purpose Materials, 1998. doi:10.1007/s004310050884.

- [18] E. Akca, A. Gürsel, A Review on Superalloys and IN718 Nickel-Based INCONEL Superalloy, *Period. Eng. Nat. Sci.* 3 (2016). doi:10.21533/pen.v3i1.43.
- [19] Y.L. Hu, X. Lin, Y.L. Li, S.Y. Zhang, X.H. Gao, F.G. Liu, X. Li, W.D. Huang, Plastic deformation behavior and dynamic recrystallization of Inconel 625 superalloy fabricated by directed energy deposition, 186 (2020). doi:10.1016/j.matdes.2019.108359.
- [20] Y.B. Tan, Y.H. Ma, F. Zhao, Hot deformation behavior and constitutive modeling of fine grained Inconel 718 superalloy, *J. Alloys Compd.* 741 (2018) 85–96. doi:10.1016/j.jallcom.2017.12.265.
- [21] C. Zhang, L. Zhang, W. Shen, Q. Xu, Y. Cui, The processing map and microstructure evolution of Ni-Cr-Mo-based C276 superalloy during hot compression, *J. Alloys Compd.* 728 (2017) 1269–1278. doi:10.1016/j.jallcom.2017.09.107.
- [22] M. Detrouis, S. Antonov, S. Tin, P.D. Jablonski, A. Hawk, Hot deformation behavior and flow stress modeling of a Ni-based superalloy, *Mater. Charact.* 157 (2019). doi:10.1016/j.matchar.2019.109915.
- [23] Y.C. Lin, D.X. Wen, J. Deng, G. Liu, J. Chen, Constitutive models for high-temperature flow behaviors of a Ni-based superalloy, *Mater. Des.* 59 (2014) 115–123. doi:10.1016/j.matdes.2014.02.041.
- [24] Q. Zuo, F. Liu, L. Wang, C. Chen, Z. Zhang, Prediction of hot deformation behavior in Ni-based alloy considering the effect of initial microstructure, *Prog. Nat. Sci. Mater. Int.* 25 (2015) 66–77. doi:10.1016/j.pnsc.2015.01.007.
- [25] P. Páramo-Kañetas, U. Öztürk, J. Calvo, J.M. Cabrera, M. Guerrero-Mata, High-temperature deformation of delta-processed Inconel 718, *J. Mater. Process. Technol.* 255 (2018) 204–211. doi:10.1016/j.jmatprotec.2017.12.014.

- [26] X. Wei, W. Zheng, Z. Song, T. Lei, Q. Yong, Q. Xie, Static recrystallization behavior of Inconel 718 alloy during thermal deformation, *J. Wuhan Univ. Technol. Mater. Sci. Ed.* 29 (2014) 379–383. doi:10.1007/s11595-014-0925-4.
- [27] N.K. Park, I.S. Kim, Y.S. Na, J.T. Yeom, Hot forging of a nickel-base superalloy, *J. Mater. Process. Technol.* 111 (2001) 98–102. doi:10.1016/S0924-0136(01)00489-7.
- [28] F. Chen, J. Liu, H. Ou, B. Lu, Z. Cui, H. Long, Flow characteristics and intrinsic workability of IN718 superalloy, *Mater. Sci. Eng. A.* 642 (2015) 279–287. doi:10.1016/j.msea.2015.06.093.
- [29] Y. Wang, W.Z. Shao, L. Zhen, L. Yang, X.M. Zhang, Flow behavior and microstructures of superalloy 718 during high temperature deformation, *Mater. Sci. Eng. A.* 497 (2008) 479–486. doi:10.1016/j.msea.2008.07.046.
- [30] Y.C. Lin, K.K. Li, H. Bin Li, J. Chen, X.M. Chen, D.X. Wen, New constitutive model for high-temperature deformation behavior of inconel 718 superalloy, *Mater. Des.* 74 (2015) 108–118. doi:10.1016/j.matdes.2015.03.001.
- [31] S. In, J.M. Zhang, Z.Y. Gao, J.Y. Zhuang, Z.Y. Zhong, Mathematical Modeling of the Hot-Deformation Behavior of Superalloy IN718, 30 (1999).
- [32] M.Z. Hussain, F. Li, J. Wang, Z. Yuan, P. Li, T. Wu, Determination of Constitutive Equation for Thermo-mechanical Processing of INCONEL 718 Through Double Multivariate Nonlinear Regression Analysis, *J. Mater. Eng. Perform.* 24 (2015) 2744–2756. doi:10.1007/s11665-015-1542-x.
- [33] N. Rao, Materials for Gas Turbines – An Overview, *Adv. Gas Turbine Technol.* (2012). doi:10.5772/20730.

- [34] Y. Wang, X. Zeng, Y. Sheng, X. Yang, F. Wang, Multi-objective parameter identification and optimization for dislocation-dynamics-based constitutive modeling of Ti - 6Al - 4V alloy, *J. Alloys Compd.* 821 (2020) 153460. doi:10.1016/j.jallcom.2019.153460.
- [35] Veiga C., Devim J. P., Loureiro A. J. R., PROPERTIES AND APPLICATIONS OF TITANIUM ALLOYS: A BRIEF REVIEW, *Rev. Adv. Mater. Sci.* 32 (2012) 133–148. doi:10.1016/j.rser.2010.03.036.
- [36] N. Poondla, T.S. Srivatsan, A. Patnaik, M. Petraroli, A study of the microstructure and hardness of two titanium alloys: Commercially pure and Ti-6Al-4V, *J. Alloys Compd.* 486 (2009) 162–167. doi:10.1016/j.jallcom.2009.06.172.
- [37] C. An RTI International Metals, INC, Titanium Alloy Guide, 2000.
- [38] Valentin N. Moiseyev, Titanium Alloys Russian Aircraft and Aerospace Applications, 2006.
- [39] N. Gey, M. Humbert, M.J. Philippe, Y. Combres, Investigation of the α - and β - texture evolution of hot rolled Ti-64 products, *Mater. Sci. Eng. A.* 219 (1996) 80–88. doi:10.1016/S0921-5093(96)10388-9.
- [40] F.C. Campbell, Manufacturing Technology For Aerospace Structural Materials, 2006.
- [41] A. Tohru, G. Baker, C. Bates, T. Bell, E. Bird, ASM- Metals Handbook- Heat Treating, Technology. 4 (2001) 3470. doi:10.1016/S0026-0576(03)90166-8.
- [42] G.L. J. Albrecht, Microstructure and Mechanical Properties of Titanium Alloys, *Proc. Titan.* 1 (1999) 363–374.
- [43] J. Porntadawit, V. Uthaisangsuk, P. Choungthong, Modeling of flow behavior of Ti-6Al-4V alloy at elevated temperatures, *Mater. Sci. Eng. A.* 599 (2014) 212–222. doi:10.1016/j.msea.2014.01.064.

- [44] G.J. Tchein, D. Jacquin, E. Aldanondo, D. Coupard, E. Gutierrez-Orrantia, F. Girot Mata, E. Lacoste, Analytical modeling of hot behavior of Ti-6Al-4V alloy at large strain, *Mater. Des.* 161 (2019) 114–123. doi:10.1016/j.matdes.2018.11.025.
- [45] L.X. Li, Y. Lou, L.B. Yang, D.S. Peng, K.P. Rao, Flow stress behavior and deformation characteristics of Ti-3Al-5V-5Mo compressed at elevated temperatures, *Mater. Des.* 23 (2002) 451–457. doi:10.1016/S0261-3069(02)00025-0.
- [46] N.S. Reddy, Y.H. Lee, C.H. Park, C.S. Lee, Prediction of flow stress in Ti-6Al-4V alloy with an equiaxed $\alpha + \beta$ microstructure by artificial neural networks, *Mater. Sci. Eng. A.* 492 (2008) 276–282. doi:10.1016/j.msea.2008.03.030.
- [47] Y.V.R.K. Prasad, T. Seshacharyulu, S.C. Medeiros, W.G. Frazier, A Study of Beta Processing of Ti-6Al-4V: Is it Trivial?, *J. Eng. Mater. Technol.* 123 (2002) 355. doi:10.1115/1.1372708.
- [48] Hugh J. McQueen, Stefano Spigarelli, Michael E. Kassner and Enrico Evangelista. *Hot Deformation and Processing of Aluminum Alloys*, (2011) 599.
- [49] R. Gitter, *Design of Aluminium structures: Selection of Structural Alloys*, 2008.
- [50] D.G. ESKIN, *Physical Metallurgy of Direct Chill Casting of Aluminum Alloys*, 2008.
- [51] Q. Dai, Y. Deng, J. Tang, Y. Wang, Deformation characteristics and strain-compensated constitutive equation for AA5083 aluminum alloy under hot compression, *Trans. Nonferrous Met. Soc. China.* 29 (2019) 2252–2261. doi:10.1016/S1003-6326(19)65131-9.
- [52] M. Dubar, L. Dubar, E.S. Puchi-cabrera, Physically-based constitutive description of a commercial Al-Mg-Si alloy deformed under cold-warm working conditions, 790 (2019) 1177–1191. doi:10.1016/j.jallcom.2019.03.113.

- [53] A.R. Eivani, H. Vafaeenezhad, O. Nikan, J. Zhou, Modeling high temperature deformation characteristics of AA7020 aluminum alloy using substructure-based constitutive equations and mesh- free approximation method, *Mech. Mater.* 129 (2019) 104–112. doi:10.1016/j.mechmat.2018.11.011.
- [54] V. Vilamosa, A.H. Clausen, T. Børvik, B. Holmedal, O.S. Hopperstad, A physically-based constitutive model applied to AA6082 aluminium alloy at large strains, high strain rates and elevated temperatures, *Mater. Des.* 103 (2016) 391–405. doi:10.1016/j.matdes.2016.04.047.
- [55] H. Mirzadeh, Simple physically-based constitutive equations for hot deformation of 2024 and 7075 aluminum alloys, *Trans. Nonferrous Met. Soc. China (English Ed.* 25 (2015) 1614–1618. doi:10.1016/S1003-6326(15)63765-7.
- [56] D. TRIMBLE, G.E. O'DONNELL, Flow stress prediction for hot deformation processing of 2024Al-T3 alloy, *Trans. Nonferrous Met. Soc. China (English Ed.* 26 (2016) 1232–1250. doi:10.1016/S1003-6326(16)64194-8.
- [57] Y.C. Lin, J. Zhang, J. Zhong, Application of neural networks to predict the elevated temperature flow behavior of a low alloy steel, *Comput. Mater. Sci.* 43 (2008) 752–758. doi:10.1016/j.commatsci.2008.01.039.
- [58] R. Bobbili, B. Ramakrishna, V. Madhu, A.K. Gogia, Prediction of flow stress of 7017 aluminium alloy under high strain rate compression at elevated temperatures, *Def. Technol.* 11 (2015) 93–98. doi:10.1016/j.dt.2014.08.004.
- [59] A. Momeni, S.M. Abbasi, Effect of hot working on flow behavior of Ti-6Al-4V alloy in single phase and two phase regions, *Mater. Des.* 31 (2010) 3599–3604. doi:10.1016/j.matdes.2010.01.060.

- [60] T. Seshacharyulu, S.C. Medeiros, W.G. Frazier, Y. Prasad, Hot working of commercial Ti-6Al-4V with an equiaxed alpha-beta microstructure: materials modeling considerations, *Mater. Sci. Eng. A-Structural Mater. Prop. Microstruct. Process.* 284 (2000) 184–194. [papers://82d09eba-ea7e-42aa-9e88-31cb27a3a70e/Paper/p340](https://doi.org/10.1016/S0921-5097(00)00340-0).
- [61] M.J. Luton, C.M. Sellars, Dynamic recrystallization in nickel and nickel-iron alloys during high temperature deformation, *Acta Metall.* (1969). doi:10.1016/0001-6160(69)90049-2.
- [62] J. Cai, K. Wang, P. Zhai, F. Li, J. Yang, A Modified Johnson-Cook Constitutive Equation to Predict Hot Deformation Behavior of Ti-6Al-4V Alloy, *J. Mater. Eng. Perform.* 24 (2015) 32–44. doi:10.1007/s11665-014-1243-x.
- [63] C.M. Lund, D.J. Steinberg, A constitutive model for strain rates from 10^{-4} to 10^6 s^{-1} , *J. Appl. Phys.* 65 (1989) 1528–1533.
- [64] C. Zener, J.H. Hollomon, Effect of strain rate upon plastic flow of steel, *J. Appl. Phys.* (1944). doi:10.1063/1.1707363.
- [65] M. Xiao, F. Li, W. Zhao, G. Yang, Constitutive equation for elevated temperature flow behavior of TiNiNb alloy based on orthogonal analysis, *Mater. Des.* 35 (2012) 184–193. doi:10.1016/j.matdes.2011.09.044.
- [66] H. Mirzadeh, J.M. Cabrera, A. Najafizadeh, Constitutive relationships for hot deformation of austenite, *Acta Mater.* 59 (2011) 6441–6448. doi:10.1016/j.actamat.2011.07.008.
- [67] J. rong Cao, Z. dong Liu, S. chang Cheng, G. Yang, J. xin Xie, Constitutive Equation Models of Hot-Compressed T122 Heat Resistant Steel, *J. Iron Steel Res. Int.* 19 (2012) 53–58. doi:10.1016/S1006-706X(12)60127-7.

- [68] J. Zhao, J. Zhong, F. Yan, F. Chai, M. Dargusch, Deformation behaviour and mechanisms during hot compression at supertransus temperatures in Ti-10V-2Fe-3Al, *J. Alloys Compd.* 710 (2017) 616–627. doi:10.1016/j.jallcom.2017.03.219.
- [69] R. Chen, S.X. Hui, W.J. Ye, Y. Yu, X.J. Mi, D.G. Lee, Y.T. Lee, High-temperature deformation behaviors of Ti-2Al-9.2Mo-2Fe alloy with boron, *Rare Met.* (2017) 1–11. doi:10.1007/s12598-017-0908-7.
- [70] J. Cai, F. Li, T. Liu, B. Chen, M. He, Constitutive equations for elevated temperature flow stress of Ti-6Al-4V alloy considering the effect of strain, *Mater. Des.* 32 (2011) 1144–1151. doi:10.1016/j.matdes.2010.11.004.
- [71] G.E. Dieter, H. a. Kuhn, S.L. Semiatin, *Handbook of Workability and Process Design*, *Handb. Work. Process Des.* (2003) 278–290. doi:10.1361/hwpd2003p232.
- [72] A. Majorell, S. Srivatsa, R.C. Picu, Mechanical behavior of Ti-6Al-4V at high and moderate temperatures-Part I: Experimental results, *Mater. Sci. Eng. A.* 326 (2002) 297–305. doi:10.1016/S0921-5093(01)01507-6.
- [73] L. Donati, A. Segatori, M. El Mehtedi, L. Tomesani, Grain evolution analysis and experimental validation in the extrusion of 6XXX alloys by use of a lagrangian FE code, *Int. J. Plast.* 46 (2013) 70–81. doi:10.1016/j.ijplas.2012.11.008.
- [74] A. Hensel, T. Spittel, *Kraft- und Arbeitsbedarf bildsamer Formgebungsverfahren*, Deutscher Verlag für Grundstoffindustrie, 1978.
- [75] S. Spigarelli, M. El Mehtedi, A new constitutive model for the plastic flow of metals at elevated temperatures, *J. Mater. Eng. Perform.* (2014). doi:10.1007/s11665-013-0779-5.

- [76] T. Seshacharyulu, S.C. Medeiros, W.G. Frazier, Y.V.R.K. Prasad, Microstructural mechanisms during hot working of commercial grade Ti-6Al-4V with lamellar starting structure, *Mater. Sci. Eng. A.* 325 (2002) 112–125. doi:10.1016/S0921-5093(01)01448-4.
- [77] M. Hu, L. Dong, Z. Zhang, X. Lei, R. Yang, Y. Sha, A Novel Computational Method of Processing Map for Ti-6Al-4V Alloy and Corresponding Microstructure Study, *Materials* (Basel). (2018). doi:10.3390/ma11091599.
- [78] P. Honarmandi, M. Aghaie-Khafri, Hot Deformation Behavior of Ti-6Al-4V Alloy in β Phase Field and Low Strain Rate, *Metallogr. Microstruct. Anal.* (2013). doi:10.1007/s13632-012-0052-6.
- [79] G.L. e J.J. S. Semiatin, Application of the Torsion Test to Determine Workability, *Met. Handb.* 8 (1985) 154–184.
- [80] J. GEORGE E. DIETER, *Mechanical Metallurgy*, (1961). doi:10.1093/oxfordhb/9780199238828.013.0020.
- [81] H.K. e S.S. G. Dieter, *Bulk Workability Testing*, 2003.
- [82] Y.C. Lin, J. Deng, Y.Q. Jiang, D.X. Wen, G. Liu, Effects of initial δ phase on hot tensile deformation behaviors and fracture characteristics of a typical Ni-based superalloy, *Mater. Sci. Eng. A.* 598 (2014) 251–262. doi:10.1016/j.msea.2014.01.029.
- [83] Y.C. Lin, J. Deng, Y. Jiang, D. Wen, G. Liu, Hot tensile deformation behaviors and fracture characteristics of a typical Ni-based superalloy, *J. Mater.* 55 (2014) 949–957. doi:10.1016/j.matdes.2013.10.071.
- [84] L. Cheng, X. Xue, B. Tang, H. Kou, J. Li, Intermetallics Flow characteristics and constitutive modeling for elevated temperature deformation of a high Nb containing TiAl alloy, *Intermetallics*. 49 (2014) 23–28. doi:10.1016/j.intermet.2014.01.007.

- [85] H.J. McQueen, N.D. Ryan, Constitutive analysis in hot working, *Mater. Sci. Eng. A.* 322 (2002) 43–63. doi:10.1016/S0921-5093(01)01117-0.
- [86] S.S. Y. Prasad, K. Rao, *Hot Working Guide: A Compendium of Processing Maps*, ASM international, 2015.
- [87] S. Spigarelli, C. Paoletti, A Unified Physical Model for Creep and Hot Working of Al-Mg Solid Solution Alloys, *Metals (Basel)*. 8 (2017) 9. doi:10.3390/met8010009.
- [88] A. Thomas, M. El-Wahabi, J.M. Cabrera, J.M. Prado, High temperature deformation of Inconel 718, *J. Mater. Process. Technol.* 177 (2006) 469–472. doi:10.1016/j.jmatprotec.2006.04.072.
- [89] P. Geng, G. Qin, J. Zhou, Z. Zou, Hot deformation behavior and constitutive model of GH4169 superalloy for linear friction welding process, *J. Manuf. Process.* 32 (2018) 469–481. doi:10.1016/j.jmapro.2018.03.017.
- [90] M. Azarbarmas, M. Aghaie-Khafri, J.M. Cabrera, J. Calvo, Microstructural evolution and constitutive equations of Inconel 718 alloy under quasi-static and quasi-dynamic conditions, *Mater. Des.* 94 (2016) 28–38. doi:10.1016/j.matdes.2015.12.157.
- [91] R. Sandström, Influence of phosphorus on the tensile stress strain curves in copper, *J. Nucl. Mater.* 470 (2016) 290–296. doi:10.1016/j.jnucmat.2015.12.024.
- [92] R. Sandström, H.C.M. Andersson, Creep in phosphorus alloyed copper during power-law breakdown, *J. Nucl. Mater.* 372 (2008) 76–88. doi:10.1016/j.jnucmat.2007.02.005.
- [93] S. Spigarelli, R. Sandström, Basic creep modelling of aluminium, *Mater. Sci. Eng. A.* 711 (2018) 343–349. doi:10.1016/j.msea.2017.11.053.

- [94] P.A. Korzhavyi, R. Sandström, First-principles evaluation of the effect of alloying elements on the lattice parameter of a 23Cr25NiWCuCo austenitic stainless steel to model solid solution hardening contribution to the creep strength, *Mater. Sci. Eng. A.* 626 (2015) 213–219. doi:10.1016/j.msea.2014.12.057.
- [95] M.E. Kassner, K. Kyle, Taylor Hardening in Five Power Law Creep of Metals and Class M Alloys, *Nano Microstruct. Des. Adv. Mater. A Commem. Vol. Profr. G. Thomas' Seventieth Birthd.* 52 (2003) 255–271. doi:10.1016/B978-008044373-7/50050-4.
- [96] R.E.X.B. Mclellan, Temperature Dependence of the Young's Modulus and Shear Modulus of Pure Nickel, Platinum, and Molybdenum, 8 (1977) 1563–1565.
- [97] Y.L. MacEwan JR, MacEwan U, Self-diffusion in polycrystalline Nickel, *Can. J. Chem.* 37 (1959) 1623–1628.
- [98] S. Karashima, H. Oikawa, T. Motomiya, Steady-State Creep Characteristics of Polycrystalline Nickel in the Temperature Range 500 to 1000 °C, *Trans. Japan Inst. Met.* 10 (1969) 205–209. doi:10.2320/matertrans1960.10.205.
- [99] D. Ma, M. Friák, J. Von Pezold, J. Neugebauer, D. Raabe, Ab initio study of compositional trends in solid solution strengthening in metals with low Peierls stresses, *Acta Mater.* 98 (2015) 367–376. doi:10.1016/j.actamat.2015.07.054.
- [100] et al. Appa Rao G, Kumar M, Srinivas M, Effect of solution treatment temperature on the microstructure and tensile properties of P/M (HIP) processed superalloy Inconel 718. In: Loria EA, editor. *Superalloys 718, 625 and 706 and various derivatives*, Pittsburgh TMS Int. (2001) 605–616.
- [101] M. Regev, S. Spigarelli, Study of mechanical, microstructural and thermal stability properties of friction stir processed aluminum 2024-T3 alloy, *Met. Mater.* 57 (2019) 229–236. doi:10.4149/km_2019_4_229.

- [102] M. Regev, T. Rashkovsky, M. Cabibbo, S. Spigarelli, Microstructure Stability During Creep of Friction Stir Welded AA2024-T3 Alloy, *J. Mater. Eng. Perform.* 27 (2018) 5054–5063. doi:10.1007/s11665-017-3122-8.
- [103] J. Ahn, E. He, L. Chen, T. Pirling, J.P. Dear, C.M. Davies, Determination of residual stresses in fibre laser welded AA2024-T3 T-joints by numerical simulation and neutron diffraction, *Mater. Sci. Eng. A.* 712 (2018) 685–703. doi:10.1016/j.msea.2017.12.027.
- [104] Z. Huda, N.I. Taib, T. Zaharinie, Characterization of 2024-T3: An aerospace aluminum alloy, *Mater. Chem. Phys.* 113 (2009) 515–517. doi:10.1016/j.matchemphys.2008.09.050.
- [105] S. Bansal, S. Rana, M. Sharma, Synthesis and Characterization of Al-Cu-Mg Aluminium Alloys and Study the Effect of Deformation and Aging on their Properties, 4 (2017) 112–116. doi:10.17148/IARJSET.2017.4816.
- [106] R. Sandström, Basic model for primary and secondary creep in copper, *Acta Mater.* 60 (2012) 314–322. doi:10.1016/j.actamat.2011.09.052.
- [107] M.E. Kassner, M.T. Pérez-Prado, Five-power-law creep in single phase metals and alloys, *Prog. Mater. Sci.* 45 (2000) 1–102. doi:10.1016/S0079-6425(99)00006-7.
- [108] Gene Mathers, <https://www.twi-global.com>.
- [109] M.E. Kassner and M.-T. Perez-Prado, *Fundamentals of Creep in Metals and Alloys*, Elsevier, Amsterdam, 2009.
- [110] G. Zagar, H. Künzi, A.A. Ioannou, A. Rossoll, Lab course on Deformation and Fracture – Creep Test, (2013) 1–9.

- [111] R.S. Mishra, M.W. Mahoney, S.X. McFadden, N.A. Mara, A.K. Mukherjee, High strain rate superplasticity in a friction stir processed 7075 Al alloy, *Scr. Mater.* 42 (2000) 163–168. doi:10.1016/S1359-6462(99)00329-2.
- [112] N. Nadammal, S. V. Kailas, S. Suwas, A bottom-up approach for optimization of friction stir processing parameters; a study on aluminium 2024-T3 alloy, *Mater. Des.* 65 (2015) 127–138. doi:10.1016/j.matdes.2014.09.005.
- [113] M.S. Węglowski, S. Dymek, C.B. Hamilton, Experimental investigation and modelling of Friction Stir Processing of cast aluminium alloy AlSi9Mg, *Bull. Polish Acad. Sci. Tech. Sci.* 61 (2013) 893–904. doi:10.2478/bpasts-2013-0096.
- [114] P. Cavaliere, Effect of minor Sc and Zr addition on the mechanical properties of Friction Stir Processed 2024 Aluminium alloy, *J. Mater. Sci.* 41 (2006) 4299–4302. doi:10.1007/s10853-006-6996-7.
- [115] A. Suri, A. Sahai, K.H. Raj, N.K. Gupta, Impact and Tensile testing of Al2024 Alloy Processed by Friction Stir Processing, *Procedia Eng.* 173 (2017) 679–685. doi:10.1016/j.proeng.2016.12.145.
- [116] N. Nadammal, S. V. Kailas, J. Szpunar, S. Suwas, Microstructure and Texture Evolution during Single- and Multiple-Pass Friction Stir Processing of Heat-Treatable Aluminum Alloy 2024, *Metall. Mater. Trans. A Phys. Metall. Mater. Sci.* 48 (2017) 4247–4261. doi:10.1007/s11661-017-4184-9.
- [117] J.G. Ren, L. Wang, D.K. Xu, L.Y. Xie, Z.C. Zhang, Analysis and modeling of friction stir processing-based crack repairing in 2024 aluminum alloy, *Acta Metall. Sin. (English Lett.* 30 (2017) 228–237. doi:10.1007/s40195-016-0489-8.
- [118] J.R. Davis, *ASM Specialty Handbook: Aluminum and Aluminum Alloys*, Ohio, USA, 1993.

- [119] C. Paoletti, M. Regev, S. Spigarelli, Modelling of Creep in Alloys Strengthened by Rod-Shaped Particles: Al-Cu-Mg Age-Hardenable Alloys, *Metals (Basel)*. 8 (2018) 930. doi:10.3390/met8110930.
- [120] I.N. Khan, M.J. Starink, J.L. Yan, A model for precipitation kinetics and strengthening in Al-Cu-Mg alloys, *Mater. Sci. Eng. A*. 472 (2008) 66–74. doi:10.1016/j.msea.2007.03.033.
- [121] A.P. Sekhar, S. Nandy, K. Kumar Ray, D. Das, Hardness - Yield Strength Relation of Al-Mg-Si Alloys, *IOP Conf. Ser. Mater. Sci. Eng.* 338 (2018). doi:10.1088/1757-899X/338/1/012011.

List of Publications

Journal Papers

1. **M. Ghat**, M. El Mehtedi, D. Ciccarelli, C. Paoletti, S. Spigarelli. High temperature deformation of IN718 superalloy: use of basic creep modelling in the study of Nickel and single-phase Ni-based superalloys, *Materials at High Temperatures*, 36 (2019), pp. 58 – 67; <https://doi.org/10.1080/09603409.2018.1456508>
2. Marcello Cabibbo, Chiara Paoletti, **Mohamed Ghat**, Archimede Forcellese and Michela Simoncini. Post-FSW Cold-Rolling Simulation of ECAP Shear Deformation and Its Microstructure Role Combined to Annealing in a FSWed AA5754 Plate Joint, *Materials* 2019, 12(9), 1526; <https://doi.org/10.3390/ma12091526>
3. E. Santecchia¹, M. Cabibbo, **M. Ghat**, M. Regev, S. Spigarelli. Physical modeling of the creep response of an Al-Cu-Mg alloy with a fine microstructure transformed by Friction Stir Processing, *Materials Science & Engineering A* 769 (2019); <https://doi.org/10.1016/j.msea.2019.138521>
4. **M. Ghat**, C. Paoletti, M. El Mehtedi, Maria C. Poletti. Constitutive modeling of Ti-6Al-4V alloy above β transus at high strain rates, *Under Processing*.

Conference proceedings

1. **M. Ghat**, M. El Mehtedi, S. Spigarelli. Hot formability of Inconel 718 by using constitutive equations. 37° Convegno Nazionale AIM, Bologna (September 2018).
2. Paoletti, D. Ciccarelli, S. Spigarelli, **M. Ghat**, M. Cabibbo. Ruolo del trattamento criogenico nei processi di rafforzamento per trattamento termico in una lega Al-Mg-Si-Pb, C., lavorazioni plastiche dei metalli, 37° Convegno Nazionale AIM, Bologna (September 2018).

3. C. Paoletti, S. Spigarelli, M. Cabibbo, **M. Ghat**, E. Cerri. Creep behavior of an Al-9,6Si-0,34Mg alloy produced by Additive Manufacturing. European Congress and Exhibition on advanced Materials and Processes (EUROMAT, 1-5 September 2019, Stockholm, Sweden). Poster Presentation.